Non-Equilibrium Quantum Dynamics in a Disordered Ising Magnet

Thesis by
Christopher Simon

In Partial Fulfillment of the Requirements for the
Degree of
Doctor of Philosophy

CALIFORNIA INSTITUTE OF TECHNOLOGY
Pasadena, California

2024
Defended December 01 2023

Christopher Simon
ORCID: 0009-0003-6129-2078

ACKNOWLEDGEMENTS

To my friends, who gave me the confidence to be myself.

To my family, who accepted me unconditionally.

To my brothers, who have always been there for me.

To my parents, who have given me extraordinary amounts of love and patience.

To my wife and dog, who give me purpose.

ABSTRACT

The quantum two-level system, or "qubit," is a simple platform that nonetheless displays fundamentally non-trivial quantum behavior. The rare-earth magnet $LiHoF_4$ is a natural physical representation of a system of coupled qubits. With its uncommonly high crystal anisotropy, $LiHoF_4$ can be mapped to the problem of the Ising model in a transverse field. However, while this Ising approximation can quantitatively predict much of the equilibrium behavior, quantum corrections, originating from off-diagonal terms in the dipolar interaction that generate quantum fluctuations, are crucial in driving non-equilibrium dynamics when subject to an external drive. Furthermore, quenched disorder can be introduced through chemical substitution, which, through the dipolar interaction, generates spatially random pinning fields, as well as internal transverse fields, which drive quantum fluctuations. Noise measurements on the disordered ferromagnet $LiHo_{0.65}Y_{0.35}F_4$ show critical behavior, whose statistics are driven from the underlying pinning distribution, while measurements on $LiHo_{0.40}Y_{0.60}F_4$ display non-critical behavior that can only be attributed to quantum co-tunneling processes. This is the first demonstration of crackling noise in a ferromagnet in the purely quantum regime. Furthermore, pump-probe susceptibility measurements on the decoupled cluster glass show the system being driven out of equilibrium with astonishingly weak drives, due to resonant transitions arising from off-diagonal dipolar terms $\sigma_i^z \sigma_j^x$. Non-linear sample response is observable in inelastic Raman scattering measurements, and these spin clusters also exhibit asymmetric Fano resonances with high Q-factors of $\sim 10^5$. Quantum interference effects can be tuned to fully decouple one of the dressed states from the others, rendering the sample transparent to the drive. This is analogous to optical systems that display electromagnetically-induced transparency, but at 100 Hz frequencies!

PUBLISHED CONTENT AND CONTRIBUTIONS

[1] M. Buchhold, C. S. Tang, D. M. Silevitch, T. F. Rosenbaum, and G. Refael. Quantum dynamics in strongly driven random dipolar magnets. *Physical Review B*, 101(21):214201, June 2020. doi: 10.1103/PhysRevB.101.214201.
C. Tang. was involved in discussions and preparing data for collaborator M. Buchhold who developed the theory, as well as participating in the writing of the manuscript.

[2] D. M. Silevitch, C. Tang, G. Aeppli, and T. F. Rosenbaum. Tuning high-Q nonlinear dynamics in a disordered quantum magnet. *Nature Communications*, 10(1):4001, September 2019. ISSN 2041-1723. doi: 10.1038/s41467-019-11985-1.
C. S. Tang contributed to the data analysis and contributed to the writing of the manuscript.

[3] D. M. Silevitch, J. Xu, C. Tang, K. A. Dahmen, and T. F. Rosenbaum. Magnetic domain dynamics in an insulating quantum ferromagnet. *Physical Review B*, 100(13):134405, October 2019. doi: 10.1103/PhysRevB.100.134405. C. Tang carried out all of the data analysis and contributed to the writing of the manuscript.

[4] C. Simon, D. M. Silevitch, P. C. E. Stamp, and T. F. Rosenbaum. Quantum Barkhausen noise induced by domain wall co-tunneling (Under Review). C. Simon fully designed, set up, and carried out all of the data acquisition and data analysis, and was involved in discussions with collaborator P.C.E. Stamp who developed the theory, and was the primary author of the non-theory portion of the manuscript.

CONTENTS

LIST OF FIGURES

Chapter 1

$LiHo_xY_{1-x}F_4$ AS A MODEL QUANTUM ISING SYSTEM

1.1 The Quantum Two-Level System (TLS) and the Ising Model

The quantum two-level system (TLS), also known as a qubit, is perhaps one of the simplest theoretical objects in quantum mechanics that still displays non-classical behavior. The quantum TLS is a powerful model, both because it is easily understandable compared to other systems, and because it has the potential to model arbitrary quantum problems through expanding the Hilbert space by coupling multiple qubits together. In this introductory section, I will discuss the basis of the quantum TLS, as well as the Ising model, in which qubits are coupled together. These observations underlie the choice of experimental system for my thesis, a physical realization of the Ising model in transverse field, and provide the background considerations in the data accumulation and analysis, and highlight where the physical realization departs from ideality.

The state vectors for the TLS Hamiltonian live in a two-dimensional Hilbert space, where any pure quantum state $|\psi\rangle$ can be expressed as a linear combination of two orthogonal states $\psi = c_\alpha |\alpha\rangle + c_\beta |\beta\rangle$, where c_α, c_β are complex coefficients whose absolute squared magnitudes sum to one $|c_\alpha|^2 + |c_\beta|^2 = 1$, and $|\alpha\rangle, |\beta\rangle$ are the two basis vectors. Since any 2x2 Hermitian matrix can be expanded as a linear combination of the three Pauli matrices, $\sigma^x, \sigma^y, \sigma^z$ and the identity matrix (which I will denote as σ^0), this means that any Hamiltonian within this two-dimensional Hilbert space can be mapped to:

$$\mathcal{H}_{\mathrm{TLS}} = \sum_{\mu=0,x,y,z} C_\mu \sigma^\mu, \tag{1.1}$$

where $\{C_\mu\}$ are real scalar coefficients. If one considers this Hamiltonian in the basis $|\uparrow\rangle, |\downarrow\rangle$ that is diagonal in σ^z, one can separate these four terms into: a constant energy offset $C_0\sigma^0$ that can be subtracted without affecting the system dynamics, a diagonal term $C_z\sigma^z$, and two off-diagonal terms $C_{x,y}\sigma^{x,y}$. Without loss of generality, one can rotate into a frame in which $C_y = 0$, and be left with the single-particle Hamiltonian for an Ising spin in a transverse field:

$$\mathcal{H}^{(1)} = -|\mu|h^z\sigma^z - \Gamma\sigma^x, \tag{1.2}$$

where $|\mu|h^z\sigma^z$ can be thought of as an energy splitting due to the Zeeman interaction of a magnetic dipole with moment $|\mu|$ and field h^z, and $\Gamma\sigma^x$ induces a tunnel splitting between the two Ising states $|\uparrow\rangle, |\downarrow\rangle$. In the Ising basis, the Zeeman splitting changes the relative rate of complex phase accumulation between the two Ising states with frequency $\sim |\mu|h^z$, and the tunneling splitting induces quantum fluctuations between the two states with rate $\sim \Gamma$. Colloquially, one can think of this problem as a spin-1/2 particle in a longitudinal field with interaction strength $-|\mu|h^z$, and a transverse field with interaction strength Γ, and so I will use to denote a longitudinal interaction, $z \leftrightarrow \|$, and to denote a transverse interaction, $x \leftrightarrow \perp$, interchangeably.

A many-body Hamiltonian can be constructed by taking a sum of the independent single-particle Hamitonians $\mathcal{H}_i^{(1)}$ and two-spin interaction terms $\mathcal{H}_{ij}$

$$\mathcal{H}_{\text{tot}} = \sum_i \mathcal{H}_i^{(1)} + \sum_{ij} \mathcal{H}_{ij}, \tag{1.3}$$

where $\mathcal{H}_{ij}$ represents the interaction term between spins i and j. Just as observables for the single particle Hamiltonian can be expanded as a linear combination of the σ^μ matrices (including σ^0 as the identity matrix), two-spin interaction terms can be represented as linear combinations of the product terms $\sigma^\mu\sigma^\nu$, giving the general form:

$$\mathcal{H}_{ij} = \sum_{ij} \sum_{\mu,\nu=0,x,y,z} V_{ij}\sigma_i^\mu\sigma_j^\nu, \tag{1.4}$$

where $V_{ij}^{\mu\nu}$ sets the strength of the interaction for each term. Inserting the single-particle Hamiltonian from before, ones arrives at the most general form of the transverse field Ising model:

$$\mathcal{H}_{\text{tot}} = -\sum_i |\mu_i|h_i^z\sigma_i^z - \sum_i \Gamma_i\sigma_i^x + \sum_{ij} \mathcal{H}_{ij}, \tag{1.5}$$

where I have let the magnetic moment μ_i, the longitudinal field h_i and the transverse field Γ_i vary from site to site. While μ_i in real systems will be a function of the local magnetic field $\vec{h}(\vec{r}_i)$, if it does not vary much, this can be approximated by a

constant magnetic moment $\mu_i \to \mu$. Furthermore, in the lab, a uniform magnetic field is frequently applied via external magnets, and it is convenient to split each term into a spatially uniform term, and a spatially varying term. While spatially-varying external fields are generally weak in the experimental setting, they are nonetheless useful to consider theoretically, since interaction terms in the Hamiltonian can be approximated in the semi-classical limit of a classical moment sourcing a classical field onto a quantum spin. In this case, the spatially-varying term becomes a very complicated object that depends on the instantaneous state of each spin, so it is usually replaced by a stochastic variable drawing from some underlying distribution– usually a Gaussian with fixed variance for ease of computation. One can construct a random-field type Hamiltonian:

$$\mathcal{H}_{\text{tot}} = -|\mu| \sum_i (h_0^z + h_i^z)\sigma_i^z - \sum_i (\Gamma_0 + \Gamma_i)\sigma_i^x + \sum_{ij} \mathcal{H}_{ij}, \tag{1.6}$$

where h_0^z, Γ_0 are spatially invariant constants, and h_i^z, Γ_i are site-dependent random variables drawn from a fixed underlying distribution. One quantitative way of introducing disorder into a system is through increasing the variance of the random field terms h_i^z, Γ_i.

In principle, while all interaction terms $\sim \sigma_i^\mu \sigma_j^\nu$ are allowed in $\mathcal{H}_{ij}$, there are often some assumptions made theoretically about which terms are non-negligible. In particular, the term $V_{ij}^{zz}\sigma_i^z\sigma_j^z$ corresponds to the classical interaction between two Ising spins (lying along the z axis), and is often the only term considered. Furthermore, $V_{ij}^{\mu\nu}$ is frequently approximated as short-range, where $V_{ij}^{\mu\nu} \neq 0$ if and only if spins i and j are nearest-neighbors. With both of these approximations, along with the assumption that $\Gamma_i = 0$, one arrives at the traditional random field Ising model (RFIM):

$$\mathcal{H}_{\text{RFIM}} = -|\mu| \sum_i (h_0^z + h_i^z)\sigma_i^z - \sum_i \Gamma\sigma_i^x + \sum_{ij} \mathcal{H}_{ij}^{zz}\sigma_i^z\sigma_j^z. \tag{1.7}$$

While this model is simplified from any real physical case, it nonetheless exhibits a remarkable display of quantum phenomena, as having non-commuting terms σ^z, σ^x generates quantum fluctuations, while the interaction term $\mathcal{H}_{ij}$ generates quantum entanglement. I will use the RFIM as a base point to understand the $LiHo_xY_{1-x}F_4$ system, and specifically point out where it falls short and quantum corrections are

needed (specifically, off-diagonal interaction terms $\sim \sigma_i^z \sigma_j^x$ and $\sim \sigma_i^z \sigma_j^0$ come into play).

1.2 The $LiHoF_4$ Single Ion Hamiltonian

$LiHoF_4$ is an electrically-insulating compound whose magnetic properties are almost entirely determined by the unpaired $4f$ electrons of the Ho^{3+} ion. These unpaired electrons do not pair off into a singlet state, but rather into a composite, finite moment. Unlike the s and d-shell electrons which can conduct electricity through de-localized Bloch states, the f-shell electrons are strongly localized, and act as localized moments on a lattice.

The dominant terms in the Ho^{3+} electronic Hamiltonian are exchange and Coulomb interactions, as the $4f$ states are so tightly confined. The Ho^{3+} ion has 10 $4f$ electrons, each with its own spin s_i and orbital angular momentum l_i. The strong exchange and Coulomb interactions hybridize all of these particles into one composite spin $S = \sum_i s_i$ and orbital angular momentum $L = \sum_i l_i$. For $LiHoF_4$, the ground state multiplet ${}^{2S+1}L_J$ is given by Hund's rules, which gives a $J = 8$ ground state multiplet with 17-fold degeneracy.

This 17-fold degenerate ground state multiplet is split due to interactions with the electric fields from neighboring ions, through a "crystal field" term $\mathcal{H}_{\text{cf}}$ in the Hamiltonian. While $\mathcal{H}_{\text{cf}}$ is difficult to calculate from first principles, its form can be simplified through discarding all terms that do not obey the underlying crystal symmetry. In the case of $LiHoF_4$, there is a tetragonal scheelite crystal structure with space group $I4_1/a$.

One can expand the crystal field potential in a multipole expansion, and recast this in terms of the Stevens operators, which consist of linear combinations of the operators J^z, J^+, J^-, J^2. I refer the reader to [40] for a derivation of these Stevens operators.

In the case of $LiHoF_4$, the crystal field Hamiltonian is given by

$$\mathcal{H}_{\text{cf}} = \sum_{l=2,4,6} B_l^0 O_l^0 \sum_{l=4,6} (B_l^4(c) O_l^4(c) + B_l^0(s) O_6^4(s)) \tag{1.8}$$

with corresponding Stevens operators $O_l^m(c/s)$ defined according to [40]. While there are many measurements of the crystal field parameters from ac magnetic susceptibility [8, 40], optical scattering [18, 36], and EPR [67], I will use the parameters from the neutron scattering measurements of [61].

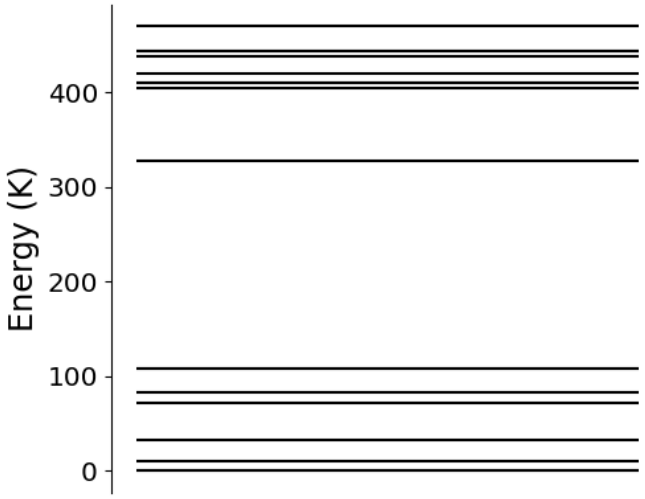

Figure 1.1: Level diagram of the $J = 8$ manifold degeneracy lifted by $\mathcal{H}_{\text{cf}}$. There is an ~ 11 K gap to the first excited state, giving rise to a two-dimensional low-energy effective Hamiltonian.

Diagonalizing this Hamiltonian, one finds a ground state doublet with an ~ 11 K gap to the first excited state. I plot the energy levels in Figure 1.1. The second excited state is > 10 K above the first excited state as well. This means that at temperatures $\ll 10$ K, the single-ion Hamiltonian is well approximated by a lower-dimensional effective Hamiltonian whose Hilbert space corresponds to the subspace of the full $\mathcal{H}_{\text{cf}}$ spanned by the two degenerate ground states. Since this Hilbert space is two-dimensional, one can naturally map the problem onto the problem of a spin-1/2 particle.

It turns out that $\mathcal{H}_{\text{cf}}$ is highly anisotropic, and consequently each of the ground states has an expectation value of its total angular momentum $\vec{J}$ completely aligned along the z axis (crystallographic c). In other words, $\langle J^x \rangle \approx \langle J^y \rangle \approx 0$. Furthermore, both states have equal and opposite z-components of their angular momenta, with $\langle J^z \rangle \approx \pm 5.51$. Intuitively, this corresponds to a classical Ising spin, with renormalized moment $g_{\parallel} = 2 g_L \langle \uparrow | J^z | \uparrow \rangle$, where $g_L = 5/4$ is the Landé g-factor, and one can denote the two states $|\uparrow\rangle$ and $|\downarrow\rangle$. I plot visualizations of these states as projected onto the J^z eigenbasis. I plot in Figure 1.2 a visualization of the two ground states projected onto the J^z eigenbasis. This strong of a crystal anisotropy is rarely found in nature, and can be quantified as the ratio of the two g-factors:

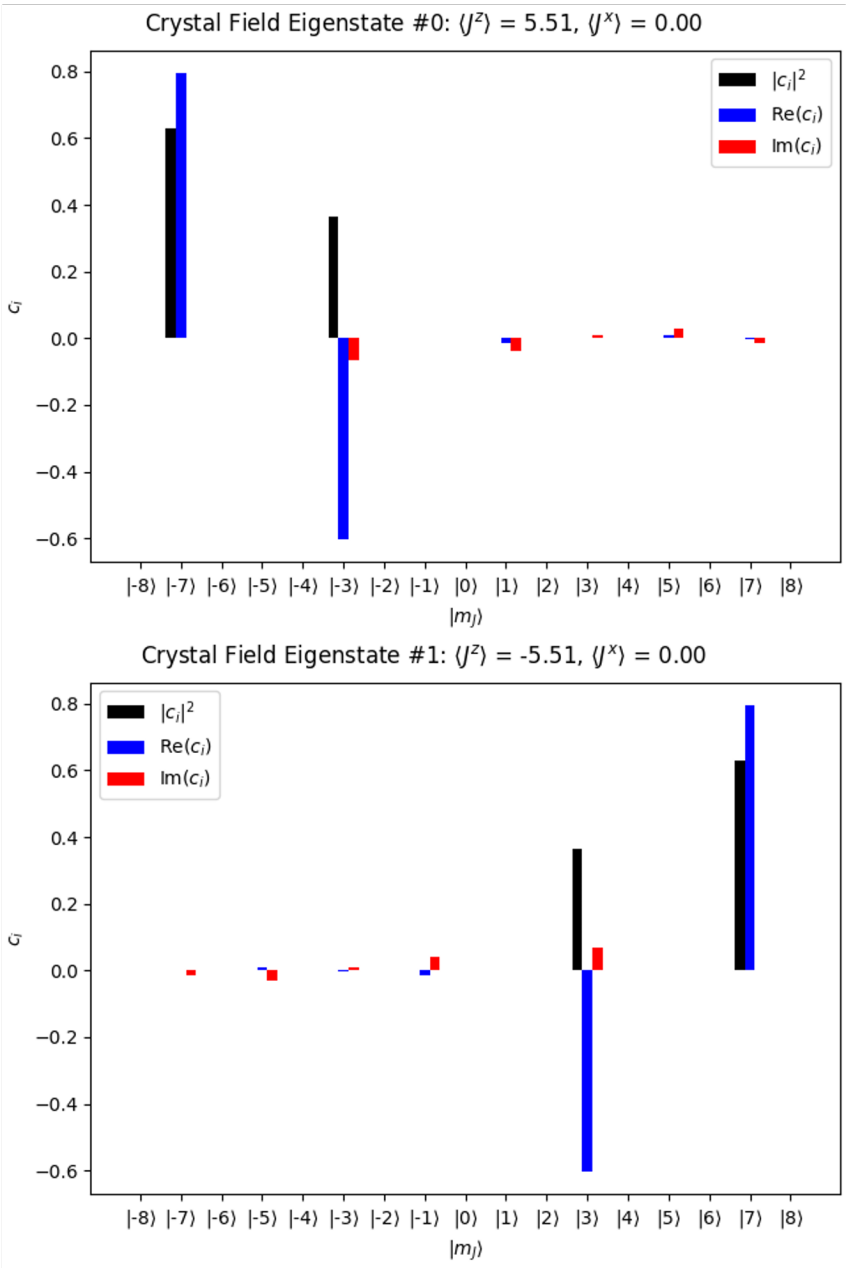

Figure 1.2: Visualization of the electronic ground state doublet of $\mathcal{H}_{\text{cf}}$ in zero external field, with $|\uparrow\rangle$ in **a** and $|\downarrow\rangle$ in **b**. Shown are the coefficients of each state when projected onto the J^z eigenbasis, with the real part in blue, imaginary part in red, and absolute square magnitude in black. $|\uparrow\rangle$ is approximately 2/3 occupation of $|m_J = 7\rangle$ and 1/3 occupation of $|m_J = 3\rangle$ with an approximate π phase between them, giving rise to a state with $\langle J^z\rangle \approx 5.51$ and $\langle J^x\rangle \approx \langle J^y\rangle \approx 0$.

$g_\parallel/g_\perp = 13.8/0.74 = 18.6$ [12].

Following Chakraborty [17], one can make what is known as the "Ising approximation", in which all of the 17-dimensional J^μ operators corresponding to the physical observables are mapped to linear combinations of Ising variables σ^μ acting upon the subspace spanned by the ground state doublet. One can write

$$J^\mu = \sum_{\nu=0,x,y,z} C_{\mu\nu}\sigma^\nu, \tag{1.9}$$

where each coefficient $C_{\mu\nu}$ is also a function of the applied magnetic field. However, while this will renormalize the mapping for different external field strengths, for experimentally-accessible field values the gap to the first excited state remains sufficiently large that the spins maintain their two-state nature, making the Ising approximation justified for all field values.

If one takes the Zeeman interaction and projects it down to the Ising subspace, one is left with the Hamiltonian

$$\mathcal{H}_{\text{Zeeman}} = g_L\mu_B \sum_\mu B^\mu J^\mu \rightarrow g_L\mu_B \sum_{\mu\nu} C_{\mu\nu}B^\mu\sigma^\nu. \tag{1.10}$$

However, only some of these terms are finite, and in order to see the dominant effects, one can gain an intuitive understanding through examining the effects of longitudinal and transverse fields on the spin. First, if a longitudinal field is applied, there is a simple Zeeman splitting of the levels, whose splitting is linearly proportional to the external field. I plot in Figure 1.3 the dependence of the ground state doublet energies on a longitudinal field, showing that it behaves identically to a classical Ising spin with a renormalized moment $\mu_{\text{Ising}} = 6.88\mu_B = 4.61$ K/T.

The dependence on transverse field is more complicated. I plot in Figure 1.4 the doublet levels as a function of external transverse field. The effect of the transverse field can be split into two parts: one that changes the average energy of both of the states $E_{\text{cm}}(B^x)$, and one that induces a tunnel splitting $\Delta(B^x)$ between the two. This splitting is responsible for quantum fluctuations, and arises from quantum mechanically mixing the excited crystal field states with the ground state doublet. For transverse fields ≤ 1 T, both of these are well approximated by a quadratic form with $E_{\text{cm}}(B^x) = -5.35\text{mK}(B^x/kG)^2$ and $\Delta(B^x) = 2.67\text{mK}(B^x/kG)^2$.

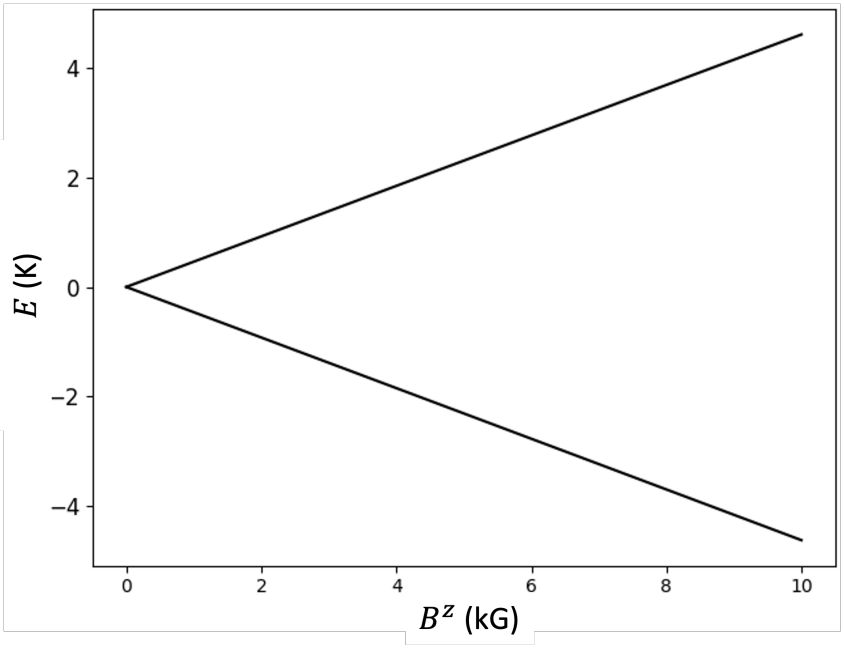

Figure 1.3: Dependence of the ground state doublet energies on a longitudinal field, showing behavior identical to a classical Ising spin with a renormalized moment $\mu_{\text{Ising}} = 6.88\mu_B = 4.61$ K/T.

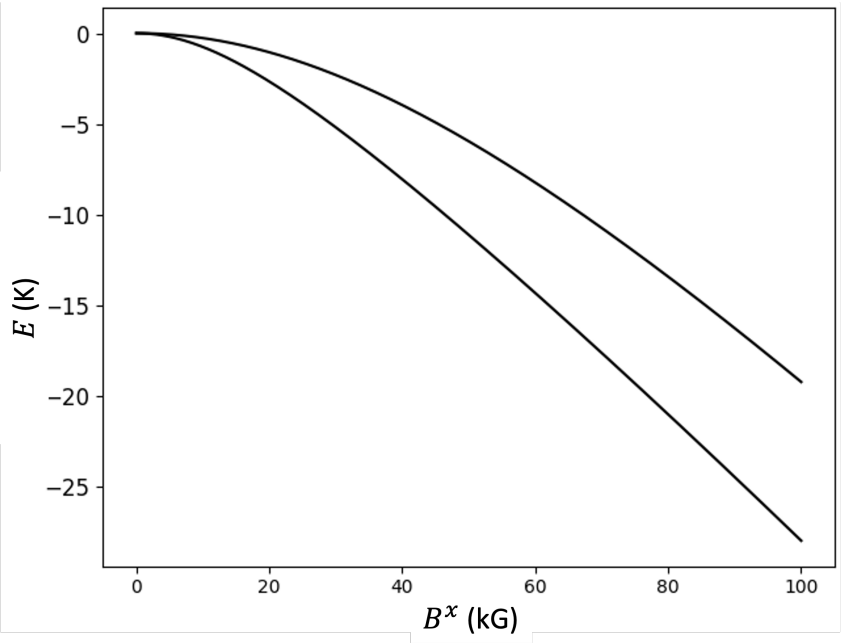

Figure 1.4: Dependence of the ground state doublet energies on a transverse field. The transverse field both lowers the average energy $E_{\text{cm}}(B^x)$ and induces a tunnel splitting $\Delta(B^x)$ that, for fields $\leq$ 1 T is well approximated by $E_{\text{cm}}(B^x) = -5.35\text{mK}(B^x/kG)^2$ and $\Delta(B^x) = 2.67\text{mK}(B^x/kG)^2$.

Now I consider a spin in a fixed transverse field and a varying longitudinal field. For high longitudinal fields, the Zeeman splitting is much greater than the tunnel splitting $E_{\text{Zeeman}}(B^z) \gg \Delta(B^x)$, and the eigenstates are essentially the Ising eigenstates $|\uparrow\rangle, |\downarrow\rangle$, whose energy splitting is linear in the longitudinal field. However, as the longitudinal field is decreased and the spin comes into resonance, there is an avoided level crossing as the eigenstates are now quantum superpositions of the two original Ising states. In this regime, where $E_{\text{Zeeman}}(B^z) \leq \Delta(B^x)$, the system is in resonance, and will tunnel between states with a rate given by Fermi's golden rule $\Gamma \sim \Delta(B^x)$.

1.3 Spin-Spin Interactions and the Dipolar Coupling

The individual spins in $LiHoF_4$ interact primarily through the magnetic dipolar interaction–a long-range anisotropic interaction that generates quantum entanglement between spins. I now consider the dipolar interaction term,

$$\mathcal{H}_{ij} = \frac{\mu_0 g_L^2 \mu_B^2}{4\pi} L^{\mu\nu}(\vec{r}_{ij}) J_i^\mu J_j^\nu, \tag{1.11}$$

between electronic spins J_i and J_j. $\mu_0 = 4\pi 10^{-7} \frac{\text{N}}{\text{A}^2}$ is the permeability of free space, $\mu_B = \frac{2}{3}\frac{\text{K}}{\text{T}}$ the Bohr magneton, $g_L = 5/4$ the Landé g-factor, and dipole-dipole matrix element $L^{\mu\nu}(\vec{r}_{ij}) = \frac{\delta_{\mu\nu}|\vec{r}|^2 - 3r^\mu r^\nu}{|\vec{r}|^5}$ evaluated at relative coordinate $\vec{r} = \vec{r}_{ij} = \vec{r}_i - \vec{r}_j$.

$LiHoF_4$ has a body-centered tetragonal crystal structure with lattice constants $a = 5.175$ and $c = 10.75$ and four Ho^{3+} ions per unit cell [37, 51]. In terms of the unit cell coordinates (a, a, c), their positions are at $(0, \frac{1}{2}, \frac{3}{4})$, $(0, 0, \frac{1}{2})$, $(\frac{1}{2}, 0, \frac{1}{4})$, $(\frac{1}{2}, \frac{1}{2}, 0)$. This amounts to a minimal distance of $\Delta r_{\text{min}} \approx 3.73$ between two Ho^{3+} ions. The corresponding magnetic interaction energy is $A_{\text{dip}} = 18.5$ mK.

If one maps the physical spin variables to the Ising spin-1/2 variables $J_i^\mu \rightarrow \sum_\nu C_{\mu\nu}\sigma_i^\nu$, the interaction term gets mapped to

$$J_i^\mu J_j^\nu \rightarrow \sum_{\alpha\beta} C_{\mu\alpha}\sigma_i^\alpha C_{\nu\beta}\sigma_j^\beta, \tag{1.12}$$

with $4 \times 4 = 16$ different terms due to the different combinations of Ising spin operators, and with each coefficient $C_{\mu\nu}$ being a function of the external magnetic field. However, due to the crystal anisotropy, not all terms have the same magnitude, and this expression can be approximated by dropping the weakest terms. Through numerical diagonalization, one can find that the largest effective interaction term is $J_i^z J_j^z \sim C_{zz}^2 \sigma_i^z \sigma_j^z$, which is larger than any other interaction term by two orders of

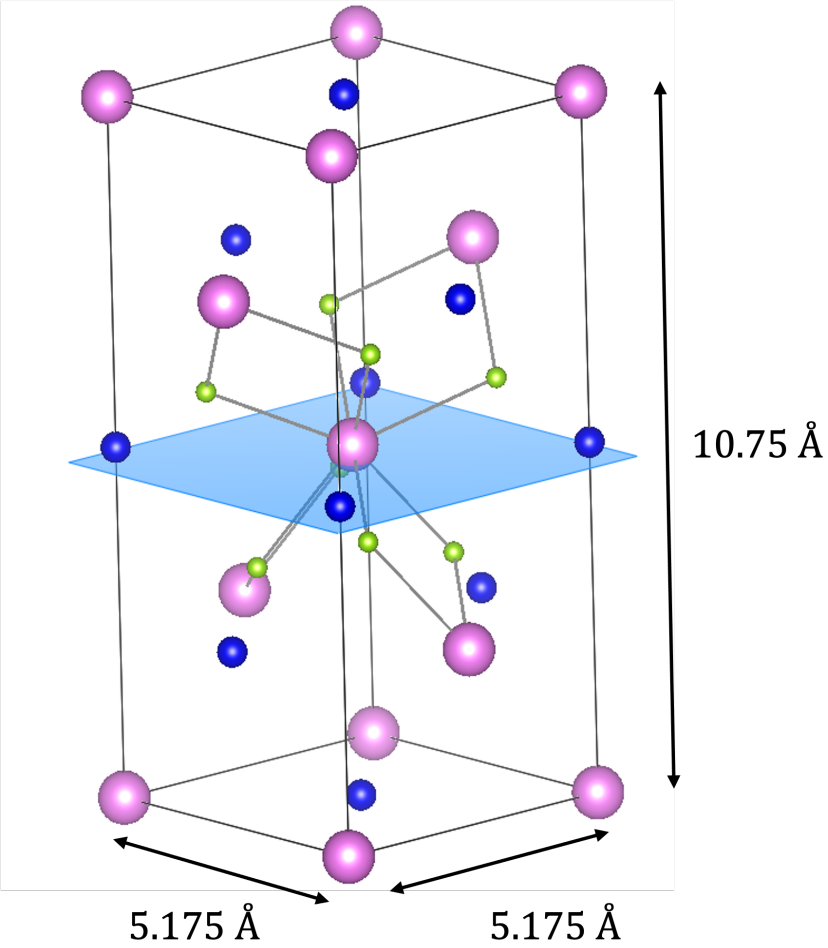

Figure 1.5: Crystal structure of $LiHoF_4$ with Ho^{3+} ions as the large pink spheres.

magnitude for the entire range of experimental fields, and so, within $\sim 1\%$ accuracy, the dipolar interaction can be well approximated by the Ising interaction,

$$\mathcal{H}_{ij}^{\text{Ising}} = \frac{\mu_0 g_L^2 \mu_B^2}{4\pi} L^{zz}(\vec{r}_{ij}) C_{zz}^2 \sigma_i^z \sigma_j^z, \tag{1.13}$$

that gives the interaction energy between two classical Ising moments. While this Ising approximation to the dipolar interaction captures much of the qualitative behavior of the phase diagram for $LiHoF_4$, some phenomena can only be explained by going past this Ising approximation, and using off-diagonal terms in the dipolar interaction. In particular, the term $\sim J_i^z J_j^x$ can be intuitively understood as one spin J_i^z sourcing a classical transverse field B^x on spin j, which has a term $\sim C_{zz} C_{0x} \sigma_i^z$ that lowers the energy of spin j, and $\sim C_{zz} C_{xx} \sigma_i^z \sigma_j^x$ that induces a tunnel splitting (and thus quantum fluctuations) on spin j. The former already has been proven

necessary in quantitatively matching Monte Carlo calculations of the phase diagram to experiment [28], while I will show in a later chapter that the latter term is important in resonant cluster excitations.

The dipole-dipole interaction $L^{\mu\nu}(\vec{r}_{ij})$ has two interesting properties, which dramatically complicate system dynamics. First, the interaction strength $L(\vec{r}_{ij})$ dies as $\sim \frac{1}{|\vec{r}|^3}$, and is thus long-range. If one integrates the dipolar interaction over a sphere with radius R, since the area of a spherical shell scales as $\sim R^2$, the integral diverges logarithmically as $\int_0^R dr \frac{1}{r} \sim \log R$, and the dynamics of any single spin depends not only its neighboring spins, but on all of the spins within the crystal. Alternatively, this means that the full many-body system will have eigenstates at many different excitation energies covering many orders of magnitude.

Furthermore, the dipolar interaction is anisotropic in nature, with ferromagnetic ($J < 0$) coupling when the two spins lie along the Ising axis, and antiferromagnetic ($J > 0$) when spins lie in the plane. Because of this, the dipolar interaction can lead to frustration, in which the system has many nearly-degenerate ground states since local spin configurations cannot satisfy all favorable Ising couplings simultaneously.

1.4 Disorder and the $LiHo_xY_{1-x}F_4$ Phase Diagram

Below the Curie temperature $T_c \approx 1.53$ K, $LiHoF_4$ orders ferromagnetically due to the dipolar interaction between spins [23]. While the full spherical dipolar sum is antiferromagnetic, $LiHoF_4$ nonetheless self-organizes into long needle-like ferromagnetic domains, as observable in scanning Hall probe measurements taken from [43] and plotted in Figure 1.6, and magneto-optic images taken from [52]. The $\sim \mu$m size maximizes the ferromagnetic axial dipolar coupling, and has a branching structure at higher fields, in which smaller shallow domains are formed within existing domains spanning the length of the sample.

This ferromagnetic order can be broken either with thermal fluctuations, or by introducing quantum fluctuations through the application of an external transverse field. At $T = 0$, there is a quantum critical point at $B^x \approx 4.9$ T. The $H_\perp$-T phase diagram is plotted in Figure 1.8. While $LiHoF_4$ behaves like a mean-field ferromagnet (dashed line in Figure 1.8) at higher temperatures, as $T < 500$ mK, the phase boundary departs from the purely electronic mean-field value upward to a higher transverse field. This increased critical transverse field arises from the hyperfine interaction between electronic and nuclear spins, which effectively locks nuclear and electronic spins together, giving an effective renormalized moment.

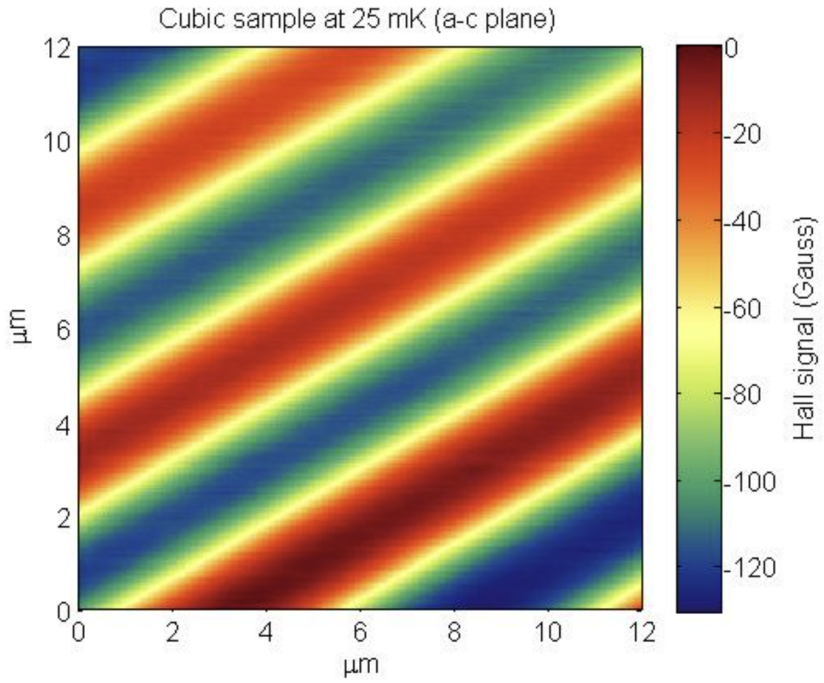

Figure 1.6: Scanning Hall probe image of $LiHoF_4$ domains taken from [43], taken on the a-c plane of the sample at $T = 25$ mK.

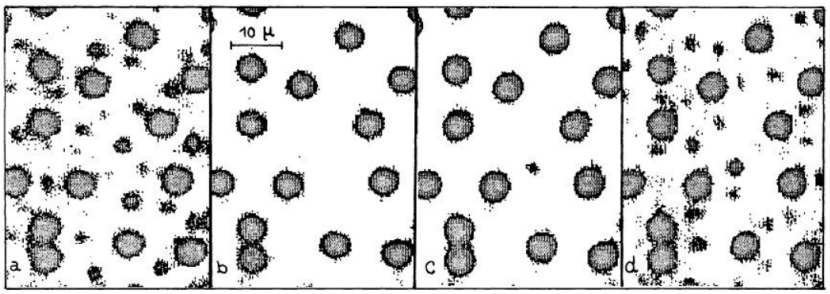

Figure 1.7: Magnetooptic images of $LiHoF_4$ domains taken from [52] with a longitudinal field of 0.7 T and a temperature of 1.3 K with image focused at: **a** the top surface, **b** half the sample thickness, **c** 3/4 of the sample thickness, and **d** the bottom surface. The images show continuous needle-like domains throughout the entire sample, as well as smaller branching domains that do not penetrate the bulk.

This is reflected by a mean-field calculation including the hyperfine interaction (solid line in Figure 1.8).

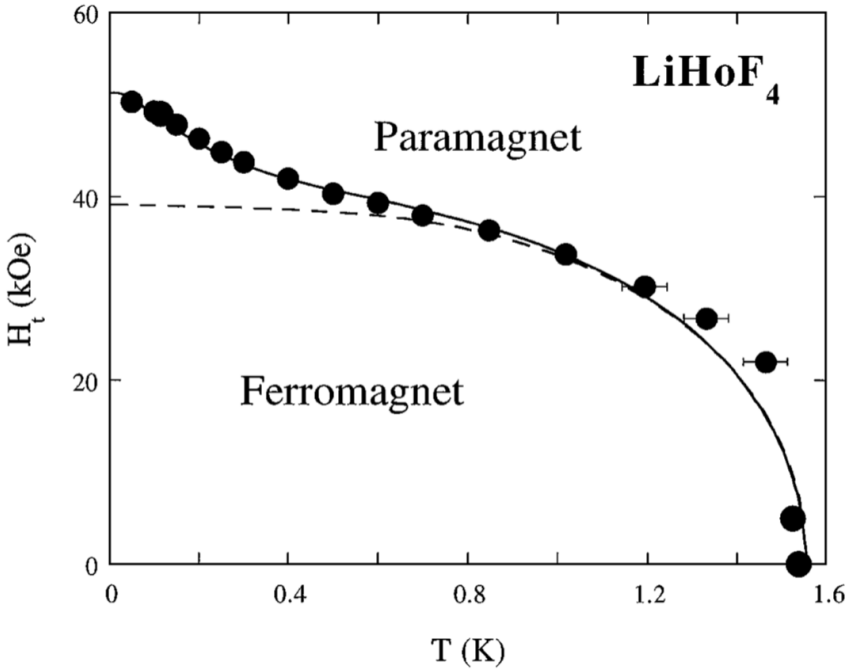

Figure 1.8: Phase diagram of $LiHoF_4$ as computed from susceptibility measurements from [12] showing the ferromagnetic (FM) to paramagnetic (PM) transition, with a quantum critical point at $B^x \approx 4.9$ T and a classical critical point at the Curie temperature $T_c \approx 1.53$ K. Filled circles are the experimental phase boundary, the dashed line is a mean-field theory solution using only the electronic spin degrees of freedom, and the solid line is a full mean-field theory incorporating the nuclear hyperfine interaction.

The $LiReF_4$ family has the convenient property that its bonding chemical properties are relatively independent of the choice of rare-earth ion Re. Because of this, one can chemically substitute some fraction $1 - x$ of the Ho^{3+} ions with non-magnetic Y^{3+} ions, which do not carry an electronic moment. This gives the diluted compound $LiHo_xY_{1-x}F_4$, which has quenched spatial disorder that can be represented by the site-diluted Ising model (SDIM), in which each spin variable $\sigma_i^\mu \rightarrow \epsilon_i \sigma_i^\mu$ now carries an occupation number $\epsilon_i \in \{0, 1\}$ depending on whether the site is occupied by a Ho^{3+} ($\epsilon_i = 1$) or a Y^{3+} ($\epsilon_i = 0$).

For modest dilutions $x \geq 0.5$, the primary effect of the dilution is to re-scale the dipolar interaction strength. As the chemical concentration goes down, the Ho^{3+} ions become farther and farther apart, and the average dipolar interaction $|V_{\text{dip}}| \sim x$

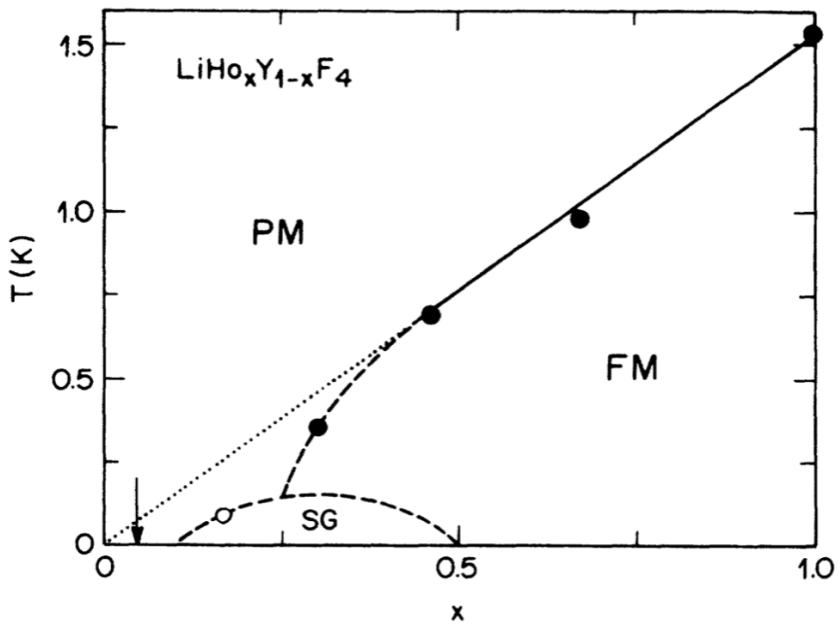

Figure 1.9: Phase diagram of $LiHo_xY_{1-x}F_4$ at zero transverse field as a function of Ho^{3+} concentration x and temperature T taken from [60]. For $x > 0.5$ the system behaves as a mean-field ferromagnet with Curie temperature $T_c \sim x$ scaling linearly with x. For lower concentrations $x < 0.3$, $LiHo_xY_{1-x}F_4$ undergoes a spin glass transition, and at even lower concentrations and the appropriate thermal boundary conditions, $LiHo_{0.045}Y_{0.955}F_4$ enters a "decoupled cluster glass" phase denoted by the arrow.

scales linearly with the Ho^{3+} concentration x. I reproduce the T-x phase diagram for the diluted $LiHo_xY_{1-x}F_4$ from [60] in Figure 1.9.

However, the quenched disorder from chemical dilution has more profound effects than simply renormalizing the dipolar interaction strength. For the pure compound $LiHoF_4$, the crystal symmetry can cancel out the dipolar contribution on any spin from its nearest neighbors. When considering the local environment on a single spin, disorder has the effect of increasing the distribution in local fields, both longitudinal and transverse, that any given spin experiences. Translated into our Ising model, this can result in site-dependent random fields which can induce either random field pinning (for local fields) or increased quantum fluctuations (for transverse fields

In the ferromagnetic state, the emergent effective low-energy degrees of freedom for $LiHo_xY_{1-x}F_4$ are the boundaries between ferromagnetic domains of opposite sign, known as domain walls. If a longitudinal field is applied to the ferromagnet, domains aligned with the field will tend to grow, while anti-aligned domains will

tend to shrink, which can be mapped to the motion of a domain wall. While a rigid planar wall is an idealization, and any real domain wall will have finite elasticity, and hence a finite roughness, for dipolar-coupled ferromagnets, the long-range nature of the dipolar-interaction tends to produce long, flat domain walls. This is experimentally confirmed from the domain images of [43, 52] in the case of the pure sample $LiHoF_4$, but remains an open question for the domain wall structure for the disordered ferromagnet $LiHo_xY_{1-x}F_4$. However, even though the domain wall is more complicated than a simple one-dimensional particle moving linearly, the dynamics are nonetheless described by a domain wall moving in a random potential sourced by random longitudinal fields. In chapter 3 I will examine measurements performed to probe the motion of these domain walls in the disordered ferromagnet $LiHo_xY_{1-x}F_4$.

For lower concentrations $x < 0.5$, these effects become important, and $LiHo_xY_{1-x}F_4$ departs from mean-field ferromagnetic behavior, with a suppressed $T_c(x < 0.5) < xT_c(x = 1)$ compared to the mean-field prediction. At low enough concentrations and temperatures, $LiHo_xY_{1-x}F_4$ enters a spin-glass phase, in which the system does not develop any long-range order, but whose dynamics progressively freeze out at lower and lower temperatures and become non-ergodic.

At even lower concentrations $x = 0.045$, the system dynamics become strongly dependent on the thermal heat-sinking [64]. When put in direct contact with strongly heat-sunk sapphire rods, the sample can dissipate energy through interactions between the sample phonons and the sapphire rods. This sets an effective phonon linewidth Γ, which changes the rate of dissipative, incoherent spin flips due to phonon scattering. Alternatively, if the sapphire rods are pulled apart from direct contact, the sample can only exchange energy with a Hysol epoxy form, whose polymer structure significantly reduces its thermal conductivity in comparison to the sapphire, thus reducing Γ, and consequently, dissipation rates. An illustration of these two heat-sinking configurations are reproduced in Figure 1.10.

In these two heat-sinking regimes, the difference in behavior can be seen in Figure 1.11, reproduced from [64], which shows the temperature dependence on the imaginary susceptibility for different sets of data in different heat-sinking configurations. The left panel of 1.11 shows the frequency f_p at which $\chi''(f)$ is a maximum as a function of inverse temperature. For higher temperatures, all samples follow the same thermally-activated Arrhenius form, while at lower temperatures some samples depart from Arrhenius, as the weak dissipation prevents the $LiHo_xY_{1-x}F_4$ phonon

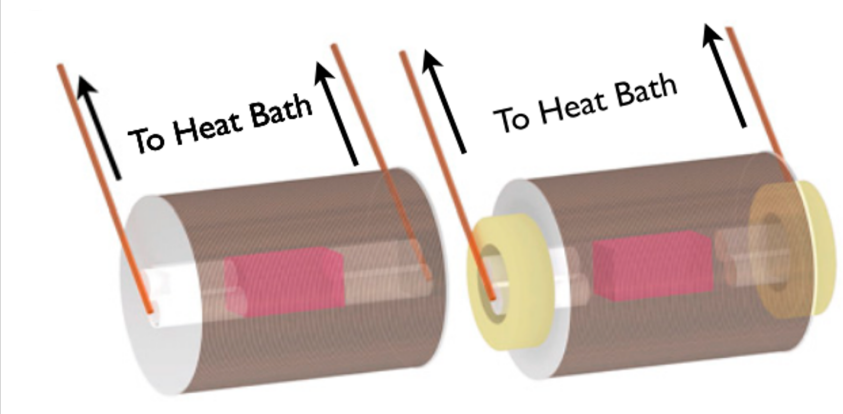

Figure 1.10: Schematic of the two heat-sinking configurations. The sample (pink cuboid) sits within a Hysol epoxy form (cylinder), and is either put in direct contact with sapphire rods that are connected to the heat bath through copper wire (left) or teflon spacers are added to pull the sapphire rods away from direct contact (right). Figure reproduced from [64].

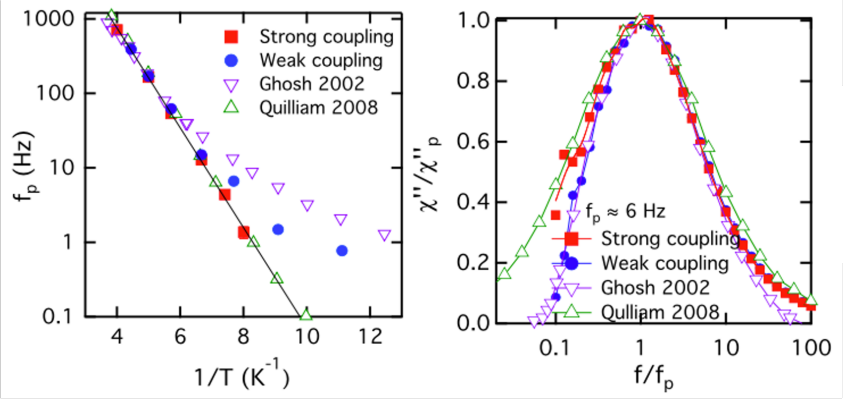

Figure 1.11: Effects of thermal boundary conditions on $LiHo_{0.045}Y_{0.955}F_4$. (Left) Peak frequency of imaginary susceptibility as a function of inverse temperature for the two configurations in Figure 1.12, compared with values published in [35, 59]. For weakly-coupled samples, the peak frequency departs from Arrhenius behavior below a certain temperature. (Right) Lineshapes of the imaginary susceptibility under different thermal conditions for the same peak frequency. Measurements in the weakly coupled thermal configuration show low-frequency spectral narrowing not observed in the connected configuration. Figure reproduced from [64].

bath from equilibrating with its environment, and it establishes a finite temperature gradient between the crystal and its environment, with the more weakly heat-sunk samples departing from Arrhenius at higher temperatures. On the right panel, at low enough temperatures, the weakly heat-sunk samples display spectral narrowing on the low-frequency end not typically seen in spin glasses. Furthermore, the width of the peak in χ'' narrows below 1.14 decades, the width predicted by Debye relaxation of a single time constant, indicating that the system cannot be described purely in terms of bulk relaxation processes. Instead, one can understand the weakly-coupled regime as a "de-coupled cluster glass", in which local spin clusters freeze together, and interact only weakly with neighboring spin clusters. I illustrate this in Figure 1.12. The left panel shows a glassy network of coupled spins in the strongly-coupled regime, while the right panel illustrates isolated spin clusters that are weakly-coupled together.

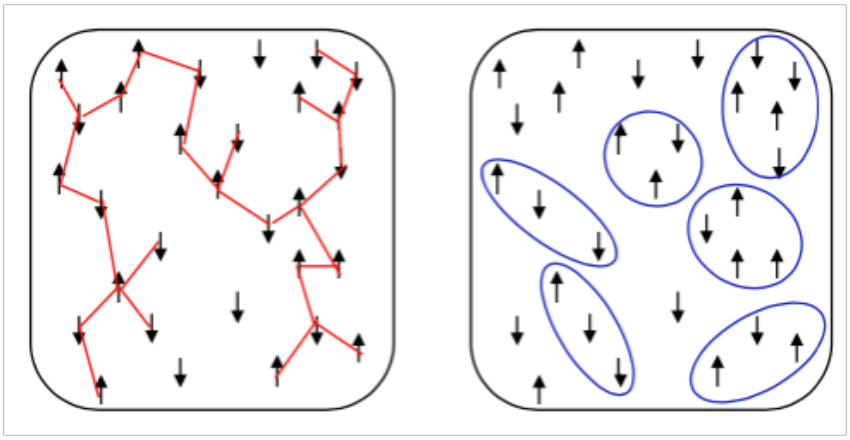

Figure 1.12: Cartoon of spin configurations in the two heat-sinking regimes. The left panel shows a glassy network of coupled spins in the strongly-coupled regime, while the right panel illustrates isolated spin clusters that are weakly-coupled. Figure reproduced from [64].

1.5 Dissipation and the Magnetoelastic Coupling

In order to study the dynamics of a system under an external drive field, one needs some estimate on the environmental induced dissipation, i.e., the dissipative transition rates $\gamma_{\alpha\to\beta}$ between two quantum states $|\alpha\rangle, |\beta\rangle$. The major source of dissipation for the magnetic moments in $LiHo_xY_{1-x}F_4$ is the coupling of the Ho^{3+} ions to lattice vibrations, i.e., phonons. In order to estimate the associated dissipation rates, I consider acoustic, Debye type low energy phonon modes, which are described by a wave vector $\vec{k}$, dispersion $\omega_{\vec{k}} = c|\vec{k}|$, Debye frequency ω_D, and

Debye temperature Θ_D.

Each phonon mode has a linewidth Γ, which describes the rate at which the mode exchanges energy with other phonons and the environment. Due to weak phonon-phonon interactions, the linewidth is dominated by the coupling of the sample to the environment. In recent experiments [64, 70], it has been pointed out that having a weak sample-environment coupling is crucial for the observation of hole burning and antiglass dynamics in driven $LiHo_xY_{1-x}F_4$. Here, I consider the lattice-environment coupling in terms of an effective phonon linewidth. Such a linewidth will set the lower bound for the magnetic dissipation rates and enable or disable the emergence of a Fano resonance. This yields a phenomenological explanation for the presence or absence of hole burning in several $LiHo_xY_{1-x}F_4$ experiments.

Acoustic phonons in the Debye model are described by the Hamiltonian

$$\mathcal{H}_D = \sum_{\vec{k}, c|\vec{k}|<\omega_D} c|\vec{k}| b^\dagger_{\vec{k}} b_{\vec{k}} \tag{1.14}$$

with bosonic ladder operators $b^\dagger_{\vec{k}}, b_{\vec{k}}$ at momentum $\vec{k}$. The linear coupling between the phonons and the magnetic states is typically of the form

$$\mathcal{H}_{\text{mag-ph}} = \sum_{\alpha,\beta,\vec{k}} g_{\alpha\beta}(\vec{k})(b^\dagger_{\vec{k}} + b_{\vec{k}})(|\alpha\rangle\langle\beta| + |\beta\rangle\langle\alpha|) \tag{1.15}$$

with coupling matrix elements $g_{\alpha\beta}(\vec{k})$ between different eigenstates $|\alpha\rangle, |\beta\rangle$ of the magnetic Hamiltonian.

The transition rate $\gamma_{\alpha\to\beta}$ between two magnetic states $|\alpha\rangle \to |\beta\rangle$ with energy difference $E_{\alpha\beta} \equiv E_\alpha - E_\beta$ can be estimated by Fermi's golden rule. It yields an energy-dependent decay rate $\gamma_{\alpha\beta} = \gamma(E_{\alpha\beta}) = \gamma(E)$ with

$$\begin{aligned}\gamma(E) &= -i \sum_{\vec{k}} |g(E,\vec{k})|^2 \left(\frac{n_{\vec{k}}}{E + i0^+ + c|\vec{k}|} + \frac{n_{\vec{k}}+1}{E + i0^+ - c|\vec{k}|} \right) \\ &= |g(E)|^2 (n_B(|E|) + \delta_{\text{sign}(E),1}) \rho_{\text{ph}}(|E|).\end{aligned} \tag{1.16}$$

Here $n_B(|E|)$ is the Bose-Einstein distribution at temperature T and energy $|E|$, $\rho_{\text{ph}}(|E|)$ is the phonon density of states, and $|g(E)|^2 \equiv g_{\alpha\beta}(c|\vec{k}| = E_{\alpha\beta}$.

For energy differences $E \ll k_B T$, the Bose function shows the typical $\frac{1}{E}$-divergence $n_B(|E|) \approx \frac{k_B T}{|E|} \gg 1$. For acoustic phonons at low energies, $g(|E|) = g_0\sqrt{|E|}$, which yields $\gamma(E) \approx g_0^2 k_B T \rho_{\rm ph}(|E|) = \gamma_D \frac{T\rho_{\rm ph}(|E|)}{\Theta_D \rho_{\rm ph}(\omega_D)}$, where γ_D is the decay rate at the Debye frequency. For a linear dispersion with linewidth Γ, the density of states in $d = 3$ dimensions is well approximated by $\rho_{\rm ph}(|E|) = \rho_0 E^2$ for $E \gg \sqrt{\Gamma\omega_D}$ and a constant $\rho_{\rm ph}(|E|) = \rho_0 \Gamma \Omega_D$ for $E \ll \sqrt{\Gamma\omega_D}$. In both cases the dissipation rate will be linearly proportional to temperature $\gamma \sim T$, but for small energies the dissipation will be constant in energy and linear in the phonon linewidth $\gamma \sim \Gamma$, while for large energies it will scale quadratically with energy $\gamma \sim E^2$

This allows for the dissipation rate at a fixed energy to be tuned in one of two ways. First, decreasing the temperature will decrease the dissipation. Second, if the energy is small enough, a constant floor can be set on the dissipation rate if the phonon linewidth is large enough compared to the phonon energy. This can be exploited in order to drive the system into a non-linear regime with energy scales that seem too weak upon first glance, and will be expanded upon in later chapters.

1.6 Conclusion

In this chapter, I have described the quantum two-level system, and how the rare-earth magnet $LiHo_xY_{1-x}F_4$ can be naturally mapped onto a quantum Ising system. $LiHo_xY_{1-x}F_4$ has an exotic phase diagram, with ground state behavior ranging from de-coupled spin clusters, to glassy relaxation, to long-range ferromagnetic ordering. However, while much of the ground state behavior can be determined through the use of the transverse field Ising model, off-diagonal terms in the dipolar interaction $\sim V^{zx} J_i^z J_j^x$ can give rise to new phenomena when looking at driven systems.

The rest of this thesis is divided into three chapters, with one chapter covering measurements made on the de-coupled cluster glass $LiHo_{0.045}Y_{0.955}F_4$ (in the weakly-coupled regime), the second covering measurements made on the disordered ferromagnets $LiHo_{0.65}Y_{0.35}F_4$ and $LiHo_{0.40}Y_{0.60}F_4$, and the final chapter providing a summary and prospects for future experiments.

In Chapter 2, I will show how off-diagonal terms in the dipolar interaction break the Ising symmetry of the crystal, and allow an ac magnetic field parallel to the Ising axis to drive the system into a non-linear response regime, dominated by resonant excitations of cluster levels in dilute $LiHo_{0.045}Y_{0.955}F_4$. I will discuss a spin dimer model that is capable of capturing the observed phenomena, including quantum interference (observed as asymmetric Fano resonances) and electromagnetically-induced

transparency (EIT), in which the interference between the excitation pathways completely destructively interferes and renders the sample transparent to the AC drive field.

In Chapter 3, I will show how noise measurements in the disordered ferromagnets $LiHo_{0.65}Y_{0.35}F_4$ can reveal the underlying free-energy surface determined by random field pinning, and how that affects the domain wall dynamics. Furthermore, I will show non-critical behavior in noise measurements on $LiHo_{0.40}Y_{0.60}F_4$, and argue that this non-critical behavior is a sign of novel quantum behavior, in which multiple macroscopic avalanches are nucleated by co-tunneling processes.

In the final chapter, I will delineate the major findings and their implications for future work.

Chapter 2

NON-LINEAR SPECTROSCOPY OF HIGH-Q SPIN CLUSTERS

This chapter describes experimental pump-probe spectroscopy measurements of $LiHo_{0.045}Y_{0.955}F_4$, in the "de-coupled cluster glass" phase (where weak heat-sinking to a thermal reservoir amplifies quantum effects). The dynamics depart from collective relaxation and must be described by a set of weakly-coupled spin clusters, each with its own unique eigenstates depending on the spatial positions of the spins which set the dipolar interaction. While linear dynamics can be interesting, it is known that driving systems into a non-linear response regime can result in exotic phenomena, where self-interactions become important.

For this reason, I turn to a set of pump-probe susceptibility measurements, in which a strong ac magnetic "pump" field drives the system into a non-linear regime, and a weaker ac magnetic "probe" field is used to interrogate the dynamics at other frequencies. This chapter begins with a brief theoretical review on generalized system susceptibilities, highlighting the importance of non-linear terms in the Taylor expansion of the susceptibility, and the difference between non-linearities arising from equilibrium vs non-equilibrium behavior.

These experiments can be described by analogy to traditional optical spectroscopy, but here applied to a many-body system in which there is a magnetic dipole transition as opposed to an electric dipole transition, and the relevant photon energies are of order $\sim$ 100 Hz ($\sim$ 1 nK, $10^{-12}eV$). Given a sufficiently strong external drive and sufficiently sharp phonon linewidth, the system can be driven out of equilibrium, where exotic phenomena such as non-linear susceptibility, tunable quantum interference, and electromagnetically-induced transparency (EIT) are observed.

2.1 Generalized Non-Linear Susceptibility

When a magnetic field is applied to $LiHoF_4$, the system responds by changing its own magnetization. Ignoring the spatial fluctuations of the sample and focusing on just the spatially-averaged bulk response, one finds that after waiting for initial transients to die down, if the external field $\vec{H}$ is small enough, the bulk magnetization $\vec{M}$ will be approximately linear with respect to that field

$$M^{\alpha} = \chi^{(1)}_{\alpha\beta} H^{\beta} \tag{2.1}$$

where $\chi^{(1)}$ is the linear susceptibility of the sample.

If, however, the external field is large enough, this linear approximation breaks down, and higher order terms in the susceptibility expansion must be included.

$$M^{\alpha} = \chi^{(1)}_{\alpha\beta} H^{\beta} + \chi^{(2)}_{\alpha\beta\mu} H^{\beta} H^{\mu} + \chi^{(3)}_{\alpha\beta\mu\nu} H^{\beta} H^{\mu} H^{\nu} + \ldots \tag{2.2}$$

In practice, systems frequently obey certain symmetry constraints, limiting which non-linear susceptibility terms $\chi^{(n)}$ are non-zero. In the Ising system $LiHoF_4$, the $\mathbb{Z}$-2 inversion symmetry of the spins forbids all even susceptibility terms, making the smallest order non-linear term $\chi^{(3)}$. For simplicity's sake, I will now assume that all spatial indices are the z-axis, i.e. I will focus on the longitudinal magnetization of the sample due to purely longitudinal fields and drop the implicit spatial indices, even though in principle there are other terms that generate spatially orthogonal responses to different field directions. In the specific case this becomes

$$M(t) = \sum_{i=1}^{\infty} M^{(i)}(t) = \sum_{i=1}^{\infty} \chi^{(i)} H^{i}(t) \tag{2.3}$$

with the implicit assumption that M is the component of the magnetization along the z-axis, and H is assumed to lie along the z-axis as well. One can Fourier transform both the magnetization and external fields:

$$\begin{aligned} M(\omega) &= \int_{\mathbb{R}} dt e^{-i\omega t} M(t) \\ H(\omega) &= \int_{\mathbb{R}} dt e^{-i\omega t} H(t) \end{aligned} \tag{2.4}$$

with reverse Fourier transforms

$$\begin{aligned} M(t) &= \int_{\mathbb{R}} \frac{d\omega}{2\pi} e^{i\omega t} M(\omega) \\ H(t) &= \int_{\mathbb{R}} \frac{d\omega}{2\pi} e^{i\omega t} H(\omega). \end{aligned} \tag{2.5}$$

While the linear response of the system only contains the spectral components that are present in the time-dependent drive field, the non-linear response naturally will mix frequencies and give rise to harmonics and sidebands in the full system response.

Furthermore, real systems are not instantaneous, and in general the system state will not depend solely on the instantaneous value of the external field, but also on the history of the external drive at previous times. One can replace the static susceptibilities $\chi^{(i)}$ with a time-dependent susceptibilities $\chi^{(i)}(\tau)$. This time-dependent response gives rise to dispersion, in which the susceptibility becomes frequency-dependent in the Fourier domain. The new history dependent response is given by

$$\begin{aligned} M^{(1)}(t) &= \chi^{(1)}(\omega)H(\omega) \\ M^{(3)}(t) &= \int_0^\infty \int_0^\infty \int_0^\infty d\tau_1 d\tau_2 d\tau_3 \chi^{(3)}(\tau_1,\tau_2,\tau_3) \\ &\quad \times H(t-\tau_1)H(t-\tau_2)H(t-\tau_3) \end{aligned} \tag{2.6}$$

with corresponding Fourier transforms

$$\begin{aligned} M^{(1)}(\omega) &= \int_0^\infty d\tau \chi^{(1)}(\tau)H(t-\tau) \\ M^{(3)}(\omega) &= \int_{\mathbb{R}}\int_{\mathbb{R}}\int_{\mathbb{R}} d\omega_1 d\omega_2 d\omega_3 \chi^{(3)}(\omega_1,\omega_2,\omega_3) \\ &\quad \times H(\omega_1)H(\omega_2)H(\omega_3)\delta(\omega-\omega_1-\omega_2-\omega_3). \end{aligned} \tag{2.7}$$

While the linear term only has non-zero spectral components at the driving frequencies, the first non-linear term $M^{(3)} \sim \chi^{(3)}$ responds not only at the driving frequencies $\{\omega_i\}$, but at new frequencies given by mixing the drive spectral components. If non-linearities are strong enough, their signature can be observed in the system response as higher harmonics of the drive frequencies, as well as sidebands if the system is driven with more than one tone.

In a two-tone pump-probe experiment, one can think of non-linearities as cross-terms between the two driving fields. While these non-linearities are unmistakably observable as spectral sidebands, the non-linearities will also affect the system response at the probe frequency. While there is a linear response $M^{(1)}(\omega_p) \sim \chi^{(1)}(\omega_p)$ at the probe frequency ω_p, the non-linear term $M^{(3)}(\omega_p) = \chi^{(3)}(\omega_p, \omega_d, -\omega_d)$ also has a non-zero response at the probe frequency. Because of this, in addition to the

obvious effects of non-linearities away from the probe frequency, there will be more subtle effects at the probe frequency that are not as immediately distinguishable from traditional linear effects. To see these effects, it is necessary to sweep the probe frequency across the pump frequency and observe the system response as a function of the detuning between the two frequencies.

While the above remains a general formulation for a system response that obeys causality, a specific solution for this linear susceptibility for the quantum many-body problem was discovered by Ryogo Kubo in 1957 [44], and is given by the Kubo formula, in which the dynamics are solved perturbatively:

$$\langle M(t)\rangle = \langle M\rangle_0 - \frac{i}{\hbar}\int_{t_0}^{t} dt' \,\langle [M(t), V(t')]\rangle_0 \,, \tag{2.8}$$

where $M(t)$ is the system bulk magnetization, $V(t)$ is the interaction energy of the external perturbation, and the brackets $\langle\rangle_0$ denote an equilibrium average with respect to the unperturbed Hamiltonian $\mathcal{H}_0$. This linear response only involves the zeroth order eigenfunctions of the unperturbed system, and is only dependent on the thermal states of the system, and not any non-equilibrium states. When the pump is not sufficiently strong and close enough to resonance with the probe field, the effect of the pump at the probe frequency is negligible, and the Kubo formula applies. However, with a strong enough pump and small enough detuning, the system enters a non-linear regime, and one must go past simple linear perturbation theory, and consider a picture that permits cross terms between the two time-dependent external fields.

One must quantify the field scales to enter the non-linear regime. For traditional AMO systems, one can usually estimate the drive strengths needed to enter a non-linear regime based on typical microscopic field scales in the problem [34]. For electric dipole transitions, this back-of-the-envelope estimate corresponds to typical electric fields within an atom, so it stands to reason that a reasonable non-linear field scale in the magnetic case would correspond to typical demagnetization fields within the lattice. However, the nearest-neighbor dipolar field is on the order of hundreds of Oe, while one can observe non-linear dynamics with a drive field several orders of magntiude smaller, on the order of hundreds of mOe. Indeed, the relevant energy scale is not the demagnetization field scale, but rather the decoherence rate due to (in $LiHo_xY_{1-x}F_4$) dissipative transitions mediated by phonons. In this way, the thermal boundary conditions are of crucial importance, because the phonon linewidth sets

the low-energy dissipation rates, which, in turn, determine whether the system can be driven into a non-linear regime.

2.2 Experimental Procedure

The susceptibility of the sample was measured using a custom high-purity (OFHC) Copper susceptometer designed and machined in-house, shown in Figure 2.1. The sample was mounted in the susceptometer, which was then mounted on the cold-finger of a Helium dilution refrigerator. While the susceptometer itself was machined out of copper, insulating coil forms were machined out of Hysol epoxy, which housed the sample. Furthermore, a uniform static transverse field was applied using an 8T superconducting solenoid sitting outside of the vacuum can. A time-dependent magnetic field was applied by driving a smaller solenoid in the susceptometer with an AC voltage, and a 1 kΩ current-limiting resistor to limit frequency-dependence in the driving field. The time derivative of the sample bulk magnetization was measured using another inductive coil nested inside of the drive solenoid, and a matching pair of coils was made and wired out-of-phase to null out the effect of the driving field itself and isolate the sample response. To do pump-probe spectroscopy, only a simple voltage summing amplifier is needed to add two sine waves at different frequencies simultaneously. For these measurements, the stronger pump field was of order ~ 0.5 Oe, while the probe field was more than an order of magnitude smaller at 0.02 Oe. The pump frequency was fixed at a frequency ~ 100 Hz, while the probe frequency was scanned around the pump frequency to determine the frequency response.

Due to the extremely narrow separation between the pump and probe frequencies ($\sim$ 1 mHz), disentangling the responses required the development of a two-stage lock-in technique, where the combined response is passed into a commercial lock-in amplifier tuned to the probe frequency, and the resulting output was sampled by a computer and passed through a software lock-in detector tuned to $\Delta f = f_{\text{pump}} - f_{\text{probe}}$. Due to Nyquist sampling criteria, all data reported here were sampled for a minimum time of $2/\Delta f$.

2.3 Raman Scattering of a Non-Linear Magnetic Crystal

One of the clear signatures of the non-linear response of a system is frequency-mixing. If a medium is driven with discrete spectral components defined by frequencies $\{\omega_{\text{input}}\}$, practically all systems will have linear response at those same driving frequencies, if non-linearities are strong enough, there will be additional re-

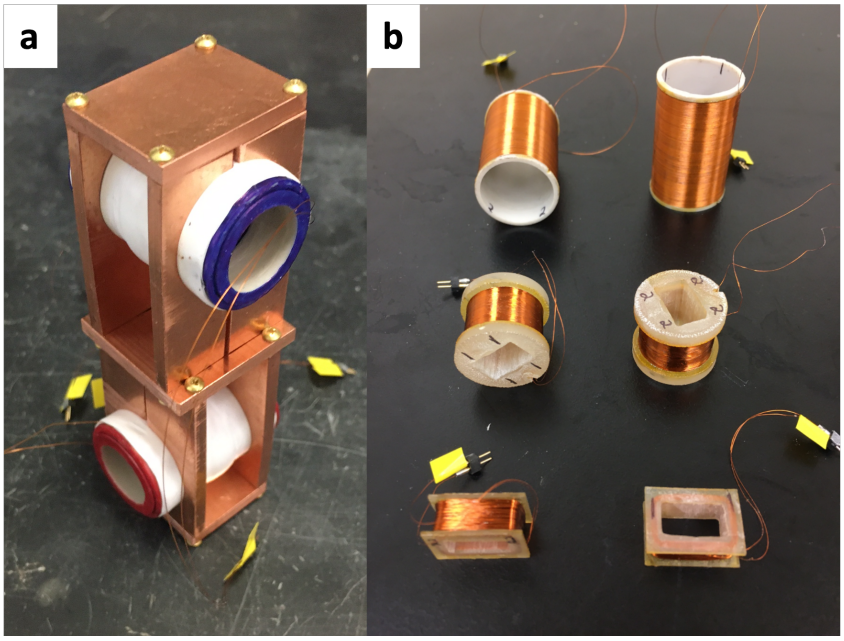

Figure 2.1: Photograph of the in-house built vector susceptometer made out of high-purity (OFHC) Copper, and coil-forms machine out of Hysol epoxy. **a** The fully-assembled susceptometer with accompanying coils. **b** In-house wrapped coils for vector susceptometry.

sponses at some frequencies $\{\omega_{\text{output}}\} \notin \{\omega_{\text{input}}\}$. In the case of these measurements, this means searching for sidebands of the pump and probe frequencies.

In the case of these measurements, in which the sample was driven with two sinewaves with almost the same frequency, a signature of the non-linear contribution $\chi^{(3)}$ can be found as sidebands in the spectral response. There will be contributions from $\chi^{(3)}$ at frequencies $\{\omega_p - \Delta\omega, \omega_p, \omega_d, \omega_d + \Delta\omega\}$. Since the linear term $\chi^{(1)}$ has terms at frequencies $\{\omega_p, \omega_d\}$, distinguishing the non-linear from the linear responses at those frequencies is difficult. However, since the linear response does not have any terms at $\{\omega_p - \Delta\omega, \omega_d + \Delta\omega\}$, any system response at those frequencies is a definitive indication of non-linear system response.

In these specific measurements, the data were collected by first mixing down the system response by ω_p with a commercial lock-in amplifier, so the non-linear signal at $\omega_p - \Delta\omega$ was mixed down to $-\Delta\omega$, which is not easily distinguishable from the signal at $+\Delta\omega$ from the drive. The spectral component at $\omega_{nl} \equiv \omega_p + 2\Delta\omega = \omega_d + \Delta\omega$, however, gets mixed down to $2\Delta\omega$, which cannot possibly come from any linear sample response, making it a convenient signal to look for non-linearities. An illustration of the spectral components is given in Figure 2.2. This corresponds to

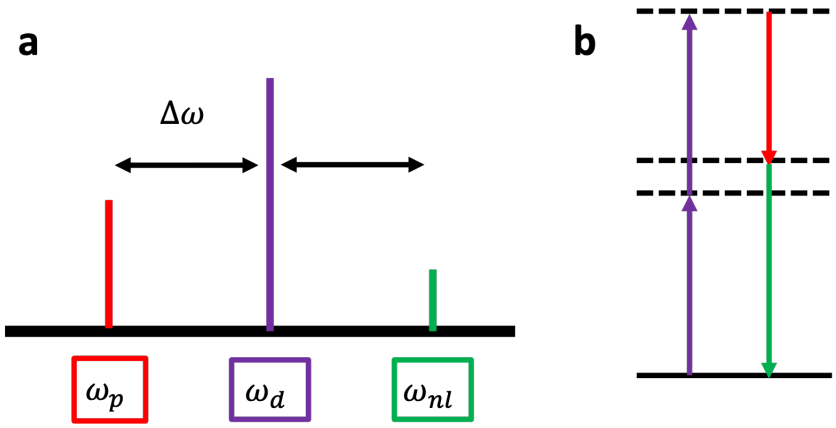

Figure 2.2: Spectral components of the system response including non-linearities. **a** Illustration of the emergence of a spectral sideband at frequency $\omega_{nl} = \omega_p + 2\Delta\omega$ due to the non-linear susceptibility $\chi^{(3)}$. **b** Illustration of level diagram showing two-photon process that generates photons at ω_{nl} by converting two photons with energy ω_d (purple) into one photon with energy ω_p (red) and another with energy ω_{nl} (green).

anti-Stokes Raman scattering–an inelastic scattering process that converts incoming photons into photons at a higher energy if $\omega_p < \omega_d$, and Stokes scattering that down-converts photons to a lower energy if $\omega_p > \omega_d$.

To pull out these non-linearities, after the down-mixed signal from the lock-in output was fed into a software fitting routine, the residuals clearly show spectral components at $2\Delta\omega$, as is shown in Figure 2.3. No phase information was recorded in these measurements, as a fully phase-coherent measurement would need to keep track of not only the phase of the probe field (represented by the local oscillator of the lock-in amplifier), but the phase of the pump field, which was not recorded.

Measuring non-linearities through frequency-mixing (in this case, Raman scattering) is a more convenient way of confirming non-linear response over the traditional method, which is to directly measure the system response as a function of the drive strength, and to extract the coefficients of the Taylor expansion of the response curve, since varying the drive strength has the unfortunate consequence of adding more heat into the system, so true temperature-independent system non-linearities must be disentangled from the effect of sample heating. By keeping the system at a constant drive power, the heating effect from the drive is de-coupled from the system response.

If non-linearities are measured, it must be confirmed that the effects are due to

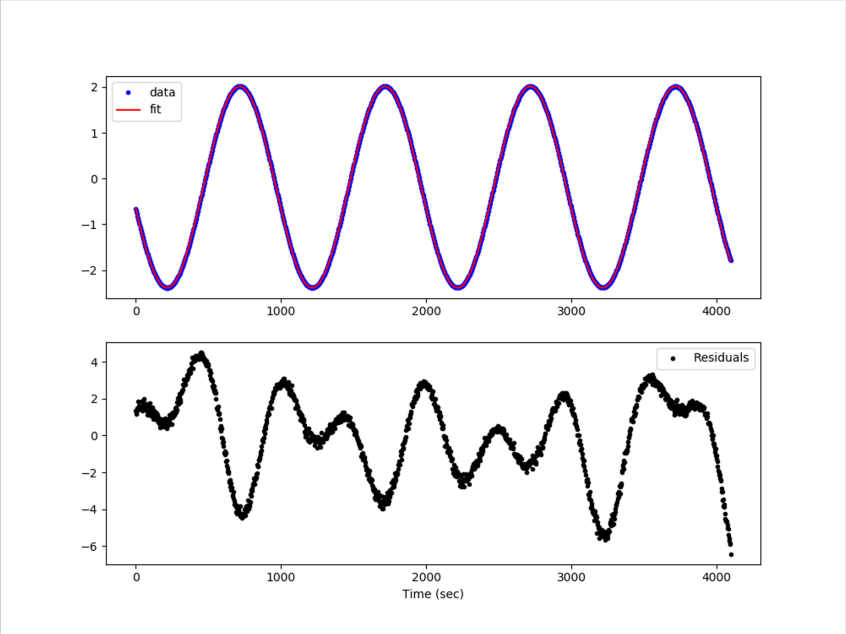

Figure 2.3: The down-mixed (by local oscillator with frequency ω_p signal is fitted in software to a sine wave with frequency $\Delta\omega$. The $\chi^{(3)}$ signal at laboratory frequency ω_{nl} is represented as a down-mixed signal at $2\Delta\omega$ left over in the residuals.

non-linearities in the sample, and not due to non-linearities in the measurement chain. Fortunately, this method of susceptometry measures the response of an empty reference coil with the same measurement chain, so signals that are present only in the sample coil and not in the reference coil are a clear indication that the measurements are due to the sample itself.

I plot in Figure 2.4 the measured sample power at frequency ω_{nl} for different values of the probe frequency $f_p = f_d + df$ as the pump frequency $f_p = \omega_p/2\pi$, pump amplitude h_{pump}, DC transverse field $H_\perp$, and temperature T are kept constant. The sample clearly responds at ω_{nl} in both the longitudinal and transverse channels, while the empty reference coil has no signal, indicating that the effect is truly due to sample non-linearities, and ruling out any amplifier non-linearities. In addition, the non-linear response behaves as one expects intuitively as a function of the detuning. While there is not enough data to quantitatively discern the exact shape of the non-linear response, there is clearly some linewidth in which the sample exhibits non-linear behavior, and, within this regime, the magnitude of the response increases as the detuning gets closer to zero.

At a fixed detuning of $\Delta f = 1$ mHz, I plot the temperature dependence of both the linear $\chi^{(1)}$ response at frequency ω_p, as well as the non-linear response $\chi^{(3)}$ at

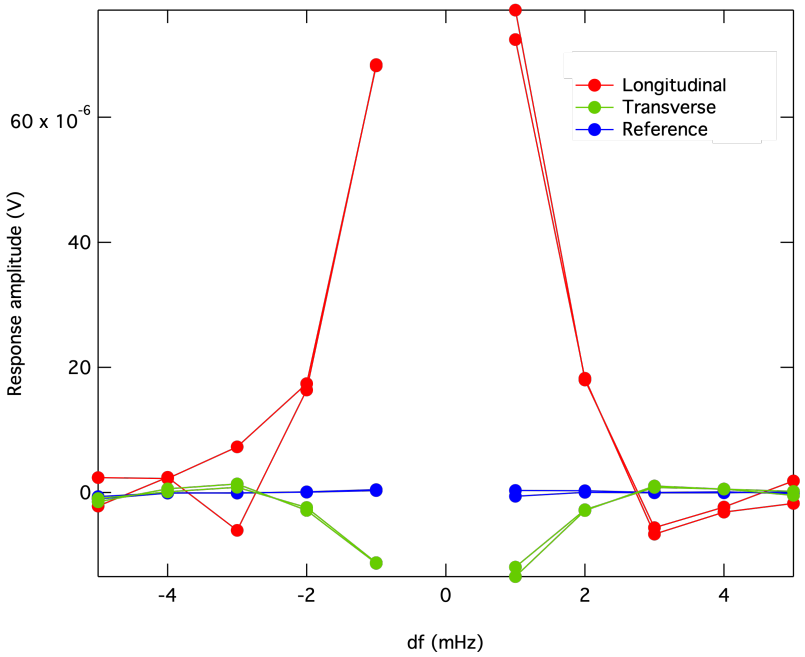

Figure 2.4: The measured sample power at the non-linear response frequency ω_{nl} for different values of the probe frequency $f_p = f_d + df$ as the pump frequency $f_p = \omega_p/2\pi$, pump amplitude h_{pump}, DC transverse field $H_\perp$, and temperature T are kept constant. The absence of any response in the empty coil indicates that the effect is truly due to sample non-linearities, ruling out any effects from the amplifier chain.

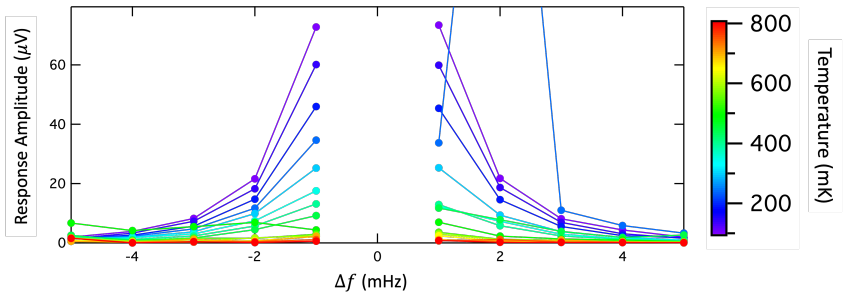

Figure 2.5: Dependence of the non-linear signal at ω_{nl} on the detuning $\Delta f = f_p - f_d$ at a series of temperatures. While all have similar linewidths at which there is appreciable non-linear response, their amplitude decreases as the temperature increases.

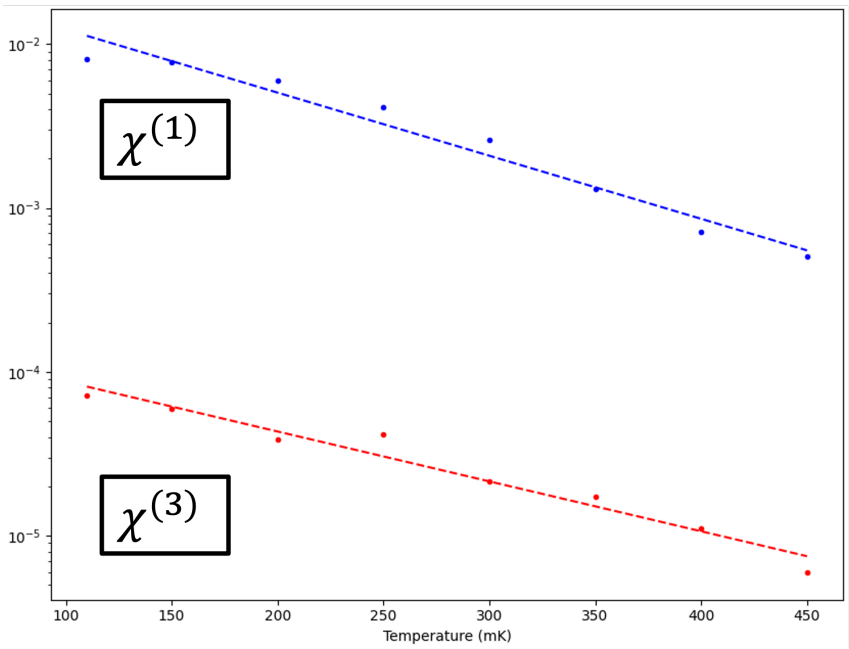

Figure 2.6: Comparison of the linear ($\chi^{(1)}$) and non-linear ($\chi^{(3)}$) responses as a function of temperature for a fixed pump amplitude, frequency, and DC transverse field. Each data set is fitted to an exponential decay of the form $|\chi^{(i)}|^2 \sim e^{-T/E_B}$, where $E_B(\chi^{(1)}) = 113$ mK and $E_B(\chi^{(3)}) = 143$ mK.

frequency ω_{nl} in Figure 2.6. Both responses fit an exponential decay of the form $|\chi^{(i)}|^2 \sim e^{-T/E_B}$, where $E_B(\chi^{(1)}) = 113$ mK and $E_B(\chi^{(3)}) = 143$ mK. While the precise origin of this temperature dependence remains unknown, it is clear that thermal fluctuations are very important in suppressing the non-linear response of the sample.

Turning now to the dependence on a static magnetic field transverse to the Ising spin axis, I plot in Figure 2.7 the dependence at fixed pump amplitude, pump frequency, and temperature of the non-linear response $\chi^{(3)}(\omega_d, \omega_d, -\omega_p)$ for both the longitudinal ($\chi_\parallel$) and transverse ($\chi_\perp$) channels. Both responses follow the same functional form with different normalization constants, indicating that both responses are different spatial projections of the same underlying dynamics. While there is a general decreasing trend with increasing transverse field, there exists an exceptional point at $H_\perp = 3$ kOe where the response drops dramatically.

I discuss below a plausible microscopic origin of these non-linearities, as well as another set of measurements that reveal that the non-linear response of the sample originates from coherent excitation of spin clusters, as well as quantum interference between multiple excitation pathways of the discrete levels.

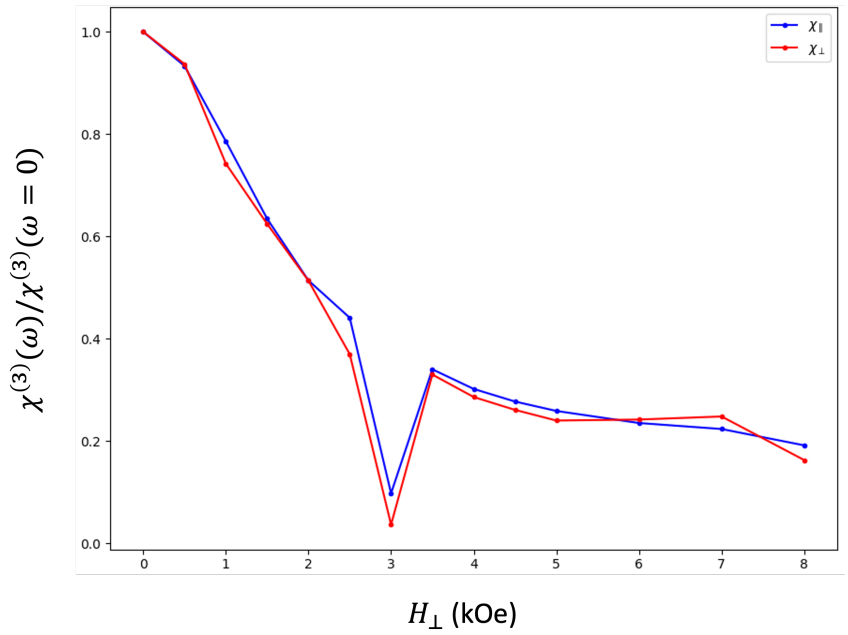

Figure 2.7: Dependence of the non-linear susceptibility $\chi^{(3)}$ on a static transverse field. Both the longitudinal response $\chi^{(3)}_{\parallel}(\omega_d, \omega_d, -\omega_p) \equiv \chi^{(3)}_{zzzz}(\omega_d, \omega_d, -\omega_p)$ and the transverse response $\chi^{(3)}_{\perp}(\omega_d, \omega_d, -\omega_p) \equiv \chi^{(3)}_{xzzz}(\omega_d, \omega_d, -\omega_p)$ follow the same functional form with different normalization constants indicating that both responses are different spatial projections of the same underlying dynamics.

2.4 Quantum Corrections to the Ising Approximation of Spin Dimers

In this section, I introduce the theory behind the spin cluster picture of $LiHo_xY_{1-x}F_4$, and more specifically how including quantum corrections to the Ising approximation can make $LiHo_{0.045}Y_{0.955}F_4$ a platform for quantum optics experiments with effective photon frequencies in the audio band ($\sim$ 100 Hz).

A key signature of the antiglass behavior is "spectral hole burning", i.e., the observation of a Fano resonance in the magnetic susceptibility $\chi(\omega)$ in a $LiHo_xY_{1-x}F_4$ sample, which is strongly driven by a time-dependent magnetic field [35, 70]. Fano resonances are commonly a signature of quantum interference. In $LiHo_xY_{1-x}F_4$, the resonances are observable at surprisingly small drive frequencies $\omega_d \approx 2\pi \times 200$ Hz and probe frequency detuninngs $\omega_p - \omega_d \approx 2\pi \times 1$ mHz. Furthermore, they can be tuned through the application of a transverse magnetic field. They occur if the $LiHo_xY_{1-x}F_4$ sample is well isolated from its environment and vanish if the coupling to the environment is increased.

The magnetic moments in $LiHo_xY_{1-x}F_4$ form a complicated, disordered, and strongly

interacting many-body problem, which is hard to address theoretically even in the simplified Ising approximation [3, 11]. What is especially puzzling in the hole burning experiments [70] is the presence of several, strongly separated energy scales and the apparent sensitivity of hole burning to all of them. The dipole-dipole interaction between two neighboring moments is of order $\Delta V \sim 500$ mK and falls off with a distance as $\sim 1/r^3$. The $LiHo_xY_{1-x}F_4$ sample is held at a temperature of $T \sim 100mK$. The sample is driven by an oscillating magnetic field with Rabi frequency $\Omega_d \approx 2\mu$K, a drive frequency which corresponds to $\omega_d \approx 60$ nK, and its response is probed at a detuning $\omega_p - \omega_d \approx 0.6$ pK.

In this work, I start from a microscopic description of $LiHo_xY_{1-x}F_4$, incorporating the full magnetic dipole-dipole interaction and the crystal field for the $J = 8$ angular momentum state of each Ho^{3+} ion. Using exact diagonalization, I will show that the observation of Fano resonances can be explained on a qualitative level already for a single pair of Ho^{3+} ions. The resonances appear as a consequence of interference between two quasi-degenerate excitation pathways, corresponding to a pair of quasi-degenerate quantum states, which can be coupled by applying an external, oscillating magnetic field.

In order to generalize this observation to more realistic samples with $n \geq 10$ magnetic degrees of freedom, I derive a toy model of effective spin-$\frac{1}{2}$ degrees of freedom, which captures the main ingredients for the observation of hole burning and reduces to the $LiHo_xY_{1-x}F_4$ Hamiltonian at low energies and for few magnetic moments. Exploring the dynamics of small samples shows that an external, oscillating magnetic field addresses only a small fraction of the many-body Hilbert space for a given set of driving parameters. The predicted magnetic susceptibility $\chi(\omega)$ displays several spectral holes, which can be explained in terms of quasi-degenerate many-body excitation pathways, and which match qualitatively well with the experimental findings and energy scales. Within this simplified model, one can understand the origin and the importance of the different energy scales and, in addition, can explain why the Fano resonance is only observed in the limit of very small coupling between the sample and the environment.

In the Ising approximation, each magnetic moment reduces to an Ising spin $J_i^\alpha = \delta_{\alpha,z} C_{zz} \sigma_i^z$ [10, 63, 76], whose orientation is described by the Pauli matrix σ^z. Under this transformation, the full electronic Hamiltonian reduces to $\mathcal{H} \rightarrow \mathcal{H}_{\text{Ising}}$ with

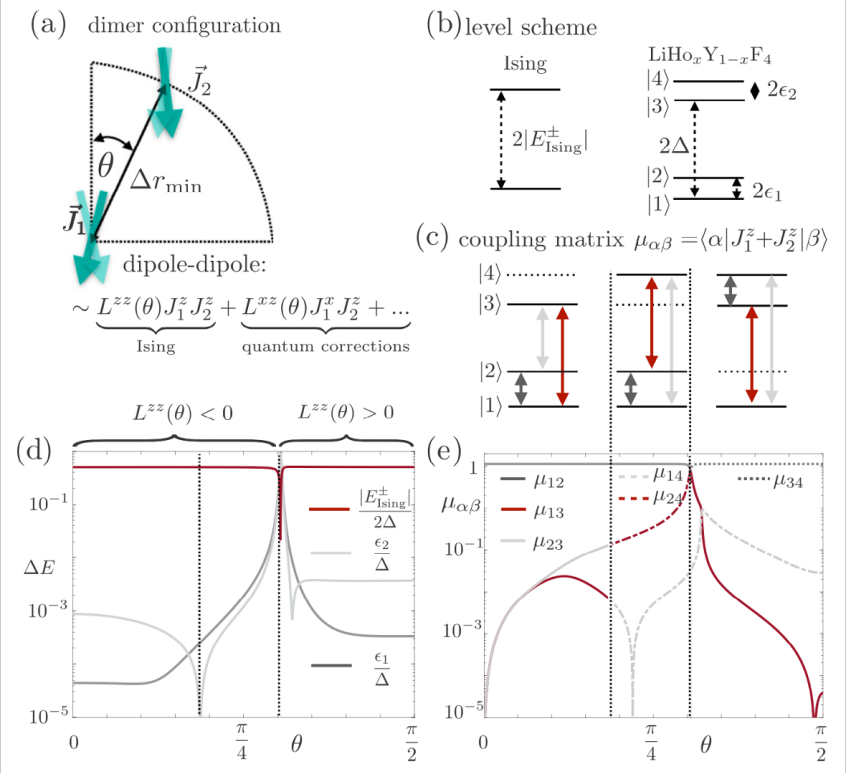

Figure 2.8: A magnetic dimer is the simplest unit from which hole burning in $\text{LiHo}_x\text{Y}_{1-x}\text{F}_4$ can be understood. (a) It is formed by two $J = 8$ magnetic moments, which interact with the material's crystal field and experience a mutual dipole-dipole force. The crystal field forces each magnetic moment to align along the z axis and features an Ising-type ground state manifold associated with spin up and down. This singles out the Ising contribution $\sim J_1^zJ_2^z$ as the dominant dipole-dipole interaction at low temperatures. Quantum corrections, led by the terms $\sim J_1^xJ_2^z, J_1^zJ_2^x$ are strongly suppressed by the crystal field but crucial for the understanding of hole burning in driven $\text{LiHo}_x\text{Y}_{1-x}\text{F}_4$ samples. (b) The terms $J_1^xJ_2^z$, ... are not compatible with the Ising symmetry. They lift the Ising degeneracy and introduce small level splittings $\epsilon_{1,2}$ between two quasi-degenerate eigenstates in the $\text{LiHo}_x\text{Y}_{1-x}\text{F}_4$ dimer. (c) Breaking the Ising symmetry also introduces small but nonzero transition matrix elements $\mu_{\alpha\beta} = \left\langle\alpha\right|(J_1^z + J_2^z)\left|\beta\right\rangle$ between different dimer eigenstates $|\alpha\rangle$, $|\beta\rangle$. (d), (e) Quantitative analysis of the level spacings (d) and transition matrix elements (e) from exact diagonalization of a $\text{LiHo}_x\text{Y}_{1-x}\text{F}_4$ dimer described by $\mathcal{H}^{(2)}$ in Eq. (2.10) with relative orientation $\vec{r}_{12} = \Delta r_{\min}(\sin\theta, 0, \cos\theta)$ [with $L^{\alpha\beta}(\theta) \equiv L^{\alpha\beta}(\theta)(\vec{r}_{12})$]. The energies are compared to an equivalent Ising dimer, described by Eq. (2.11). The colors in (e) match with the illustration in (c). At $\theta = \arccos\frac{1}{\sqrt{3}}, \frac{3\pi}{16}$, the states $|3\rangle$ and $|2\rangle$, $|4\rangle$ are degenerate. For some θ, there is one "dark" state (dashed line) corresponding to an Ising singlet, which does not couple to the other states via J^z. The quasi-degenerate partner of the dark state, however, weakly couples to both states of the remaining quasi-degenerate pair. I refer to the particular form of $\mu_{\alpha\beta}$ in (c), (e), i.e., the coupling of a quasi-degenerate pair of states to an energetically well separated state, as a "Λ scheme". It is the basic building block for hole burning in driven $\text{LiHo}_x\text{Y}_{1-x}\text{F}_4$.

$$\mathcal{H}_{\text{Ising}} = \frac{A_{\text{dip}} C_{zz}^2}{2} \sum_{i \neq j} \sigma_i^z \sigma_j^z L^{zz}(R_{ij}). \tag{2.9}$$

Here $A_{\text{dip}} = 18.5$ mK is the interaction energy, $C_{zz} \approx 5.51$ is the effective renormalized magnetic moment along the Ising axis, and R_{ij} is the dimensionless distance between spin i and spin j in units ofΔr_{min}.

The full electronic Hamiltonian in the 17-dimensional $J = 8$ Hilbert space can be well approximated by the Ising Hamiltonian (2.9) for $LiHo_{0.045}Y_{0.955}F_4$ if the dissipation rates, corresponding to dephasing and incoherent flips of the magnetic moments, are larger than the energy level splittings between quasi-degenerate states. In this case, dissipation dominates over coherent dynamics and the dynamics look effectively classical, i.e., Ising-like. This statement will be made more quantitative below by showing that the hole burning, associated to the antiglass dynamics, can be explained on the basis of the $J = 8$ Hamiltonian without performing the Ising approximation.

In order to point out the importance of quantum effects in the $LiHo_xY_{1-x}F_4$ Hamiltonian for $x \leq 0.05$, I compare the low energy physics of the full Hamiltonian $\mathcal{H}$ with the effective Hamiltonian over the truncated Hilbert space $\mathcal{H}_{\text{Ising}}$ for small spin clusters of $n = 2, 3$ magnetic moments and refer to $n = 2, 3$ as a dimer, trimer setup. Quantum corrections are caused by the off-diagonal dipole-dipole interactions $J_i^z J_j^x$ and $J_i^x J_j^x$, which induce virtual transitions out of the crystal field's ground state manifold. The large angular momentum $J = 8$ yields significant transition matrix elements for states far above the $\sim$ 10 K gap of the first excited state. Although the corrections resulting from these transitions remain perturbative, a large fraction of the excited states have to be taken into account for a correct description of the quantum corrections. In order to be free of approximations, I choose n positions for the Ho^{3+} atoms and diagonalize the $17^n \times 17^n$ Hamiltonian $\mathcal{H}$ with crystal field parameters taken from [61]. The precise form of the crystal field Hamiltonian for $LiHo_xY_{1-x}F_4$ is discussed in Chapter 1.

First, I consider a dimer setup of two Ho^{3+} ions with $J = 8$. which experience the crystal field and mutual dipole-dipole interactions. The Hamiltonian of the two ions $i = 1, 2$, which are separated by a vector $\vec{R}_{12}$ (in units of Δr_{min}), is

$$\mathcal{H}^{(2)} = \mathcal{H}_{\text{cf}}(\vec{J}_1) + \mathcal{H}_{\text{cf}}(\vec{J}_2) + A_{\text{dip}} \sum_{\alpha,\beta=x,y,z} L^{\alpha\beta}(\vec{r}_{12}) J_1^\alpha J_2^\beta \tag{2.10}$$

with $L^{\alpha\beta}(\vec{r}_{12}) = \frac{\delta_{\alpha\beta}|\vec{R}|^2 - 3r^\alpha r^\beta}{|\vec{R}|^5}$ as the dipole-dipole matrix element between ions with relative displacement $\vec{r}_{12}$. The corresponding Ising Hamiltonian is obtained by projecting onto the ground state doublets of $\mathcal{H}_{\mathrm{cf}}(\vec{J}_{1,2})$ and is given by

$$\mathcal{H}^{(2)}_{\mathrm{Ising}} = A_{\mathrm{dip}} C^2_{zz} L^{zz}(\vec{r}_{12}). \tag{2.11}$$

It has eigenenergies $\pm E_{\mathrm{Ising}} = \pm|A_{\mathrm{dip}} C^2_{zz} L^{\alpha\beta}(\vec{r}_{12})|$, each of which is twofold degenerate.

In general, the dipole-dipole interaction in Eq. (2.11) does not feature a compatible $\mathbb{Z}_2$ symmetry and thus breaks the ground state degeneracy of the crystal field Hamiltonian. This introduces splitting energies $\epsilon_{1,2}$ as illustrated in Fig 2.8b. I introduce the projector $P^{(n)}$, which projects onto the 2^n states of lowest energy of $H^{(n)}$. For each dimer eigenbasis one finds

$$P^{(2)} H^{(2)} P^{(2)} = 2\mathrm{diag}(\Delta + \epsilon_2, \Delta, \epsilon_1, 0) \tag{2.12}$$

and

$$H^{(2)}_{\mathrm{Ising}} = 2\mathrm{diag}(E_{\mathrm{Ising}}, E_{\mathrm{Ising}}, 0, 0). \tag{2.13}$$

Away from the special point $L^{zz}(\vec{R}_0) = 0$, where the 'classical Ising' interaction vanishes, the modifications of the eigenvalues of $P^{(2)} H^{(2)} P^{(2)}$ compared to $H^{(2)}_{\mathrm{Ising}}$ seem relatively small, i.e., $\frac{\epsilon_{1,2}}{\Delta}$, $\left|\frac{\Delta - E_{\mathrm{Ising}}}{E_{\mathrm{Ising}}}\right| \sim 10^{-3} - 10^{-4}$ for $|\vec{R}| = 1$, see Fig. 2.8d. For $|\vec{R}| > 1$, one finds an accurate scaling estimate:

$$\left[\frac{\epsilon_{1,2}}{\Delta}\right]_{|\vec{R}|>1} \approx \left[\frac{\epsilon_{1,2}}{\Delta}\right]_{|\vec{R}|=1} \frac{1}{|\vec{R}|^3}. \tag{2.14}$$

This anticipates that the corrections of $P^{(2)} \mathcal{H}^{(2)} P^{(2)}$ compared to $\mathcal{H}^{(2)}_{\mathrm{Ising}}$ can be understood in terms of second-order perturbation theory. The eigenvalues of the dipole matrix $J^\alpha_1 J^\beta_2$ can, however, become very large. Using second order Brillouin-Wigner perturbation theory [53] in the eigenbasis of $\mathcal{H}_{\mathrm{cf}}(\vec{J}_1) + \mathcal{H}_{\mathrm{cf}}(\vec{J}_2)$, convergence towards $P^{(2)} \mathcal{H}^{(2)} P^{(2)}$ requires the inclusion of more than $N = 100$ of the $172 = 289$ eigenstates. This makes it difficult to express the eigenstates of $P^{(2)} \mathcal{H}^{(2)} P^{(2)}$ in the Ising basis analytically.

A second modification caused by using $\mathcal{H}^{(2)}$ instead of $\mathcal{H}^{(2)}_{\text{Ising}}$ is that the total z axis magnetization $J^z_{\text{tot}} = J^z_1 + J^z_2$ is no longer diagonal in the basis of energy eigenstates. For the Ising Hamiltonian, $J^z_i \sim \sigma^z_i$ and $[\sigma^z_i, \mathcal{H}_{\text{Ising}}] = 0$ and J_{tot}, $\mathcal{H}_{\text{Ising}}$ can be diagonal in the same basis. In contrast, all diagonal matrix elements of J^z_{tot} vanish in the eigenbasis of $\mathcal{H}$. I define the matrix elements of the total magnetic moment in the z direction between eigenstates $|\alpha\rangle$, $|\beta\rangle$

$$\mu_{\alpha\beta} = \left\langle \alpha \left| J^z_{\text{tot}} \right| \beta \right\rangle = \sum_i \left\langle \alpha \left| J^z_i \right| \beta \right\rangle \tag{2.15}$$

For Ising eigenstates, $\mu_{\alpha\beta} \sim \delta_{\alpha\beta}$, while for $LiHo_xY_{1-x}F_4$ clusters $\mu_{\alpha\beta} \sim (1 - \delta_{\alpha\beta})$. The absolute values $|\mu_{\alpha\beta}|$ for the dimer setup are shown in Fig. 2.8e.

For noncommuting $[J^z_{\text{tot}}, \mathcal{H}] \neq 0$, an oscillating magnetic drive field $h(t) = h_d \cos(\omega_d t)$ in the z direction, which is described by the Hamiltonian

$$\delta\mathcal{H}(t) = h_d \cos(\omega_d t)\mu_B\mu_0 J^z_{\text{tot}}, \tag{2.16}$$

induces transitions between different energy eigenstates $|\alpha\rangle \rightarrow |\beta\rangle$. The transition rates are proportional to $|\mu_{\alpha\beta}|$ (see Fig. 2.8e), and the corresponding level schemes for the dimer setup are illustrated in Fig. 2.8c. The transition matrix $|\mu_{\alpha\beta}|$, which couples a quasi-degenerate pair of states to another energetically well separated state, has the shape of a (inverse) Λ and is referred to as a "Λ scheme." As will be discussed, it features similar dynamics to driven three-level systems in quantum optics, where Λ schemes of this shape are common. The Λ scheme is the basic building block for the understanding of hole burning in $LiHo_xY_{1-x}F_4$ and will be analyzed in detail in the following sections.

Adding more magnetic moments to the cluster either enhances or suppresses corrections to the Ising approximation and may lead to more involved coupling matrices $\mu_{\alpha\beta}$. Refer to [15] for a detailed derivation, but it can be shown that both the addition of more Ho^{3+} moments, as well as the addition of the hyperfine interaction, still result in the accumulation of relatively isolated truncated Hilbert spaces consisting of effective Λ schemes.

2.5 Magnetic Susceptibility and Fano Resonances of Strongly-Driven Spin Dimers

The Λ schemes found in magnetic dimers in Figure 2.8c are common candidates for the observation of interference between different excitation pathways and Fano resonances [34, 48]. In this section, I discuss the mechanism of destructive interference, which leads to a Fano resonance in the magnetic susceptibility, for an idealized Λ scheme. The Λ scheme itself is illustrated in Figure 2.9. It consists of three quantum states $|1, 2, 3\rangle$, which are driven by two external fields. The $|2\rangle \rightarrow |3\rangle$ transition is driven by a time-dependent driving field and the $|1\rangle \rightarrow |3\rangle$ transition is driven by a time-dependent probe field. The measured time-dependent magnetic susceptibility will be proportional to the coherences $|3\rangle\langle 2|$, $|3\rangle\langle 1|$. Their dynamics do not depend on whether the Λ scheme is regular or inverted and, without loss of generality, I discuss an inverted scheme. The generalization to the situation of many magnetic moments can be found in [15].

The ideal Λ scheme consists of three levels $|l\rangle$, $l \in \{1, 2, 3\}$ corresponding, e.g., to three different dimer eigenstates, as shown in Figure 2.9c. An oscillating external magnetic field with Rabi frequency Ω_d and drive frequency ω_d drives the $|2\rangle \rightarrow |3\rangle$ transition with a detuning $\eta = \omega_d - E_{23}$ from resonance. At the same time, an oscillating probe field with Rabi frequency Ω_p and drive frequency ω_p probes the $|1\rangle \rightarrow 3$ transition with detuning $\nu + \eta = \omega_p - E_{13}$ from resonance. In addition, incoherent transitions are induced by the coupling of the states to a phonon continuum. The corresponding rates for the (anti-) Stokes $\gamma_{3\rightarrow 1,2}$ ($\gamma_{1,2\rightarrow 3}$) are modeled and estimated in [15].

The time-dependent Hamiltonian for this Λ scheme is:

$$\mathcal{H}_\Lambda(t) = E_{13}\,|1\rangle\langle 1| + E_{23}\,|2\rangle\langle 2| + \Omega_d \cos(\omega_d t)(|2\rangle\langle 3| + \text{h.c.}) + \Omega_p \cos(\omega_p t)(|1\rangle\langle 3| + \text{h.c.}), \tag{2.17}$$

with $E_{13}, E_{23} > 0$. Assuming small Rabi frequencies, $\Omega_{d,p} \leq \omega_{d,p}$, one can perform a rotating wave approximation (RWA), i.e., transform the $\mathcal{H}_\Lambda(t)$ into a frame rotating with the drive and pump fields and discard all counterrotating terms $\sim 2\omega_{d,p}$. The corresponding unitary transformation is $U(t) = \exp[it(\omega_p\,|1\rangle\langle 1| + \omega_d\,|2\rangle\langle 2|)]$ and the transformed Hamiltonian is:

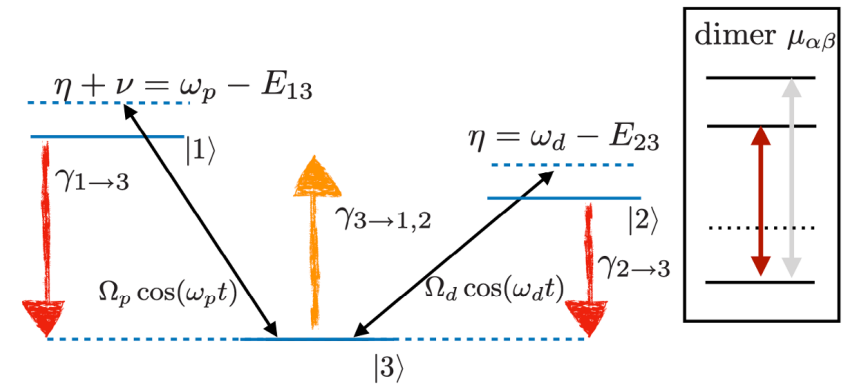

Figure 2.9: Illustration of an idealized, driven Λ scheme, which is realized in an antiferromagnetic Ho^{3+} dimer subject to time-dependent magnetic drive and probe fields in the z direction. The inset shows a corresponding dimer transition matrix $\mu_{\alpha\beta}$ extracted from Figure 2.8c. The drive, probe fields oscillate with frequencies ω_d, ω_p, and the strength of the couplings is described by the Rabi frequencies Ω_d, Ω_p, which are proportional to the corresponding coupling matrix elements and the strength of the magnetic drive, probe fields h_d, h_p, i.e., $\Omega_d \sim h_d\mu_{13}$, $\Omega_p \sim h_p\mu_{23}$. The drive scheme also includes dissipative transitions with rates $\gamma_{\alpha\to\beta}$, corresponding to Stokes ($\uparrow$) and anti-Stokes ($\downarrow$) transitions, which stem from the coupling of the magnetic moments to a low-temperature phonon continuum. Adjusting the detuning η, $\nu + \eta$ of the drive and probe field from the energy differences E_{13}, E_{23} in the Λ scheme enables a Fano resonance, i.e., hole burning, in the linear susceptibility $\chi^{(1)}$. Note: this illustration represents an idealization. In reality, both the drive and probe fields contribute to μ_{13} and μ_{23} at the same time. In linear response to the probe field h_p, however, the measured signal is very well approximated by Λ schemes linear in h_d. The fuller picture can be described by a drive scheme with $(\omega_d, h_d) \to (\omega_p, h_p)$.

$$\begin{aligned}\tilde{\mathcal{H}}_\Lambda &= U^\dagger(t)\mathcal{H}_\Lambda(t)U(t) - iU^\dagger(t)\partial_t U(t)^{\text{RWA}} \\ &= \frac{\Omega_d}{2}(|3\rangle\langle 2| + |2\rangle\langle 3|) + \frac{\Omega_p}{2}(|3\rangle\langle 1| + |1\rangle\langle 3|) \\ &\quad + \nu\,|2\rangle\langle 2| + (\nu+\eta)\,|3\rangle\langle 3|\,.\end{aligned} \tag{2.18}$$

In the last step, a constant energy shift was added $\tilde{\mathcal{H}}_\Lambda \to \tilde{\mathcal{H}}_\Lambda + (\nu + \eta)$, which does not change the dynamics.

In order to account for the dissipation, I use a density matrix description of the magnetic system. The density matrix

$$\hat{\rho} = \sum_{\alpha,\beta\in\{1,2,3\}} \rho_{\alpha\beta} \left|\alpha\right\rangle \left\langle\beta\right| \tag{2.19}$$

is Hermitian $\rho_{\alpha\beta} = \rho^*_{\alpha\beta}$ and has unit trace $\sum_\alpha \rho_{\alpha\alpha} = 1$. Its time evolution is described by a quantum master equation in Lindblad form [13]:

$$\partial_t \hat{\rho} = i[\hat{\rho}, \tilde{\mathcal{H}}_\Lambda] + \sum_{\alpha=1,2} (\mathcal{L}_{\alpha\to 3} + \mathcal{L}_{3\to\alpha})\hat{\rho}. \tag{2.20}$$

The second term describes dissipative transitions via the superoperators $\mathcal{L}_{\alpha\beta}$ which act linearly on $\hat{\rho}$,

$$\mathcal{L}_{\alpha\to\beta}\hat{\rho} = \gamma_{\alpha\to\beta}(\left|\beta\right\rangle \left\langle\alpha\right| \hat{\rho} \left|\alpha\right\rangle \left\langle\beta\right| - \frac{1}{2}\{\left|\alpha\right\rangle \left\langle\alpha\right|, \hat{\rho}\}). \tag{2.21}$$

The linear response to the probe field $\sim \Omega_p$ is obtained from the stationary state ($\partial_t\hat{\rho} = 0$) of Eq. (2.21). To simplify notation, I assume one common rate $\gamma \equiv \gamma_{\alpha\to\beta}$ for all dissipative processes. This is justified for $k_B T > E_{13}, E_{23}$. One finds

$$\rho_{11} \approx \rho_{22} = \frac{1-\rho_{33}}{2} \tag{2.22}$$

$$\rho_{21} = \frac{\Omega_d\rho_{31} - \Omega_p\rho_{23}}{2(i\gamma - \nu)} \tag{2.23}$$

$$\rho_{23} = \frac{\Omega_d(3\rho_{33}-1)}{4\eta + 6i\gamma} \tag{2.24}$$

$$\rho_{31} = \frac{i\gamma - \nu + \frac{\Omega_d^2}{4\eta+6i\gamma}}{\Omega_d^2 - (i\gamma-\nu)(6i\gamma - 4(\eta+\nu))}\Omega_p(3\rho_{22}-1). \tag{2.25}$$

The time-dependent expectation of an arbitrary, time independent operator $\hat{O}$ in the rotating frame is

$$\left\langle\hat{O}\right\rangle(t) = \mathrm{Tr}(U^\dagger(t)\hat{\rho}U(t)\hat{O}) = \sum_{\alpha,\beta}(U^\dagger(t)\hat{\rho}U(t))_{\alpha,\beta}O_{\beta\alpha}. \tag{2.26}$$

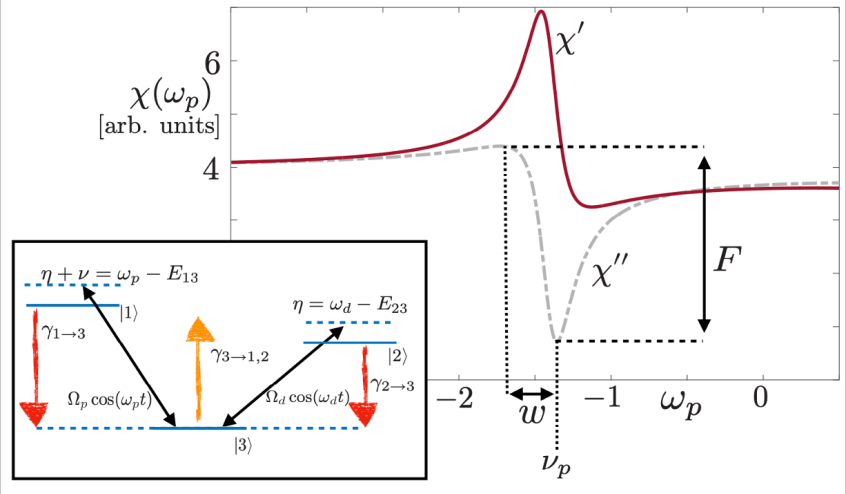

Figure 2.10: Spectral hole (Fano resonance) in the susceptibility $\chi(\omega_p)$ obtained in linear response in Ω_p from the Λ scheme in Figure 2.9 (repeated in inset). Both the real (χ', red bold line) and the imaginary part (χ'', grey dotted line) display an asymmetric lineshape, indicating a Fano resonance close to the resonance condition $\omega_p - \omega_d \approx E_{13} - E_{23}$. The dimensionless parameters for this figure are $\gamma = 0.1$, $\Omega_d = 4$, $\omega_d = 18$, $E_{23} = 20.4$, $E_{13} = 19.4$. The dependence of the strength F, spectral width w, and position ν_p of the signal on the drive parameters can be found in [15].

If the response is evaluated at the probe frequency ω_p, only terms proportional to $\rho_{13}, \rho 31 \sim e^{\pm i\omega_p t}$ contribute to Eq. (2.26). This yields the linear response of the generic operator $\hat{O}$

$$\lim_{\omega_p\to 0}\frac{\partial\left\langle\hat{O}\right\rangle_{\omega_p}}{\partial\Omega_p} = \frac{O_{13}(i\gamma - \nu + \frac{\Omega_d^2}{4\eta+6i\gamma})}{\Omega_d^2 - (i\gamma-\nu)(6i\gamma - 4(\eta+\nu))}(3\rho_{22}-1). \tag{2.27}$$

For the specific choice of $\hat{O} = |1\rangle\langle 3| + |3\rangle\langle 1|$, i.e., measuring the operator to which the probe field is coupled, $\frac{\partial\langle\hat{O}\rangle_{\omega_p}}{\partial\Omega_p} \equiv \chi_O(\omega_p)$ is the susceptibility.

The real and imaginary parts of the susceptibility $\chi = \chi' + i\chi''$ are shown in Figure 2.10 for a suitable set of parameters. They display a pronounced Fano resonance, i.e., a spectral hole, whose strength depends on the dissipation rate γ and the Rabi frequency of the drive Ω_d. For weak driving $\Omega_d \to 0$, the signal reduces to the expected Lorentzian, $\chi''(\omega_p) = \frac{6\gamma}{36\gamma^2+16(\omega_p-E_{13}^2)}$, with a peak $\sim \frac{1}{6\gamma}$ at $\omega_p = E_{13}$.

2.6 Fano Resonances in Pump-Probe Spectroscopy of $LiHo_{0.045}Y_{0.955}F_4$

The first thing to consider is the dependence of the Fano resonances on thermal fluctuations. I plot in Figure 2.11 the imaginary part of the susceptibility at frequency $f_{\text{probe}} = f_{\text{pump}} + \Delta f$ at identical test conditions (temperature, external DC field, time-dependent pump field) except for the thermal boundary conditions. In the strong heat-sinking regime, the sample was pressed firmly against a sapphire plate that was strongly thermally coupled to the cold-finger of the Helium dilution refrigerator. In the weak regime, the sapphire was pulled out of contact with the sample, and the bulk of the cooling came from physical contact with a Hysol epoxy coil form. As can clearly be seen in Figure 2.11, the Fano resonance is only observable in the weak heat-sinking regime where isolation from the thermal bath protects quantum interference pathways.

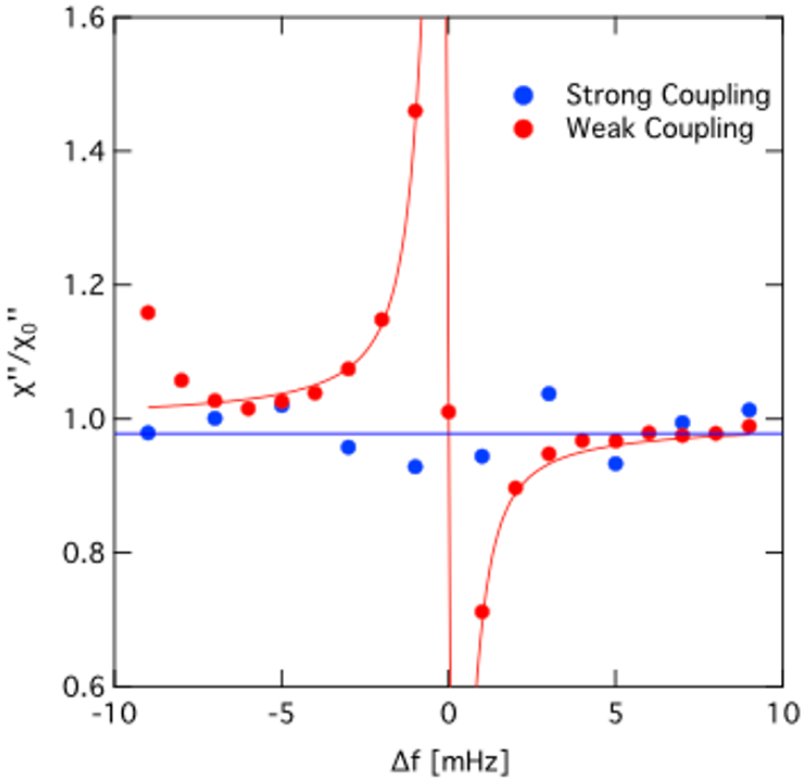

Figure 2.11: Plot of the imaginary susceptibility χ'' as a function of the detuning of the probe away from the pump $\Delta f = f_{\text{probe}} - f_{\text{pump}}$ for two heat sinking regimes. Note that the weak coupling regime clearly exhibits an asymmetric Fano resonance while the strong coupling regime does not.

By comparing the integrated area of the resonant response with the area of the entire

linear response spectrum, I estimate that the fraction of spins bound in clusters resonant at the chosen drive frequency is of order 2×10^{-6} of the entire sample. As the temperature is increased, the amplitude of the resonant response drops and the resonance appears to broaden, with the response suppressed to 8% of its original amplitude at $T = 500$ mK and to below the noise floor of the measurement at 700 mK. Given that the overall linear susceptibility of $LiHo_{0.045}Y_{0.955}F_4$ has a strong temperature dependence, the thermal evolution of the resonant response can be seen more clearly by normalizing it to the linear response at each temperature (determined by measuring $\chi''(\Delta f = 30\text{mHz})$). I show in Fig. 2.12b spectra obtained at a series of temperatures, normalized, and then combined into a surface plot where color and height now represent the absorption for a given Δf and T. The broadening of the resonance with increasing temperature emerges clearly in this visualization and I examine it quantitatively in Fig. 2.14c by looking at the evolution of the linewidth in the fits to the Fano form:

$$\chi''(\Delta f) = A\frac{(\frac{q\Gamma}{2} + \Delta f)^2}{\Delta f^2 + \frac{\Gamma^2}{2}}, \tag{2.28}$$

where Γ is the linewidth of the resonance and q, known as the Fano parameter, characterizes the interference between the different transition pathways. The mHz scale low-temperature limit of the linewidth suggests that the coupling between the clusters and the background spin bath is weak, and hence that the system can be considered in the framework of a two-level system in weak contact with the environment rather than a continuous relaxation process. Quantum states with splittings substantially smaller than nominal bath temperatures are very common in solids and liquids, and indeed form the basis for various resonance (e.g., nuclear magnetic resonance (NMR)) spectroscopies, many of which rely on non-equilibrium quantum-state preparation. Reduced bath coupling during cool-down increases the T_1 and T_2 times associated with such quantum states, and hence makes a description of the magnetic response of the system due to a set of independent multilevel quantum systems more appropriate than a picture based on classical, thermal diffusion.

When a multilevel quantum description applies for a fixed bath coupling (which extracts heat) and ac driving field (which inserts heat), an equilibrium with a set of fixed state occupancies will characterize the system, and to first order that equilibrium can be described by a fixed effective temperature. On the other hand, the non-equilibrium dynamics are dominated by small multilevel systems describ-

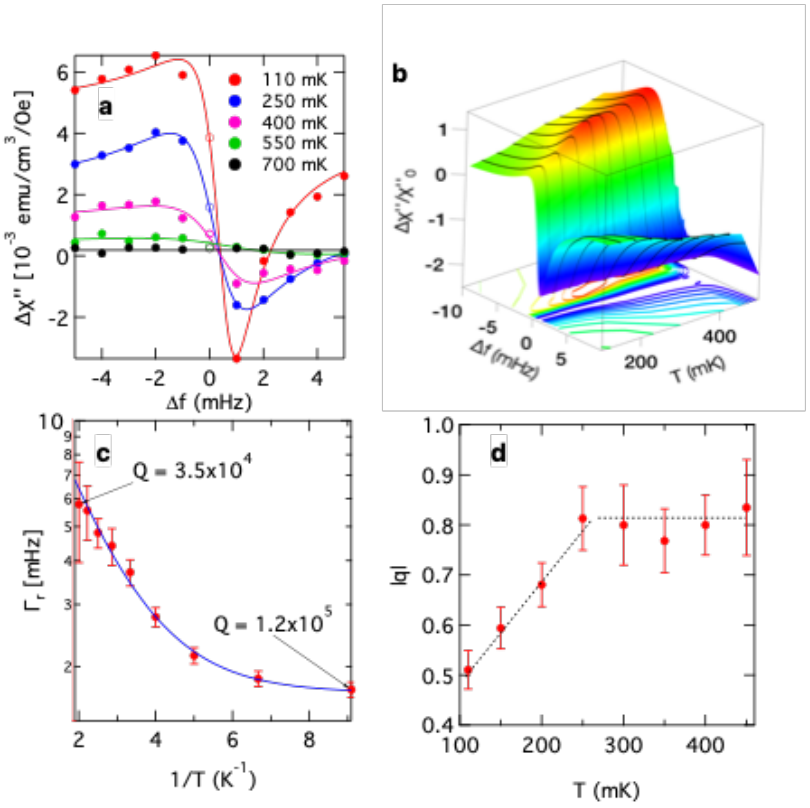

Figure 2.12: Linear absorption spectra of $LiHo_xY_{1-x}F_4$ as a function of temperature. **a** Measured absorption in the presence of a 0.3 Oe pump field at $f_{pump} = 202$ Hz and zero transverse field using a probe field with 20 mOe amplitude. Curves are fits to Fano resonance forms, Eq. 2.28 in the text. The points at $f = f_{pump}$ (open symbols) are omitted from the fits (see text for details). **b** Absorption normalized with respect to the response at $\Delta f = 30$ mHz as a function of frequency and temperature. Color and z position both indicate normalized absorption. **c** Linewidth of the resonance, as determined from fitting to the Fano model, vs. temperature T. Line is a fit to an intrinsic linewidth of 1.7 mHz plus exponential thermal broadening with $\Delta = 740$ mK . **d** Fano parameter q vs. temperature, showing the suppression of coupling to the bath at the lowest T. Lines are guides to the eye.

able in terms of some generalized Bloch equation, exactly as is the case, e.g., for NMR performed even at room temperature, and are therefore quantum mechanical. The linewidth increases exponentially with T, consistent with a thermally activated process with a gap $\Delta = 740$ mK, which is an energy well below the 9.4 K first excited crystal-field state energy but of the same order as the nearest-neighbor spin couplings.

It should be noted that the free-induction relaxation time of $\sim 10 - 30$ s observed previously [35] is substantially shorter than the $\sim 500 - 1000$ s of the inverse linewidth of the hole uncovered in the driven pump-probe measurements. This follows because the free-induction decay was measured for relaxation after the strong ac drive field was turned off, whereas the linewidth here is measured in the far more weakly driven linear regime.

I now examine the effects of various tuning parameters on the cluster response, specifically the pump amplitude $H_{\rm pump}$ and the static transverse field $H_{\perp}$., showing the measured susceptibility spectra in Figures 2.13 and 2.14, and derived quantities in Figures 2.15 and 2.16. First I explore in figures 2.13 and 2.15 the effects of changing the amplitude of the pump field. Most important is the change in the sign of the Fano q: for the largest drive field (0.5 Oe), the low- and high-frequency responses are enhanced and suppressed, respectively, opposite to what is seen for the lower drive field. The zero crossing of q occurs at a critical $h_{\rm pump} = 0.45$ Oe (Fig. 2.15a). The data point at the pump frequency where pump and probe-derived signals cannot be distinguished are ignored for the Fano fits, because they represent the response of the highly excited (pumped) clusters and not the perturbatively mixed clusters with other resonant frequencies.

Figures 2.15b,c reveal clear distinctions between $\chi_{\rm drive}$, the total signal at $f_{\rm pump}$, and $\chi_{\rm Fano}$, the linear Fano contribution calculated from evaluation at $f = f_{\rm pump}$ of the fitted Fano form to data at $f \neq f_{\rm pump}$. First, $\chi'_{\rm drive}$ goes through a maximum at the zero crossing of q (Fig. 2.15c), whereas $\chi'_{\rm Fano}$ undergoes a decrease that looks like a rounded step. Second, when I plot the phases $\phi = \tan^{-1} \chi''/\chi'$ (Fig. 2.15b), one finds that although both $\chi_{\rm drive}$ and $\chi_{\rm Fano}$ have phase shifts that are smaller at high $h_{\rm pump}$, the latter actually has a zero near the zero of q. In other words, for small linear perturbations, the Fano response is dissipationless in the limit $f \to f_{\rm pump}$. This result follows from Eq. (2.28), which gives $\phi = \phi(q) = \tan^{-1} \frac{q^2}{1-q^2}$, a functional form that is superposed over the experimental results in Fig. 2.15b. The absence of dissipation in the Fano response that describes the linear continuum at $q = 0$ means

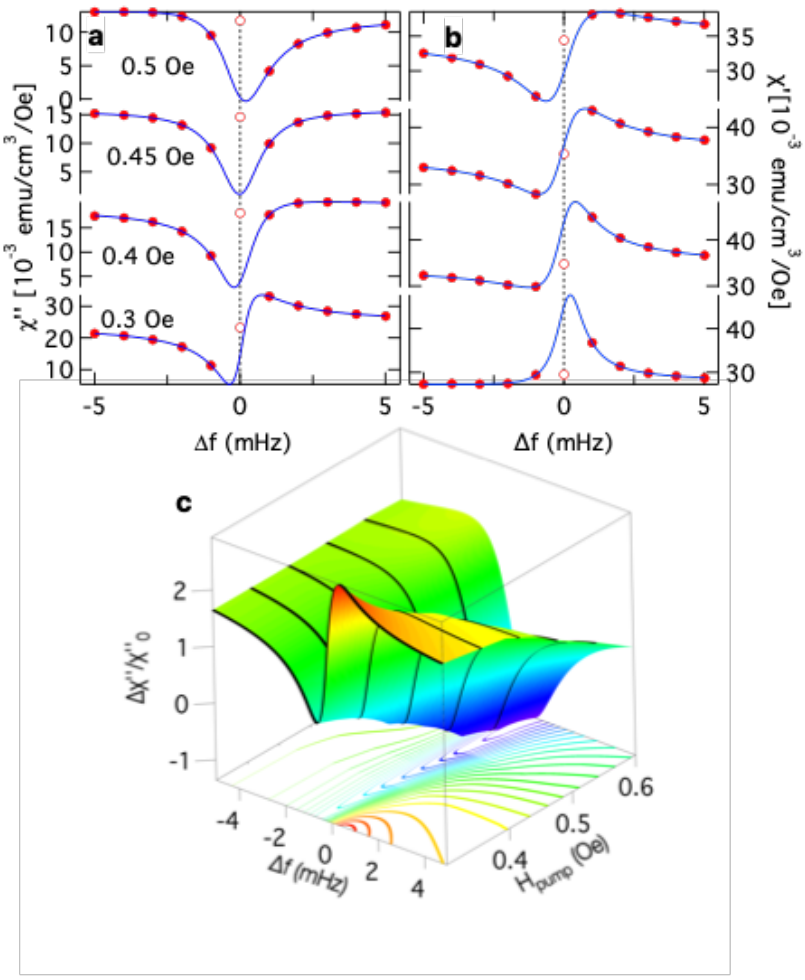

Figure 2.13: Linear absorption as a function of pump amplitude at $T = 110$ mK for a 202 Hz pump. **a**,**b** Measured imaginary and real susceptibilities (points), and fits to a Fano resonance form as a function of pump amplitude at zero transverse field. Increasing the pump amplitude tunes the resonant behavior, at the cost of increased decoherence. **c** Normalized absorption as a function of frequency and pump amplitude. Color and z position both indicate normalized absorption.

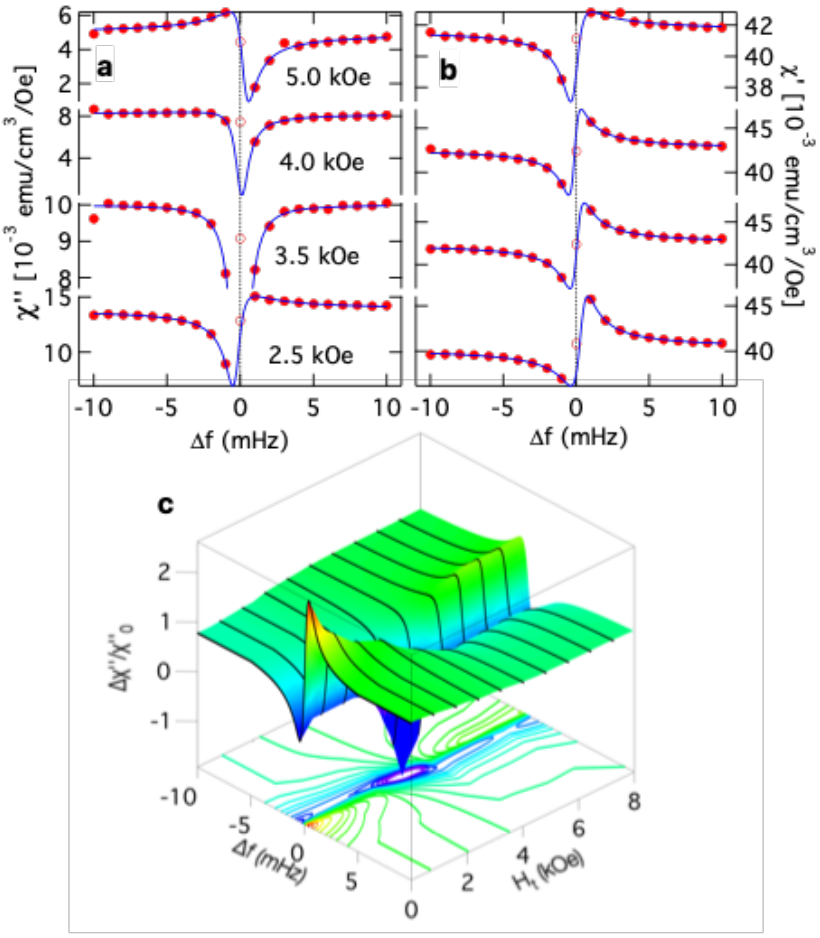

Figure 2.14: Linear absorption as a function of transverse field at $T = 110$ mK for a 202 Hz pump. **a**,**b** Measured imaginary and real susceptibilities (points) and fits to a Fano resonance as a function of transverse field for a fixed 0.3 Oe pump. Transverse field-induced quantum tunneling tunes the resonant behavior without a corresponding increase in decoherence. **c** Normalized absorption as a function of frequency and transverse field. Color and z position both indicate normalized absorption.

that hole burning is actually complete at the drive frequency: there is no continuum contribution to χ'', which remains unaffected by the drive in the limit $f \rightarrow f_{\rm pump}$. Significantly, the absence of dissipation coincident with the $q = 0$ crossing indicates that the clusters cannot be excited between their ground and excited states by the external drive.

Varying the ac pump amplitude accesses different mixtures of the states of the localized clusters. The additional power applied to the drive solenoid also results in eddy-current-induced heating of the copper susceptometer mount and hence some degree of conductive heating of the sample despite the low thermal conductivity Hysol epoxy coil form holding the sample inside the susceptometer. This, as well as dissipation within the sample itself, gives rise to a higher effective temperature, with a concomitant loss of coherence. The decoherence of the resonant excitation is reflected by a measurable increase in the linewidth Γ, whose temperature-dependent evolution can be traced readily in Fig. 2.12c. Over the range of pump amplitudes shown in Fig. 2.13, the resonance linewidth increases from 1.1 to 1.8 mHz (Fig. 2.15d, equivalent to $\sim$ 50 mK of direct thermal heating. Even while heating is clearly present, the linewidths remain negligible on the scale of the drive frequency, allowing the coherent superpositions of multiple excitation pathways. Their relative signs change at a critical longitudinal pump field of 0.45 Oe, thus yielding the zero crossing of q, one of the main results of this experiment.

I now take advantage of one of the key features of the $LiHo_xY_{1-x}F_4$ family–the ability to tune the microscopic Hamiltonian by applying a magnetic field transverse to the Ising axis, thereby quantum-mechanically mixing the single ion and cluster eigenstates [17, 83] via different matrix elements than does the ac longitudinal field. Again, application of a transverse field induces a crossover (Fig. 2.14) at a well-defined field of $H_\perp = 3.5$ kOe [68], similar to that seen earlier as a function of pump amplitude (Fig. 2.13). I also plot in Fig. 2.16a the transverse field dependence of the Fano parameter q. This parameter changes linearly with $H_\perp$ over most of the experimental range, showing that the external transverse field not only changes the energies of different states but also tunes the interference between the multiple excitation pathways. In particular, at the $H_\perp = 3.5$ kOe crossover field, q vanishes. At the same time, as also seen when $h_{\rm pump}$ was varied to obtain a zero crossing of q, there is a quadratic zero in the phase for $\chi_{\rm Fano}(f_{\rm pump})$ (Fig. 2.16b) and a maximum in $\chi'_{\rm drive}$ (Fig. 2.16c), both of which coincide with the zero of q and can be roughly described by the function $\phi(q)$. The simultaneous vanishing of q and

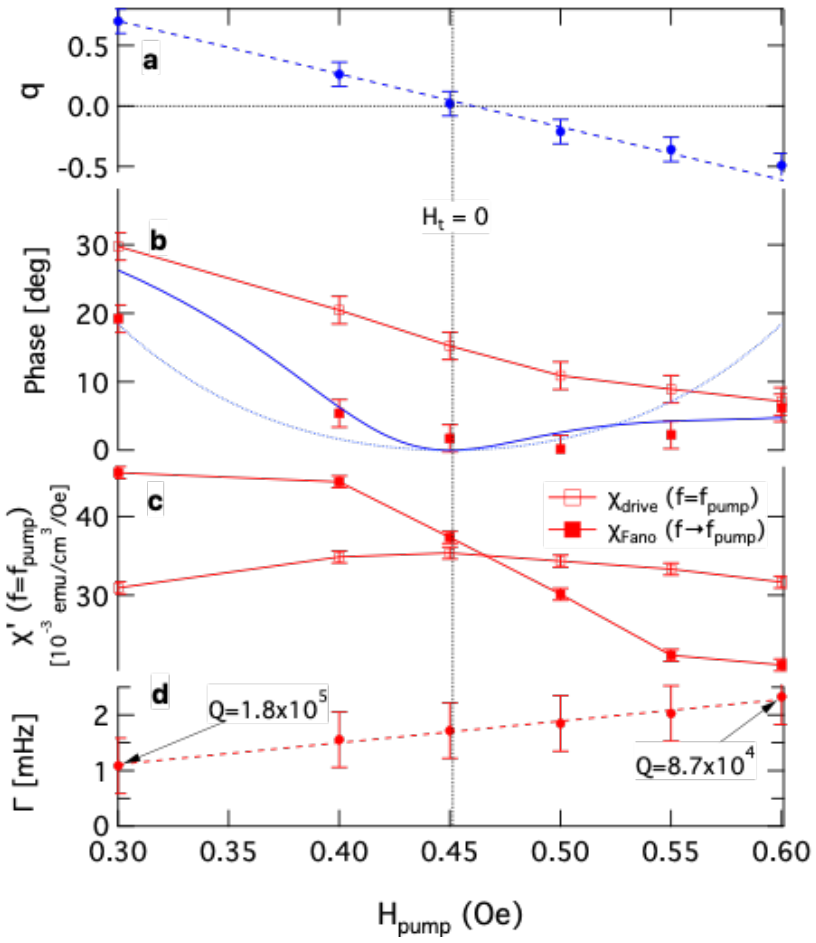

Figure 2.15: Evolution of resonant behavior as a function of pump amplitude at $T = 0.11$ K and $H_\perp = 0$ for a 202 Hz pump. **a** Fano parameter q vs. drive amplitude showing a continuous evolution including a smooth crossing through zero. Dashed line is a guide to the eye. **b** Evolution of the phase of the complex susceptibility at $f = f_{\text{pump}}$ for the non-linear (open symbols) and linear (filled symbols) responses. The zero crossings of q are associated with a local minimum in the dissipation, and a corresponding minimum in the phase shift of the linear probe response as the probe frequency approaches the pump frequency. $\phi(q) = \tan^{-1}\left(\frac{q^2}{1-q^2}\right)$ (blue dotted curve) follows from Eq. (2.28) in the text. **c** Real susceptibility χ' measured directly at $f = f_{\text{pump}}$ (open symbols) and determined by extrapolating the fitted Fano resonance to $f = f_{\text{pump}}$ (filled symbols), showing the contrast in behavior between the non-linear and linear responses, respectively. **d** Fano linewidth Γ vs. ac drive h_{pump}. Increasing the drive amplitude broadens the linewidth as heat is pumped into the system and hence reduces the oscillator Q.

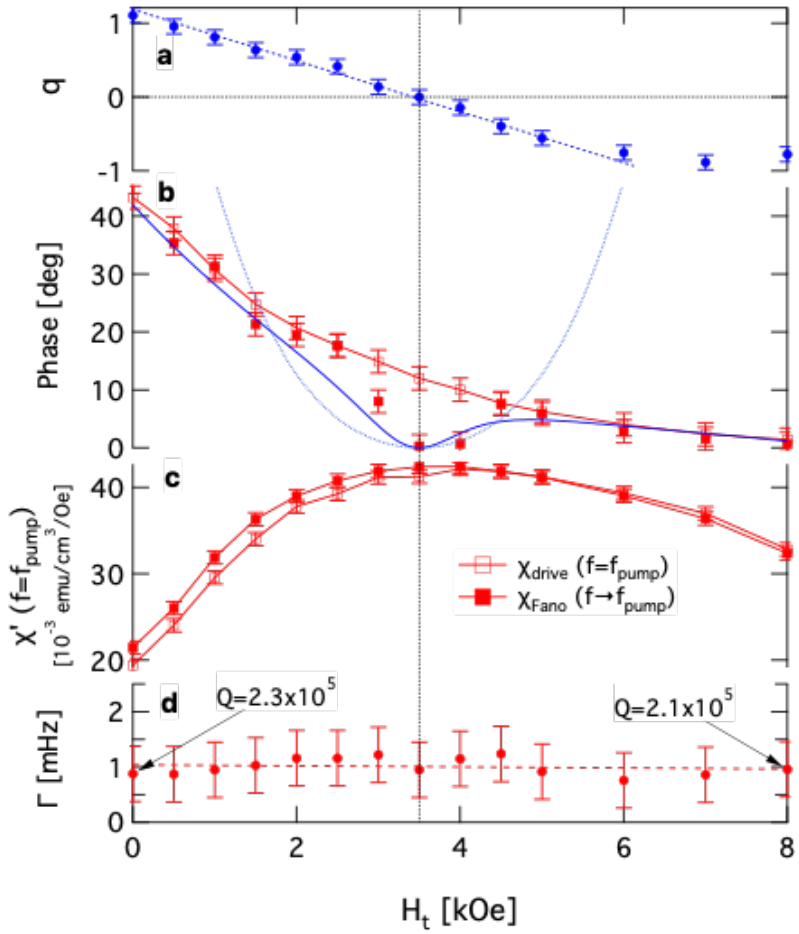

Figure 2.16: Evolution of resonant behavior as a function of transverse field at T = 0.11 K for a 202 Hz/0.3 Oe pump. **a** Fano parameter q vs. transverse field showing a continuous evolution including a smooth crossing through zero. Dashed line is a guide to the eye. **b** Evolution of the phase of the complex susceptibility at $f = f_{\text{pump}}$ for the non-linear (open symbols) and linear (filled symbols) responses. As with the pump dependence shown in Fig. 5, the zero-crossing of q is associated with a vanishing of the dissipation in the linear response with the same functional form, demonstrating universal behavior from two disparate tuning parameters. **c** Real susceptibility χ' measured directly at $f = f_{\text{pump}}$ (open symbols) and determined by extrapolating the fitted Fano resonance to $f = f_{\text{pump}}$ (filled symbols), showing a small but apparent distinction in the evolution of the non-linear and linear responses. **d** Fano linewidth Γ vs. transverse field. In contrast to the behavior as a function of h_{pump}, increasing $H_\perp$ does not change the linewidth.

the phase (and hence the dissipation) opens the possibility for the static transverse field to be used to decouple the localized cluster excitations from the external ac field. In contrast to what was seen for the h_{pump} scan with $H_\perp = 0$, χ'_{drive} and χ'_{Fano} are nearly indistinguishable at f_{pump}. Another contrast, anticipated from the previous paragraph and visible in the comparison of Figs. 2.15d and 2.16d is that the linewidth is, to within error, $H_\perp$ independent. The essentially constant behavior of the linewidth is a strong indication that the evolution due to the transverse-field-induced quantum fluctuations is fundamentally different from the purely classical behavior seen as a function of increasing temperature.

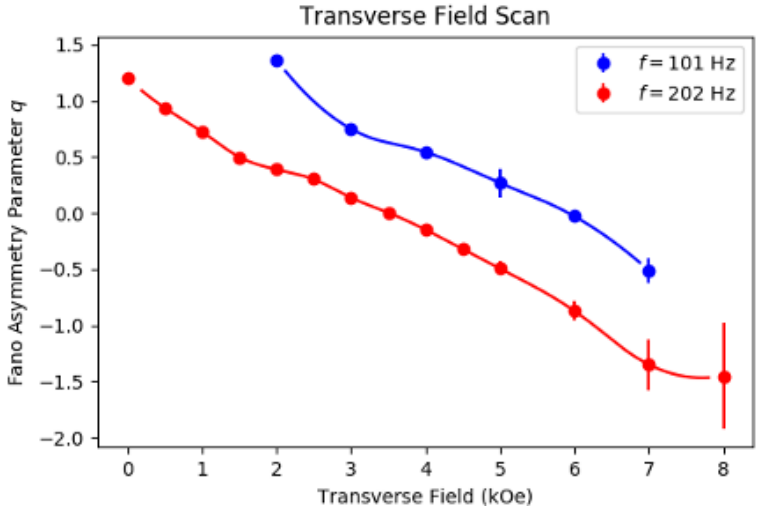

Figure 2.17: Evolution of the Fano q at constant T and h_{pump} as a function of $H_\perp$ for two different pump frequencies. The field at which there is zero-crossing in the Fano q depends on pump frequency for the two transverse field scans.

While one might be tempted to associate the $H_\perp = 3.5$ kOe field scale as a universal zero-crossing in the Fano q since it corresponds with known level-crossings in the single-ion electronuclear Hamiltonian, the $q = 0$ crossing moves to different transverse fields at different pump frequencies as seen in Figure 2.17, suggesting that the interference effects result from more subtle phase-shifts in the transition pathways due to the precise eigenstates of the cluster in question. As different clusters are sampled by changing drive frequencies, their dependence on transverse field and pump amplitude changes due the exact structure of that individual cluster.

2.7 Inferring Dissipation Rates from Experimental Data

In order to determine relevant energy scales and dissipation rates, experimental data from a series of temperatures was fitted to a single Λ scheme. Without loss of

generality, I use the fitting function:

$$(\chi(\delta\omega)+\beta)\,\alpha = \frac{|\mu_{13}|^2(i\gamma-\nu+\frac{H_d^2|\mu_{23}|^2}{4\eta+6i\gamma})}{H_d^2|\mu_{23}|^2-(i\gamma-\nu)(6i\gamma-4(\eta+\nu))} + \frac{|\mu_{23}|^2(i\gamma+\nu+2\delta\omega+\frac{H_d^2|\mu_{13}|^2}{4(\eta+\nu+\delta\omega)+6i\gamma})}{H_d^2|\mu_{13}|^2-(i\gamma+\nu+2\delta\omega)(6i\gamma-4(\eta+\delta\omega))}. \tag{2.29}$$

The parameters α and β are added in order to take into account the experimental measurement procedure, in which the asymptotic behavior (at large detunings $\delta\omega$) of the Fano signal is normalized and isolated from a temperature-dependent background signal. The dissipation rates are modeled to increase linearly with temperature $\gamma = \gamma_0 T$ and insert $\nu = \delta\omega - \epsilon$, $\eta = \omega_d - \Delta$. The energies ϵ, Δ again correspond to the quasi-degenerate, quantum energy splitting and the Ising level splitting, respectively. The drive field amplitude $H_d = 5.7$ MHz corresponds to $h_d = 0.3$ Oe.

The comparison between the theoretical fit and the experimental data is shown in figure 2.18. It shows very good agreement between experiment and the prediction from a single Λ scheme. All curves share the same transition matrix elements $\mu_{13} = 2.3\times10^{-5}$, $\mu_{23} = 7.1\times10^{-6}$, energy levels $\epsilon = 22$ mHz, $\omega_p - \Delta = 21.4$ mHz, and a linearly increasing decay rate $\gamma = 0.48$ mHz $\times\frac{T}{150\text{mK}}$. The parameters α, β display a non-linear temperature dependence with $\alpha = (247, 244, 212, 168, 116)$ and $\beta = (5, 3.8, 2.7, 1.8, 1.1)$ for the temperatures $T = (150, 200, 250, 300, 350)$ mK. The monotonic decrease of these values with temperature is likely to be caused by the general decrease in the measured signal for the susceptibility for increasing temperatures.

2.8 Conclusion

One of the more remarkable features of the de-coupled cluster glass $LiHo_{0.045}Y_{0.955}F_4$ is that it displays non-linearities at energy scales that seem unintuitive. I conclude by connecting both of the non-linear measurements, the inelastic Raman measurements and the asymmetric Fano resonances, and their interpretations with respect to optical analogues.

The relevant energy scales in these susceptibility measurements consist of a temperature $T \sim 100$ mK, a nearest-neighbor dipolar interaction energy $|V_{\text{dip}}| \sim 500$

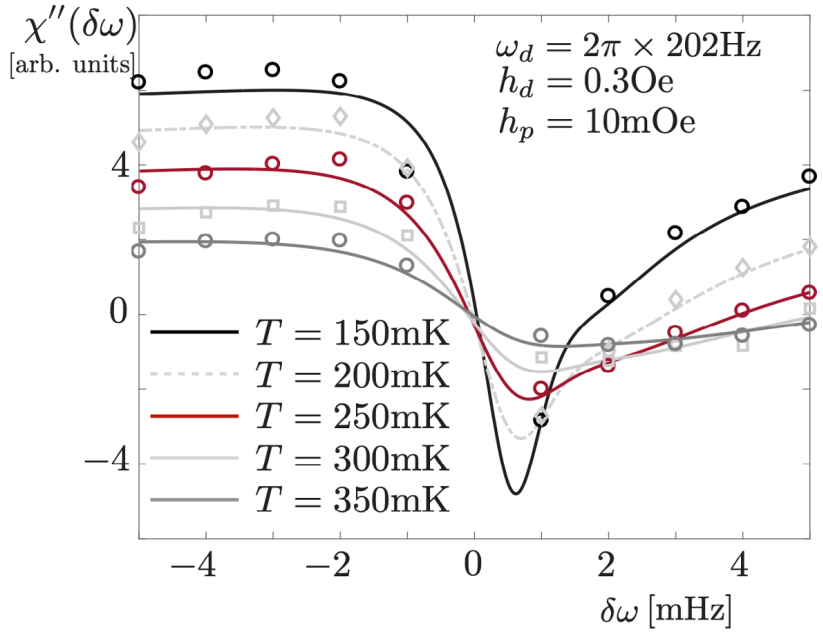

Figure 2.18: Comparing experimental data for the imaginary part of the magnetic susceptibility from a $LiHo_xY_{1-x}F_4$ sample with $x = 0.045$ and theoretical predictions from a single Λ scheme yields very good agreement. The experimental data is represented by markers (circles, diamonds, and squares) and was taken for varying probe field detuning $\delta\omega = \omega_p - \omega_d \in 2\pi \times [-5, 5]$ mHz. The temperature of the sample varies from curve to curve, ranging from $T = 150$ mK to $T = 350$ mK. The lines are predictions for a single Λ scheme with transition matrix elements $\mu_{13} = 2.3 \times 10^{-5}$, $\mu_{23} = 7.1 \times 10^{-6}$, energy levels $\epsilon = 22$ mHz, $\omega_p - \Delta = 21.4$ mHz, and a linearly increasing decay rate $\gamma = 0.48$ mHz $\times \frac{T}{150\text{mK}}$. The parameters α, β display a non-linear temperature dependence with $\alpha = (247, 244, 212, 168, 116)$ and $\beta = (5, 3.8, 2.7, 1.8, 1.1)$ for the temperatures $T = (150, 200, 250, 300, 350)$ mK. The comparison demonstrates that the experimentally observed signal is very well explained already on the basis of a single Λ scheme, and with energy levels and transition matrix elements that agree well with predictions for small magnetic clusters in $LiHo_xY_{1-x}F_4$. The linear temperature dependence of the dissipation rate is in agreement with acoustic phonons at very small energy differences $\sim \omega_d$.

mK, an effective laser frequency of $\omega_p \sim 100$ nK, and a resonance linewidth of $\delta\omega \sim 1$ pK. With a strong Ising moment $|\mu| \approx 6.88\mu_B$, a naïve estimate for the Rabi frequency of a ~ 0.3 G drive field would yield $\Omega_p \sim 2\mu$K. Since the field is aligned along the z axis, if one simply uses the Ising approximation, the commutator $[B^z, \mathcal{H}_{\text{Ising}}] = 0$ vanishes, and the system always remains in an instantaneous Ising eigenstate, and no transitions between states can be driven. However, if one includes off-diagonal terms in the dipolar interaction $V_{ij}^{zx} \sim \sigma_i^z \sigma_j^x$, the $\mathbb{Z}_2$ Ising symmetry is broken, and a longitudinal magnetic field h^z can be transformed into a term $\sim \sigma^x$ which induces quantum fluctuations between states. Since these off-diagonal terms are weak, the matrix elements $\langle \alpha \,|\, g_L \mu_B h^z J^z \,|\, \beta \rangle$ are small, drastically suppressing the effective Rabi frequency. Since these overlaps are small, the system can be driven back into a regime in which the rotating wave approximation is still valid $\Omega_{p,d} < \omega_{p,d}$.

The dominant source of dissipation comes from phonon scattering, in which incoherent spin flips are driven via lattice vibrations. If one decouples the system phonon bath from its environment, one can tune the $LiHo_xY_{1-x}F_4$ phonon linewidth Γ, which is the dominant competing term in the Hamiltonian. The energy splittings (~ 100 nK) are small compared to the environmental bath temperature (~ 100 mK), putting these cluster excitations in the infinite temperature regime. However, even though bath temperatures are high, if the coupling between the bath and the system is weakened sufficiently, the system will not equilibrate, and the relevant energy scale for entering non-linear behavior becomes the dissipation rate due to phonon-scattering, which for low energies is set by the phonon linewidth Γ. Because of this, $LiHo_{0.045}Y_{0.955}F_4$ can be driven into a non-linear response regime with much smaller fields (~ 0.3 G) than would be predicted from typical internal fields (~ 100 G) or temperature scales (~ 100 mK). The reported susceptibility measurements can be understood in the context of optical experiments, with the exception that instead of electric-dipole transitons this system undergoes magnetic-dipole transitions, albeit at effective photon energies of $\sim 10^{-12}$ eV.

First, non-linear behavior is confirmed via inelastic Raman-scattering measurements, in which spectral sidebands are formed when a system is driven with two tones. This non-linear behavior $\sim \chi^{(3)}$ is exponentially-suppressed with temperature, as is the linear response $\sim \chi^{(1)}$ with a similar energy constant ~ 100 mK. Next, I examine the non-linear behavior through the sample response at the probe frequency.

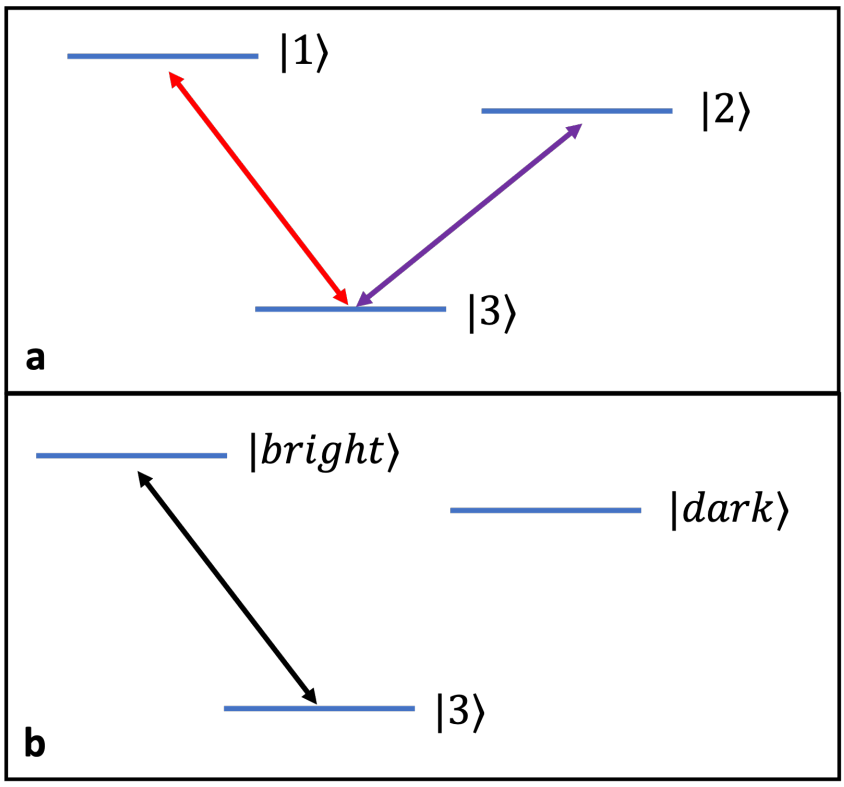

Figure 2.19: An illustration of the two different level schemes of the dressed states for a spin cluster. **a** A traditional V-scheme. **b** at the exceptional points where the Fano asymmetry parameter q vanishes, one of the three states de-couples from the other two, and the two nearly-degenerate states are sorted into a "bright" state that is coupled with the 3rd state, and a "dark" state that is un-coupled from either of the other two.

Using a spin dimer model, one naturally recovers so-called Λ- or V-schemes, in which a 3-state system has one state coupled to a nearly-degenerate pair of states. If this system is driven into a non-equilibrium state (characterized by non-zero off-diagonal elements in the density matrix), there is naturally quantum interference between the two excitation pathways. This interference can be tuned via various macroscopic variables (h_d, $H_\perp$, T), which is observable as an asymmetric Fano resonance in the susceptibility. At special points in phase space (h_d, $H_\perp$, T) where the Fano asymmetry parameter $q = 0$, there is complete destructive interference between both of the excitation pathways, and the sample becomes transparent to the drive field.

A useful alternative description of this phenomena where $q = 0$ can be made via reference to the optical phenomenon known as electromagnetically-induced

transparency (EIT). The destructive interference in the cluster basis can be described through "dressed states," where one describes the states in the rotating laser frame. In this frame, one of the states in the Λ-scheme decouples from the others. Because of this, the dissipation associated with the imaginary susceptibiliy vanishes. I illustrate the two regimes in Figure 2.19.

Chapter 3

DOMAIN WALL MOTION AND NOISE MEASUREMENTS IN A FERROMAGNET

I now turn to a set of experiments that measured the domain wall dynamics of $LiHo_xY_{1-x}F_4$ in a regime (temperature T, external transverse field $H_\perp$, doping concentration x) in which the sample exhibits long range ferromagnetic order. These dynamics were probed using measurements of the bulk magnetization as a sample was driven through many hysteresis loops. I organize this chapter by starting with a discussion of domain walls and disorder in the system. I further describe the experimental procedure used to both acquire and analyze Barkhausen noise data. I show and discuss the shape of the magnetization curves for two samples of different Ho concentrations ($x = 0.40, 0.65$). I then provide an analysis of Barkhausen noise in the $x = 0.65$ sample following traditional critical approaches, explain how the data compare to various theoretical models, and demonstrate how lineshape analysis reveals underlying drag effects. Finally, I move to the $x = 0.40$ sample, and discuss how observed non-critical behavior in the data gives evidence for quantum correlations in macroscopic avalanches.

3.1 Domain Walls and Ferromagnetism

If an external magnetic field is applied parallel to the Ising axis of a ferromagnet, the sample will respond by polarizing its magnetization along the field direction. For small fields this effect is approximately linear, while at large fields the sample saturates at some value that can have dependence on external variables such as temperature. For soft ferromagnets, if a sample is ramped from saturation in one direction $|\downarrow\rangle$ to saturation in the opposite direction $|\uparrow\rangle$, the sample response happens in approximately three stages. First, new $|\uparrow\rangle$ domains will be nucleated within large existing $|\downarrow\rangle$ domains. After enough new $|\uparrow\rangle$ domains are nucleated, they will expand (and consequently $|\downarrow\rangle$ domains will contract) which I describe as motion of the domain wall motion [41]. Wall motion is responsible for the bulk of the magnetization reversal, as it is energetically favored in comparison to the cost of nucleating a new domain, which involves breaking the couplings between all of its nearest neighbors. Finally, close to $|\uparrow\rangle$ saturation, old $|\downarrow\rangle$ domains will be annihilated as they shrink to zero volume.

Even if one ignores domain creation/annihilation processes, the full domain wall problem is incredibly complex, as a fully quantum treatment of the problem involves accounting for multi-particle entanglement between a large number of quantum Ising spins, even before one considers environmental couplings that complicate the problem.

However, while an exact treatment of the quantum domain wall problem remains outside the scope of this experimental thesis, one can frequently make measurements in a regime in which the exact microscopic details are averaged over and/or rendered unimportant, and the statistical behavior of one's sample depends solely on more fundamental properties such as effective dimensionalities and whether the interactions in the problem are long or short range. This was the initial motivation for measuring Barkhausen noise in $LiHo_xY_{1-x}F_4$. For more detailed theoretical treatments of quantum domain wall tunneling, I refer the reader to references: [19, 29, 74, 75].

Barkhausen noise measurement techniques have existed for over 100 years [6], and a litany of ferromagnetic materials have been characterized using this technique. With sufficiently strong disorder, as a ferromagnet is ramped through a hystereis loop via an external magnetic field parallel with the Ising axis, the bulk magnetization does not evolve smoothly, but rather displays a set of discrete jumps as domain walls that are pinned in place by some random pinning potential overcome the pinning and violently snap forward [32]. The statistics in the jumps in magnetization, also known as Barkhausen events, and their correlations, can reveal underlying properties of the sample.

Barkhausen noise is in fact a subset of a more general type of noise in disordered systems–crackling noise, which arises when a system responds through discrete impulsive events over a broad range of sizes. Many systems, including sheared foams [79], fluids in porous media [20], vortex avalanches in superconductors [33], magnetic skyrmions [26], cascading disruptions of power grids [62], and even meme propagation on social media networks [38, 39].

In this chapter, I will discuss measurements using the same century-old Barkhausen technique on another soft, disordered ferromagnet like many before it, but with a few novel properties that expand the class of magnets characterized by the Barkhausen technique. First, $LiHo_xY_{1-x}F_4$ is an electrical insulator [7], and therefore has no dissipation due to eddy currents. Second, the magnetic moments in $LiHo_xY_{1-x}F_4$ are quantum Ising spins, whose dynamics depart from classical behavior when quantum

fluctuations are sufficiently strong.

3.2 Experimental Procedure

In this section, I discuss the experimental procedure used to measure the Barkhausen noise in $LiHo_xY_{1-x}F_4$.

The bulk magnetization was measured using two methods of transduction–a slow ($\sim$ 1 Hz) measurement of the DC magnetization made by a Hall sensor placed on the sample edge, and a faster ($\sim$ 1 MHz) measurement of the time-derivative of the bulk magnetization made by using an inductive copper pickup coil wrapped around the center of the sample. While the measurements of the $x = 0.65$ sample were conducted using an air-spaced coil, a more rigid mount was needed for measurements in a transverse field. Because of the large moments of the rare-earth Ho^{3+} ions, an external field transverse to the Ising axis will not only induce quantum fluctuations between individual spin states, but also produce a macroscopic torque on the entire sample. Without a tightly-fitted mount, the transverse field produced enough torque to shatter the sample.

A new PEEK coil form was machined with a tightly-fitted square pocket to hold the (4x4x8)mm^3 cuboid sample, and a single-layer coil with 100 turns was wrapped around this coil form. Both pickup coils are shown in Figure 3.1. While some signal was sacrificed due to the decreased effective coil filling factor, this PEEK mount was rigid enough to prevent sample destruction under a strong transverse field. A 100-turn inductive pickup coil was wrapped around the center of the sample to measure the time-derivative of the bulk magnetization, and the coil assembly was mounted on the high-purity copper cold-finger of a Helium dilution refrigerator to reach milliKelvin temperatures. External magnetic fields were applied using a superconducting 6T/2T vector magnet, with the longitudinal field ramped between saturation fields $\pm$4 kOe, with a sweep rate $dH_{\parallel}/dt = 11.1$ Oe/s in the adiabatic limit. I checked that I was in the adiabatic limit by comparing results at ramp rates from 1.1 Oe/s to 11.1 Oe/s. For the $x = 0.65$ sample, no field was applied transverse to the Ising axis. In the $x = 0.40$ sample, however, an external transverse field was applied ranging from 0 Oe to 200 Oe. I will discuss in a later section why higher transverse fields were not used.

The raw signal was boosted to detectable levels via a two-stage amplification technique. A superconductive-shielded high-frequency cryogenic transformer (CMR-Direct LTT-h), connected to the mixing chamber of the dilution refrigerator, ampli-

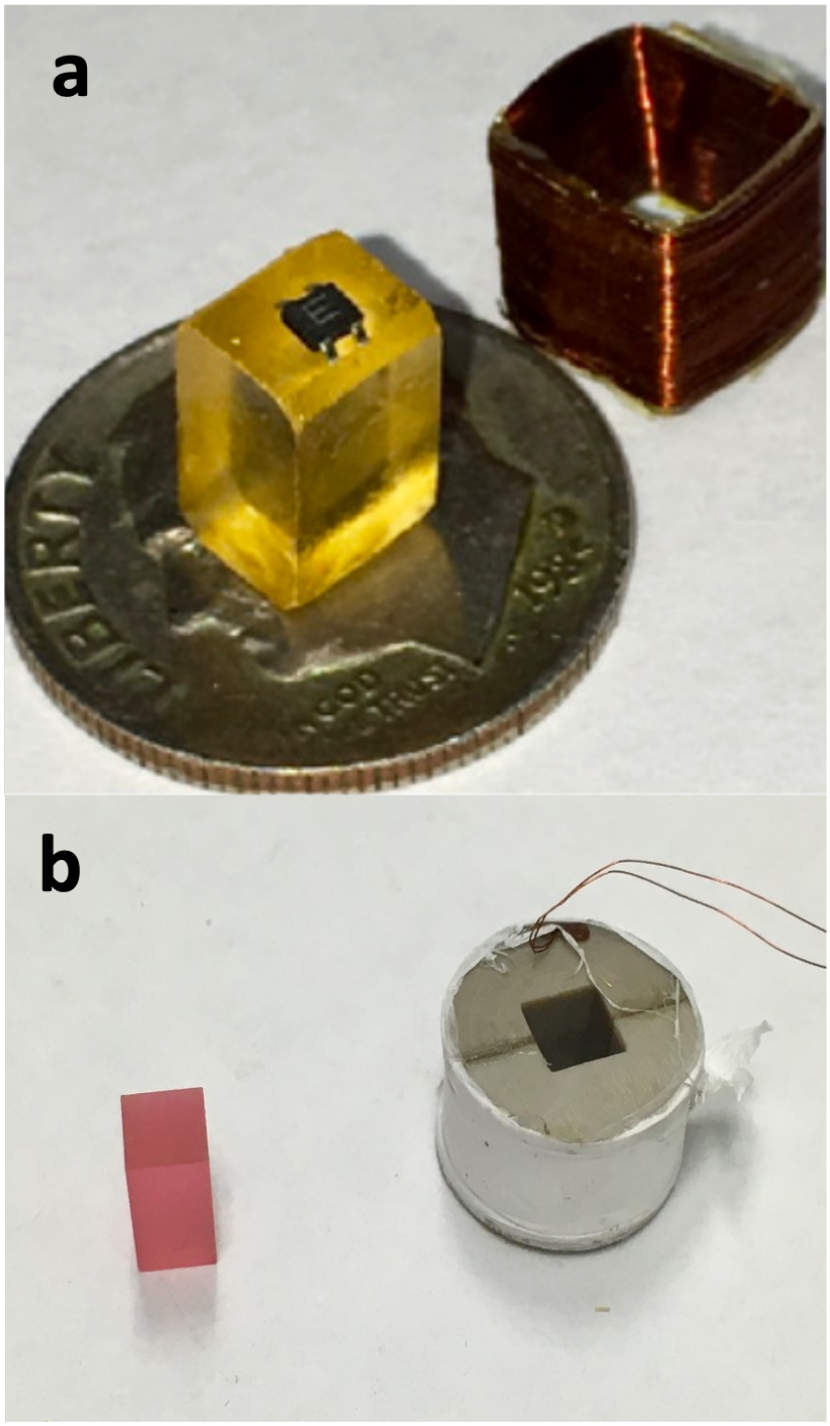

Figure 3.1: Coils used for Barkhausen noise measurements. **a** air-spaced coil used for $x = 0.65$ sample without a transverse field. **b** PEEK coil form used for $x = 0.40$ sample with a finite transverse field.

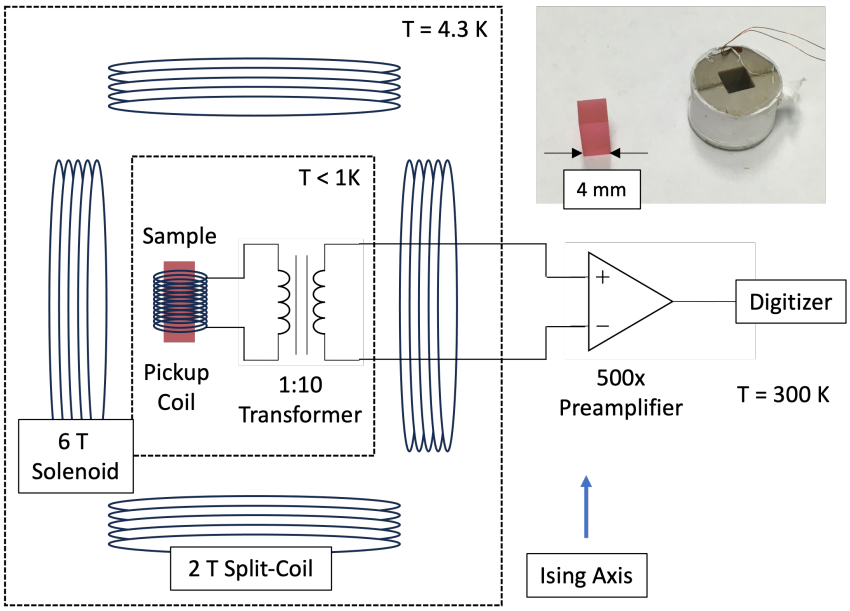

Figure 3.2: Schematic of experimental setup. An inductive pickup coil is wound around the crystal of $LiHo_{0.40}Y_{0.60}F_4$ inside an insulating PEEK coil form. The assembly is mounted on the Cu cold finger of a helium dilution refrigerator equipped with a 6 T/2 T superconducting vector magnet. The induced voltage signal is amplified first by a cryogenic broadband transformer amplifier, and then at room temperature by a low-noise transistor preamplifier, and finally digitized by a streaming oscilloscope. Inset: Photograph of sample and pickup coil assembly.

fied the differential pickup coil signal by a factor of 100 for the $x = 0.65$ sample, and by a factor of 10 for the $x = 0.40$ sample. The lower gain was chosen to extended the measurement bandwidth of the transformer amplifier past 100 kHz. In order to achieve a flat spectral response a resistor was placed to balance the transformer input and output impedences. Furthermore, in order to reduce noise, a metal film resistor was selected for the 15 kΩ resistor needed to match the transformer input and output impedences and mounted to the mixing chamber of the dilution refrigerator to lower its Johnson noise.

A battery-powered low noise preamplifier (Stanford Research SR560) outside the cryostat provided additional gain. The amplified voltage was digitized with a 16-bit 250 kHz digitizer (National Instruments NI-6211) for the $x = 0.65$ sample, and a 16-bit 5 MHz oscilloscipe (Picoscope 4262) for the $x = 0.40$ sample.

For each hysteresis loop, a continuous stream of data was acquired corresponding to a time-trace of the induced pickup coil voltage, digitized at 125 kHz ($x = 0.65$) or 1 MHz ($x = 0.40$), binned in files of length $\sim$ 1 s each. Given that at most $\sim$ 100

events were detected per loop, several hundred loops were needed to acquire enough events from which to draw any reasonable statistical inferences. Since each loop took $\sim$ 10s of minutes to ramp between $\pm \sim 10$ kOe at a rate of ~ 10 Oe/s, the data consists of several weeks worth of continuous 1 MHz sampling, resulting in Terabytes of raw data. In order to process this amount of data, an automated routine was needed for event detection and extraction. This procedure is detailed in this section.

First, a noise floor was defined by fitting the distribution of voltage values to a Gaussian. Since detectable events were sparse ($\sim$ 100 events of duration $<$ 1 ms each per $\sim$ 10 min hysteresis loop), the large voltage values corresponding to avalanche signal did not appreciably affect the fitting of the noise distribution. The background instrumental noise distribution was then characterized using the calculated standard deviation and mean. This DC offset was subtracted off from the raw data, and a voltage threshold was established where the absolute value of the signal was greater than 3.5σ, where σ is the standard deviation of the Gaussian-distributed instrumental white voltage noise. Whenever the measured voltage was above this threshold for >4 consecutive points, the extraction program would register this as an event, and store this clipped waveform, with the ends of the clipped time series defined by a linear extrapolation below the noise floor. The edge extrapolation was tested with various fitting routines and the results were found to be largely insensitive to small changes in regression routines.

The analysis I performed on these extracted events largely consisted of doing one of two things: projecting every event onto a scalar metric, such as total duration, area, etc. and looking at the relative frequencies and/or cross-correlations of these metrics and their dependence on external parameters such as temperature or external transverse field, and lineshape analysis, in which the temporal profile of each event was projected onto a regular mesh through interpolation and normalization, and the resulting normalized lineshapes binned, averaged, and compared to each other.

While not possible with this data set due to how sparse the events were, I note that there is another interesting way of analyzing the data with large enough signal, which is to calculate full two-point time correlators in the voltage over an entire hysteresis loop [78], and compare them to theoretical predictions using functional renormalization group (FRG) calculations [46].

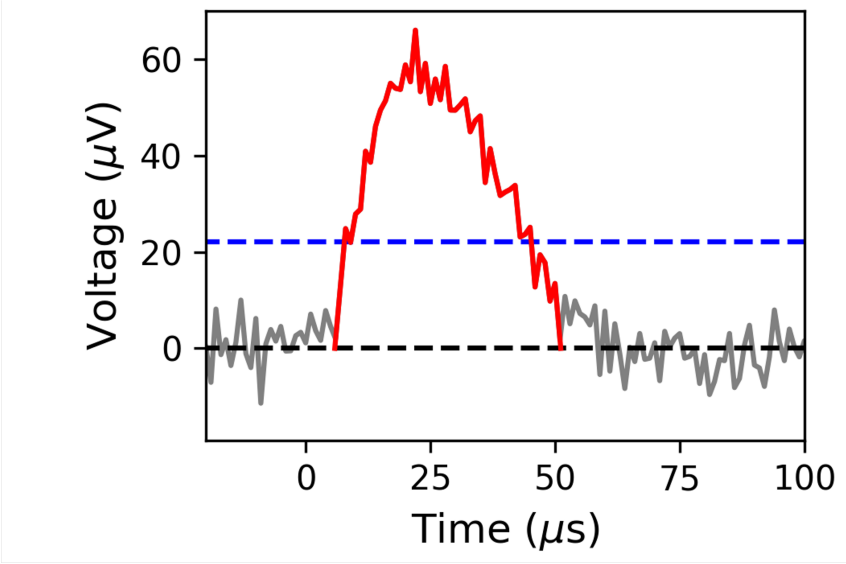

Figure 3.3: A sample event as detected by extraction algorithm. The event threshold is set as the dashed blue line, the raw data is in grey, and the extracted event is in red.

3.3 Hysteresis and Magnetization Loops of Cuboid Samples with $x = 0.65$ and $x = 0.40$

In this section I plot and discuss the magnetization curves and their temperature dependence from both ferromagnetic samples ($x = 0.40$ and $x = 0.65$). The crystals have the same aspect ratio, and thus shape-dependent demagnetization factor.

One convolving factor in Barkhausen analysis comes from having a finite field ramp rate. While predictions of critical behavior are made in the limit of infinitely slow driving, there should be a regime in which the driving is effectively adiabatic. In a Landau-Zeener formulation, one can quantify the driving rate as the time-derivative of the Zeeman energy splitting in the two Ising levels as the external field is ramped. The ramp rate used in these experiments was $dH^{\parallel}/dt = 11.1$ Oe/s, resulting in a rate of change of splittting $d(E_2 - E_1)/dt = 10.23$ mK/s. This makes our 11.1 Oe/s ramp rate adiabatic if the strength of the quantum fluctuations from off-diagonal matrix elements in the Hamiltonian are greater than 0.716 μK. While the tunneling calculation is complicated by the strong hyperfine coupling of the electronic spins to the Ho^{3+} nucleus, it is probable that the average random local transverse field on each spin is great enough such that 11.1 Oe/s is slow enough to be in the adiabatic regime.

The magnetization curves of both samples are plotted in Figure 3.4. Both samples

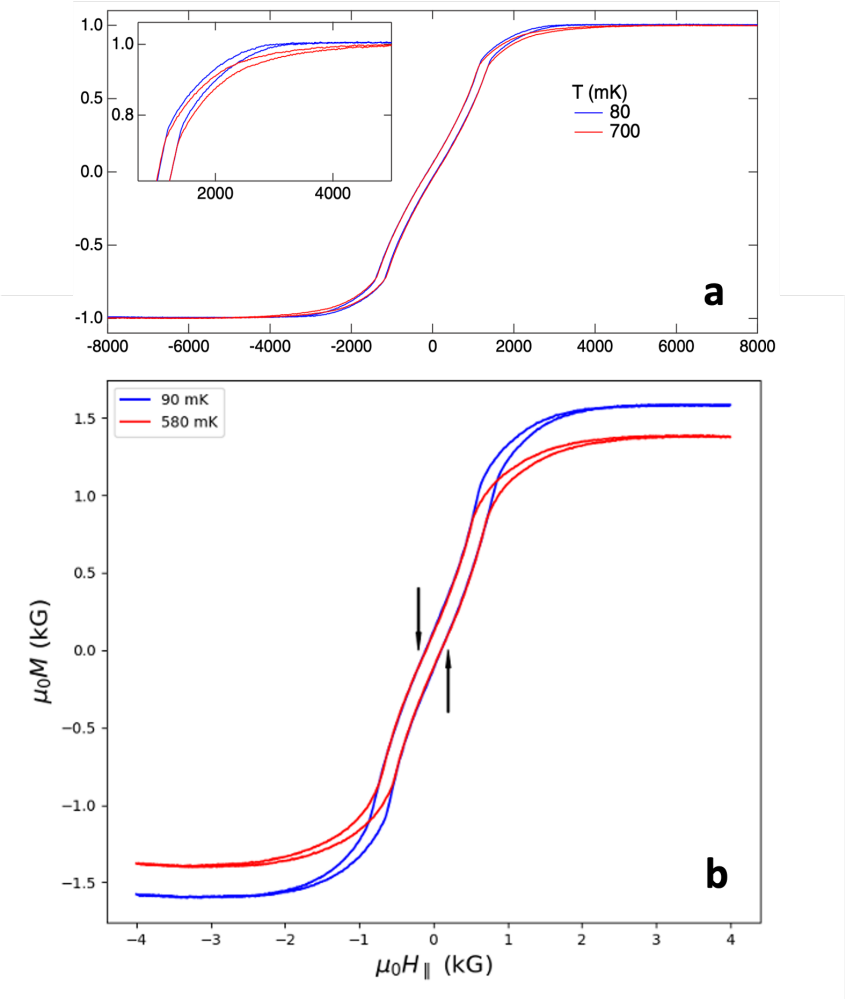

Figure 3.4: The magnetization loops at different temperatures for **a**: the $x = 0.65$ sample and **b**: $x = 0.40$ sample.

display the same characteristics of a soft ferromagnet–a narrow hysteresis loop with low coercivity with a low-field quasi-linear regime, plateauing at a saturation magnetization at higher external longitudinal field. This "softness" of the magnet is frequently found in dipolar-coupled ferromagnets such as $LiHo_xY_{1-x}F_4$ [41]. As discussed in the beginning of this section, the magnetization evolution process over a full hystersis loop for these soft ferromagnets occurs by two separate processes: domain creation/annihilation that occurs at high fields near saturation, and domain wall motion, where a pair of domains shrinking/growing is mapped from the spin problem to its dual–the motion of the boundary between the two domains.

It is not surprising that there is temperature dependence in the saturation magnetization, as the saturation magnetization is a measure of the thermodynamics equilibrium

population and size distribution of oppositely-oriented domains, which is determined by a tradeoff between the magnetostatic energy due to the interaction of the domain with the external field, the magnetostatic energy in the demagnetization field, and the entropy gained due to multiple domain configurations. As can be seen in Figure 3.4, both samples reach a decreased saturation magnetization at higher temperatures, which matches what you would expect from thermally-populated domains oriented anti-parallel to the field direction.

However, in contrast to the temperature dependence in the high-field regime, the low-field, quasi-linear regime of the hysteresis loop is entirely temperature independent up to 0.95 of the Curie Temperature T_c, which rules out thermal activation as the dominant activation mechanism–leaving only quantum tunneling mechanisms as possibilities.

It should be noted that the behavior of these cuboid samples differ from other measurements reported in the literature, most notably [69]. In particular, as the temperature was raised in the $x = 0.44$ sample in [69] close to T_c, the loop narrowed dramatically, from a width of around 100-200 Oe, to a width of less than a few Oe. The dramatic difference in temperature dependence between the two samples is attributed to the shape-dependent demagnetization factor, since my measurements were in cuboid samples with an aspect ratio of 1x1x2, while the sample in [69] was a needle. The more flattened geometry increases the distribution of random fields in the sample due to the combination of the anisotropic dipolar interaction and the quenched disorder from site dilution.

I will emphasize here that the effect of disorder in $LiHo_xY_{1-x}F_4$ is non-trivial; the dipolar interaction has all terms $\sim \sigma_i^\mu \sigma_j^\nu$ with $\mu, \nu \in \{0, x, y, z\}$. The first term $\sim C_{zz}^2 \sigma_i^z \sigma_j^z$ results in a random longitudinal field that raises or lowers the effective field needed to induce a spin flip. The second term $\sim C_{zz} C_x \sigma_i^z$ mixes the tilted spin polarization in the transverse direction into an effective random longitudinal field. Finally, the third term $\sim C_{zz} C_{xx} \sigma_i^z \sigma_j^x$ induces quantum fluctuations on one spin due to the dipolar field from the Ising source.

With strong enough random longitudinal fields, thermal fluctuations are not strong enough to overcome the wall pinning, and the domain wall motion is dominated by quantum, rather than thermal, fluctuations. The temperature independence of the quasi-linear portions of the magnetization loops for the cuboid $x = 0.65$ and $x = 0.40$ samples are the result of domain walls whose motion is dominated by quantum tunneling. I note that this tunneling is broken up into many independent

tunneling events, rather than one fully coherent macroscopic tunneling event. While the tunneling of small sections of domain wall is a complicated theoretical problem from first principles, one can instead measure correlations between tunneling events, whose statistics are governed by spatial correlations in the domain wall pinning potential due to random longitudinal fields.

3.4 Power Law Fits and Lineshape Analysis of Barkhausen Noise in $LiHo_{0.65}Y_{0.35}F_4$

Systems near criticality exhibit scaling relations and power law behavior between various quantities in each system, and the exponents corresponding to these scaling relations help elucidate the underlying mechanisms and universality class for a particular system. For $LiHo_{0.65}Y_{0.35}F_4$, Barkhausen events were extracted from measurements of many hysteresis loops, and each extracted event was mapped to a scalar metric–usually a normalized n-th moment of the event lineshape. In Figure 3.5 I plot 1-dimensional histograms of the probability distribution function (PDF) for each of the following metrics: duration ($T = t_f - t_i$), area ($S = \int_{t_i}^{t_f} dt' V(t')$), energy ($E = \int_{t_i}^{t_f} dt' V^2(t')$). While not a PDF for a scalar event metric, the power spectral density is also included in Figure 3.5, as it displays approximate power law behavior over a limited regime. Critical exponents were extracted by fitting the data in the region that exhibited power law behavior. I excluded the low and high tails of the data because of limitations in the instrumentation signal-to-noise, which artificially precludes small events from being detected, as well as a well-known phenomenological large-event cutoff due to demagnetization effects.

The power law forms are given as follows: a) energy ($P(E) \sim E^{[(\tau-1)/(2-\sigma\nu z)+1]}$), b) area ($P(S) \sim S^{-\tau}$), c) power spectral density ($S(\omega) \sim \omega^{-1/\sigma\nu z}$), d) duration ($P(T) \sim T^{-\alpha}$). The numerical values of the fitted exponent are found to be: a) $[(\tau-1)/(2-\sigma\nu z)+1] = 1.7 \pm 0.1$, b) $\tau = 1.7 \pm 0.2$, c) $1/\sigma\nu z = 1.7 \pm 0.1$, and d) $\alpha = 1.8 \pm 0.2$.

There are many models used to simulate Barkhausen noise in a disordered ferromagnet that can be subdivided broadly into two categories: random energy models in which the bulk magnetization is mapped onto an effective domain wall coordinate, whose equation of motion is given by a Langevin equation, and spin models that start from the microscopics of a problem and are generally either numerically simulated [65] or solved using renormalization group methods to calculate critical exponents in scaling law behavior [24]. The following disordered spin Hamiltonians have been studied in the literature [80]. The first is is the random field Ising model (RFIM)

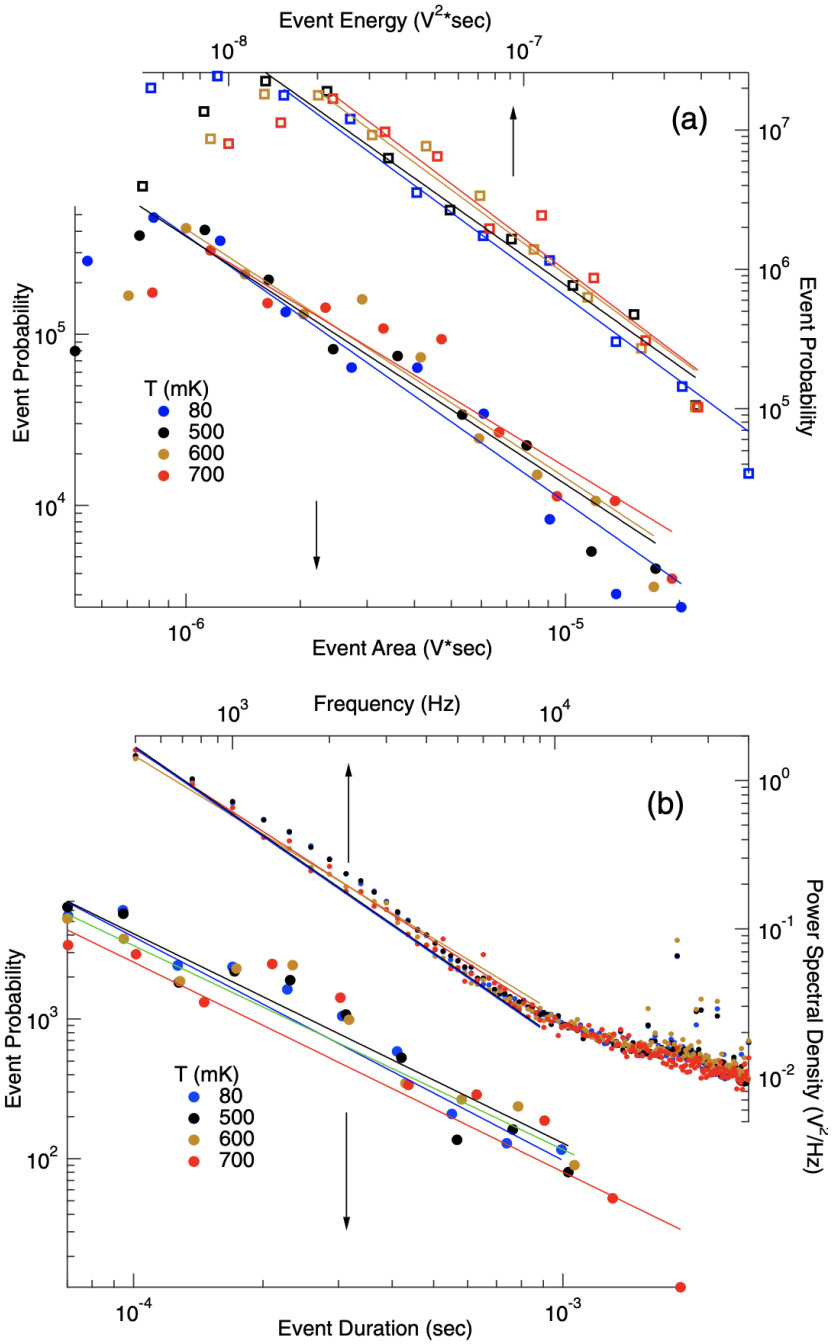

Figure 3.5: Histograms of various metrics in Barkhausen noise for a 1x1x2 cuboid sample of $LiHo_{0.65}Y_{0.35}F_4$. **a** Energy E with fitted power law exponent $[(\tau-1)/(2-\sigma\nu z)+1] = 1.7 \pm 0.1$ and Area S with fitted power law exponent $\tau = 1.7 \pm 0.2$. **b** Power spectral density $S(\omega)$ with fitted power law exponent $1/\sigma\nu z = 1.7 \pm 0.1$ and Duration T with fitted power law exponent $\alpha = 1.8 \pm 0.2$.

in which the disorder is represented as a spatially-random longitudinal field on each site, giving rise to the RFIM Hamiltonian:

$$\mathcal{H}_{\mathrm{RFIM}} = -J \sum_{i,j} s_i s_j - h \sum_i s_i - \sum_i h_i s_i, \tag{3.1}$$

where s_i is the spin variable as site i, J is the nearest-neighbor spin-spin coupling strength, h is the external longitudinal field, and h_i is a site-dependent random field. The disorder can also be represented as a random coupling strength J_{ij} between spins in the random bond Ising model (RBIM):

$$\mathcal{H}_{\mathrm{RBIM}} = -\sum_{i,j} J_{ij} s_i s_j - h \sum_i s_i. \tag{3.2}$$

An equivalent representation is the site diluted Ising model (SDIM), in which spins are randomly either occupied ($c_i = 1$) or unoccupied ($c_i = 0$), with Hamiltonian:

$$\mathcal{H}_{\mathrm{SDIM}} = -J \sum_{i,j} c_i c_j s_i s_j - h \sum_i s_i. \tag{3.3}$$

Finally, the random anisotropy Ising model deals with domains with random anisotropy axes, which is not relevant to $LiHo_xY_{1-x}F_4$, but given below where each $\vec{n}_i$ is a random unit vector giving the local anisotropy axis, with associated Hamiltonian

$$\mathcal{H}_{\mathrm{RAIM}} = -J \sum_{i,j} s_i s_j \vec{n}_i \cdot \vec{n}_j - \vec{h} \cdot \sum_i s_i \vec{n}_i. \tag{3.4}$$

While all of these models have been simulated numerically, only the RFIM has been studied in detail. As the strength of the disorder (the variance of the random field h_i) is tuned, the system undergoes a continuous phase transition, that is best understood under renormalization group theory [24]. Originally a technique used to study how coupling strengths change at different length/energy scales in quantum field theories [82], the renormalization group discusses how the effective equations of motion for the system evolve when measurements are made at different length scales. The procedure involves iteratively coarse graining the system–integrating small length/high momentum degrees of freedom and renormalizing the coupling strengths between the remaining effective degrees of freedom [82]. As the system is progressively more and more coarse grained, the characteristic avalanche length

scale either flows towards infinity for small disorder or towards zero for strong disorder [57]. Separating these regimes is an unstable fixed point at which the phase transition occurs. At this critical value of disorder, the system loses all length scales, and displays self-similarity, with fractal avalanches at all length scales.

According to the RFIM, power laws in the data manifest simply because of proximity to a disorder-driven phase transition [57]. At first it may seem surprising that any power laws would be predicted, since the sample disorder was not carefully chosen to be perfectly fine tuned to the critical spin concentration, but the nature of the phase transition is that it has a large critical region, so that power laws are present over large regimes even for disorder significantly away from the critical value [57]. Given that power laws are seen for only one decade in the experimental data, it is possible that simple proximity to a critical point could be the source of the underlying criticality and resulting power laws, assuming that the disorder for the $x = 0.40, 0.65$ samples is greater than the critical disorder.

Beyond spin models one can also model the domain wall dynamics using a domain wall de-pinning model. In this model the system is recast to a continuum model in which the dynamics of a two-dimensional elastic interface are solved for in a highly-damped regime [31]. Since high dissipation is assumed, the domain wall motion can be modeled as a random walk, and a Fokker-Planck equation of motion can be derived from the Hamiltonian [2]. Criticality results from the fact that demagnetization fields act as a restoring force, which keep the effective force on the domain wall close to the critical de-pinning force [84]. This self-organized criticality does not arise from proximity to a phase transition, but because dynamical effects self-stabilize the system and naturally drive it towards a critical point. This model can be solved using formal renormalization group calculations, and scaling laws can be derived in two cases: with and without long-range interactions [31]. For the case with long-range dipolar forces, I recover mean-field behavior, and the calculation agrees with the celebrated ABBM model [2], in which power laws result from spatial correlations in the disorder.

Although the reported exponents α and τ do not fall exactly onto the theoretical exponent values for either of the usual universality classes seen in Barkhausen noise experiments ($\alpha = 2.0, \tau = 1.5$ for the long-range domain wall depinning universality class, and $\alpha = 1.5$, $\tau = 1.27$ for the short-range domain wall depinning class), to within error bars, the exponent relationship $\frac{\alpha-1}{\tau-1} = \frac{1}{\sigma\nu z}$ characteristic of avalanches holds [31]. Finite size effects, small scaling regimes, disorder, and other effects

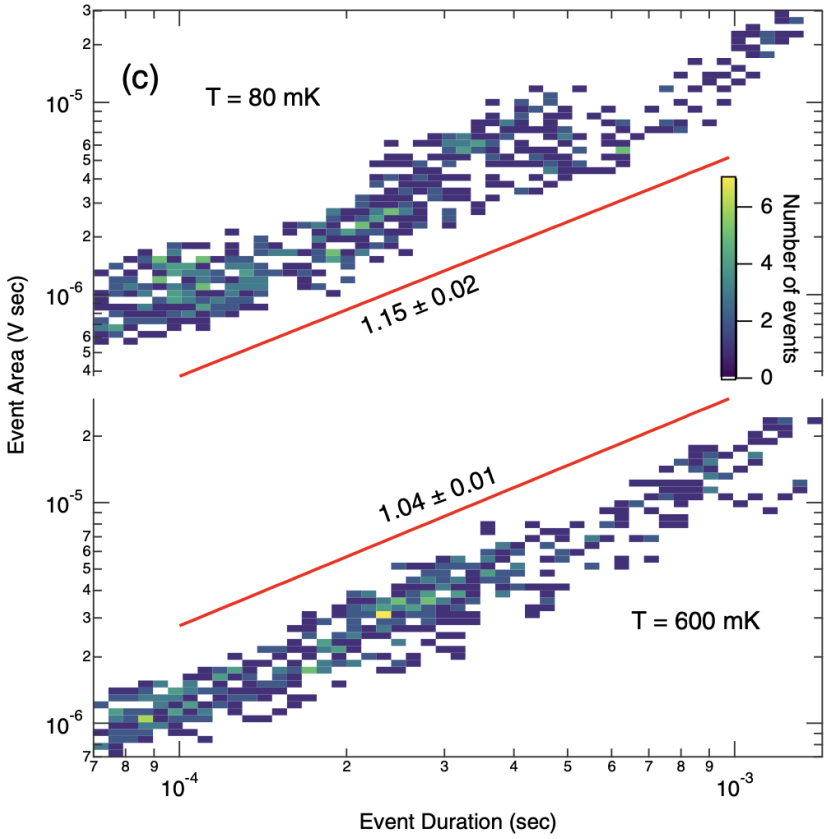

Figure 3.6: Bivariate histograms of event probability vs area and duration at T=80 mK and 600 mK, showing an approximately linear relationship with no well-defined crossover. Lines are best-fit power laws (offset for clarity).

are known to skew the measured values for the scaling exponents compared to the theoretical values extracted through finite size scaling and simulations of large systems [58]. The exponent values extracted here do in fact fall within the range of exponent values that have been quoted in the literature for other experiments that belong to the long range depinning universality class or the random field Ising model (RFIM) universality class for Barkhausen noise in disordered magnets [66], for which simulations [58] predict $\tau = 1.6$ and $1/\sigma\nu z = 1.75$, and $\alpha = 2$ and $([(\tau-1)/(2-\sigma\nu z)+1] = 1.42)$. Future studies of the history dependence along the lines of Ref. [16] could help narrow down the underlying universality class further.

I plot in Fig. 3.6 the occurrence rate of avalanche events as a function of event area and duration, and fit each bivariate histogram to a power law. I find that the data is consistent with a power law exponent of 1 across the entire distribution at all T. It is likely that this exponent for the entire range includes strings of temporally overlapping avalanches, possibly through thermally triggered "aftershocks" of

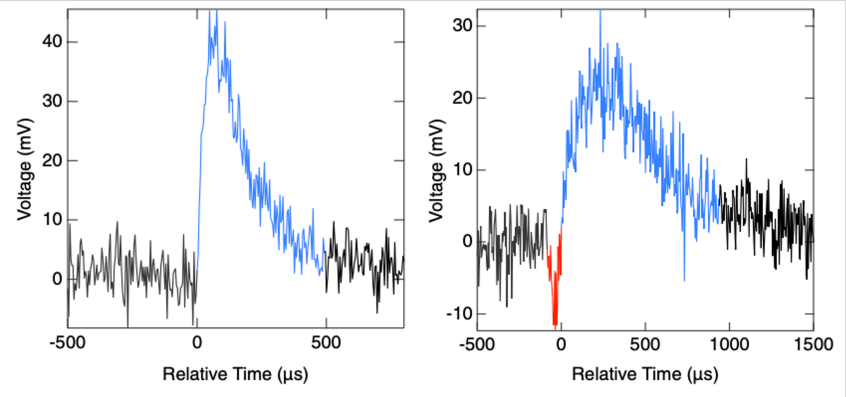

Figure 3.7: Voltage time series showing a long-duration event with an opposing-polarity precursor stage.

avalanches. Such overlaps of avalanches are known to produce size versus duration exponents around 1 [81]. Alternatively, I note that the event distribution at 80 mK appears to segregate into three visually-distinct regimes; if the power law fit is constrained to the central section (spanning 160 to 500 μs), I obtain a value of $1/\sigma\nu z = 1.5 \pm 0.1$ This suggests the possibility that the central regime may be the true avalanche scaling regime, but the limited range over which this behavior occurs prevents us from making a more definitive statement. The additional number of events associated with the crossover into this possible scaling regime is also visible in the duration probability histograms in Fig 3.5b as a small "bump" above the trend lines for the bins around 200 μs. Applying an external transverse field and thereby inducing quantum fluctuations potentially could broaden this postulated scaling regime, allowing for a more robust analysis.

As illustrated in Fig. 3.7, a small fraction of the observed events are preceded by a smaller precursor feature of opposite sign. Some spins actually reverse against the direction of the local magnetic field immediately prior to the more typical domain reversal event where spins realign to point along the magnetic field. Such a counter-intuitive effect is possible due to the dipole nature of the interspin coupling in $LiHo_xY_{1-x}F_4$, where for some relative orientations the dipole coupling can be anti-ferromagnetic. Temporary reconfigurations of the spins to oppose the magnetic field can be energetically favorable locally, and hence enable a reverse-polarity switching event. Analogous behavior has been observed in plastic deformation of sheared materials, where local pinning sites similarly can distort the free energy landscape and allow for seemingly "uphill" motion. [56, 77] Numerical simulations of domain-wall motion in disordered perpendicular-anisotropy thin films [42] likewise have

observed a small fraction of reverse-polarity events. The occurrence probability of these precursor events is strongly temperature dependent, with approximately 5% of the 80 mK events showing a precursor, decreasing to 1% at 250 mK and less than 0.1% at 500 mK and above where thermal fluctuations dominate.

3.5 Dissipation and Lineshape Asymmetry in $LiHo_{0.65}Y_{0.35}F_4$

While models of closed dynamics for domain walls yield symmetric average lineshapes, it has been known that dissipative effects can cause lineshape asymmetries for many physical systems including fluid flow in disordered nanoporous materials [21], dislocation avalanches in metallic microcrystals [73], and creep rupture in heterogenous materials [25]. In bulk metallic ferromagnets, the origin of these drag effects has been ascribed typically to eddy-current back-action. However, $LiHo_{0.65}Y_{0.35}F_4$, which is electrically insulating, cannot sustain eddy currents, so one must look beyond conductivity-related mechanisms in order to explain the observed drag. Furthermore, the typical modeling of drag in spin dynamics via the Landau-Lifshitz-Gilbert (LLG) equation does not directly apply here due to the $S = 1/2$ Ising nature of the spins, which precludes the spin-precession dynamics that underly the LLG approach. While there is a low equilibrium phonon density since measurement temperatures are approximately three orders of magnitude lower than the Debye temperature $\Theta_D = 560$ K for the $Li(Ho,Y)F_4$ family [1], it is known that a strong thermal coupling between the $Li(Ho,Y)F_4$ crystal phonons and an external heat bath can set a floor on the effective phonon density of states (DOS), and therefore the low energy dissipation rates [15]. It has been shown in previous experiments on $LiHo_xY_{1-x}F_4$ that domain-pinning arising from random fields, due to the quenched disorder from the dilution of the ho^{3+} ions by Y^{3+} ions, widens the hysteresis loop, which corresponds to greater dissipation of energy [69]. There is limited work on the phonon-coupling in $LiHo_xY_{1-x}F_4$ [9], and the exact nature of how random fields affect the spin-lattice coupling is still an open question.

I show in Fig. 3.8a and b scaled curves as a function of temperature for short (<150 μs) and long (>500 μs) time events, respectively. Following the approach in Ref. [14], I construct the scaled curves by first normalizing the time axis for each event by its individual duration, normalizing the voltage such that the total integrated area is equal to 1, and finally averaging the voltage as a function of normalized time across all events for a given temperature and duration bin. Despite the absence of eddy currents in insulating $LiHo_{0.65}Y_{0.35}F_4$, clear early-time asymmetries characterize a number of the curves in both time bins, indicating the presence of alternative

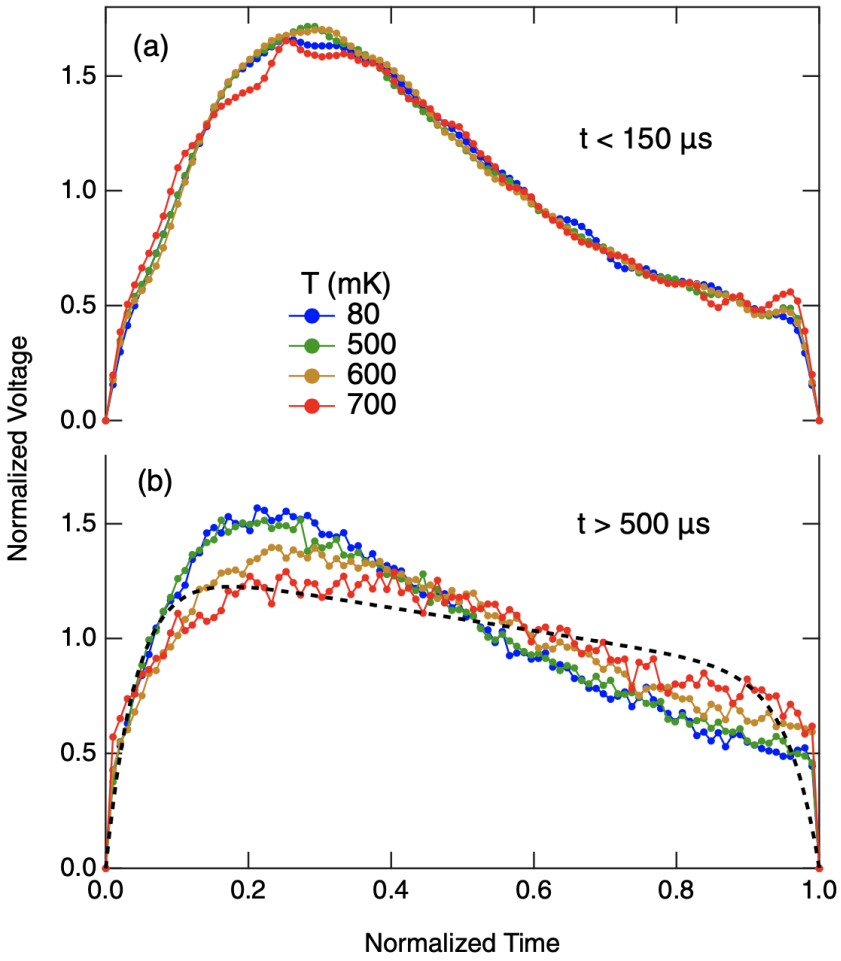

Figure 3.8: Evolution of lineshape as a function of temperature and event duration, showing the onset of drag effects. (a,b) Average scaled event shape vs. scaled duration (see text for details on averaging and scaling process) for short (<150 μs) and long (>500 μs) events, respectively. Dashed line is a fit at T = 700 mK to the ABBM model incorporating shape demagnetization and a phenomenological skew term. [85]

sources for drag effects. I also include in Fig. 3.8b a fit of the 700 mK data to the ABBM model incorporating both demagnetization effects and a phenomenological linear skew term [85]. This ABBM-based model only accurately fits the observed data for long events at high temperature, with noticeably different shapes appearing in the short-time, low-temperature limit. These deviations point to a crossover to a different set of domain dynamics and consequent change In universality class away from mean-field [27, 45].

The evolution of the asymmetry in the scaled lineshapes can be described quantitatively by calculating a normalized skewness [85] for the scaled lineshapes at each temperature/duration bin. For short events (<150 μs), the skewness was essentially constant as a function of temperature, equal to 0.46 ± 0.01 for all temperatures between 80 and 700 mK. By contrast, for longer events (>500 μs), the skewness decreases monotonically with increasing temperature, from 0.42 at 80 mK to a much more symmetric 0.18 at 700 mK. The overall trend is for longer events at high temperatures to tend towards lower skewness, similar to what has been observed in Barkhausen measurements on metallic ferromagnets [22, 85], but opposite to the behavior of non-magnetic crackling noise systems such as yield transitions in sheared amorphous solids [49], granular media [5], and earthquakes [50].

The shorter duration events shown in Fig. 3.8a demonstrate only a weak dependence of average skewness on temperature. The long duration events of Fig. 3.8b, however, see approximately a factor of two decrease in skewness at 600 and 700 mK compared to the same duration bins at low temperature, indicating that drag effects are becoming proportionally less important in the dynamics of those events. While the short events correspond to individual domain reversals whose dynamics are dominated by the drag-inducing microscopic pinning landscape, the longer events represent a linked cascade of reversals more strongly dependent on the strength of thermal fluctuations, which overcome local pinning mechanisms.

3.6 Beyond Criticality: Quantum Co-Nucleation of Domain Wall Pairs in $LiHo_{0.40}Y_{0.60}F_4$

The same Barkhausen noise measurements were repeated on the $x = 0.40$ sample. While the shapes of the magnetization loops were qualitatively identical, the statistics of the fast avalanche events were drastically different than those of the $x = 0.65$ sample. In particular, the data appear to not only depart from criticality, but to exhibit two distinct domain activation mechanisms.

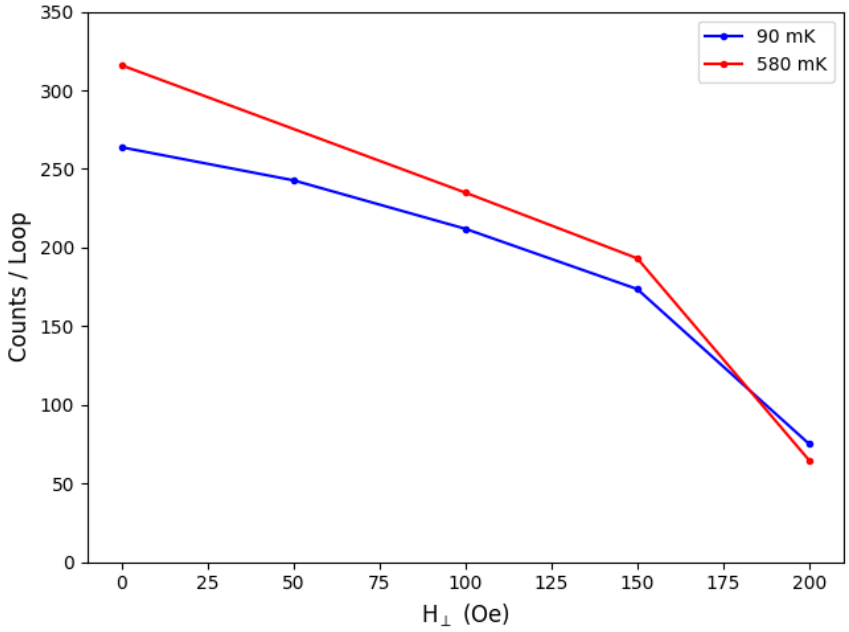

Figure 3.9: Frequency of total number of observed Barkhausen events per hysteresis loop for low (blue, 90 mK) and high (red, 580 mK) temperatures for a range of transverse fields.

I note that the only events that I am able to observe correspond to the largest avalanches. The detectable avalanches range in size from $\approx 2 \times 10^{-10}$ Wb $\rightarrow$ 6×10^{-9} Wb, corresponding to avalanches containing a number of spins N between 1.5×10^{15} and 4.5×10^{16} spins. The change in the macroscopic magnetization over the full hysteresis loop (Fig. 3.4b) is actually dominated by the multiplicity of smaller domain flips below our noise floor, with the change in magnetization due to the measured large events contributing anywhere from $\sim 0.01\%$ (at $H_\perp = 0$) to $\sim 0.1\%$ (at $H_\perp = 200$ Oe) of the total change in magnetization of the entire sample over the full loop. All events were observed in a narrow region between 150 Oe $\leq H_\parallel \leq$ 200 Oe) while ramping up, and at the equivalent negative field while ramping down (marked by arrows in Fig. 3.4b). By contrast to previous susceptibility measurements [14] that measured only the domain walls with weakest pinning, in this experiment I measure only the most strongly-pinned domain walls.

While traditional Barkhausen analysis consists of deducing the underlying universality class by means of extracting the critical exponents through power law fits of event statistics [57, 84] or by using lineshape analysis to learn about underlying dissipative or demagnetization effects [30, 55, 71, 85], this is not appropriate here because our data do not display the standard power laws characteristic of universal-

ity. Instead, one observes two distinct classes of events, presumably corresponding to two different domain-wall activation mechanisms, that show remarkably different dependences on applied transverse fields. The dependence on transverse of the total number of events is shown in Figure 3.9

The non-critical behavior is most easily observed by comparing the two-dimensional histograms plotting the cross-correlation between event duration (T) and area ($S = \int_0^T V dt$) for the most extreme temperatures (90 mK and 580 mK) and transverse fields (0 Oe and 200 Oe). As seen in Fig. 3.10a, the events separate into two distinguishable classes at low fields: one class that I label as "independent" that approximately spans a power law with an exponent of ≈ 1.1 (close to the power of 1 indicative of avalanches [55]) over approximately one decade of duration, and the second that I designate "cooperative" (highlighted by the red oval in Fig. 3.10a that appears as an approximately Gaussian cluster over a more limited range of durations with higher areas for any given duration than events in the "independent" class. Furthermore, while the frequency of the "independent" events decreases only modestly with transverse field, the "cooperative" events are suppressed almost completely with a 200 Oe transverse field. I have plotted one sample event in each class in Fig. 3.10b, both marked by arrows on the 2d histograms in Fig. 3.10a, with the "cooperative" event in red and the "independent" event in orange.

In the following discussion, I discuss the possible origins of these two activation mechanisms, as well as phenomenologically explain why such a small 200 Oe transverse field could suppress the "cooperative" events starting from the microscopic Hamiltonian.

First, I deduce that both activation mechanisms are quantum mechanical in nature. Like the magnetization curves within the linear regime, the event statistics show the same temperature independence, demonstrating that within these experimental parameters, the sample is deep within the quantum regime, where the dynamics are governed by quantum tunneling, rather than thermal activation, of spins.

Given that both activation mechanisms are due to quantum tunneling (rather than one being quantum and the other thermal), it is not immediately obvious how there could be two different tunneling mechanisms, why they would have such dramatically different transverse field dependence, or how such a small 200 Oe field could suppress markedly either class of events.

Given this challenge, it is necessary to go beyond the theoretical picture of a single

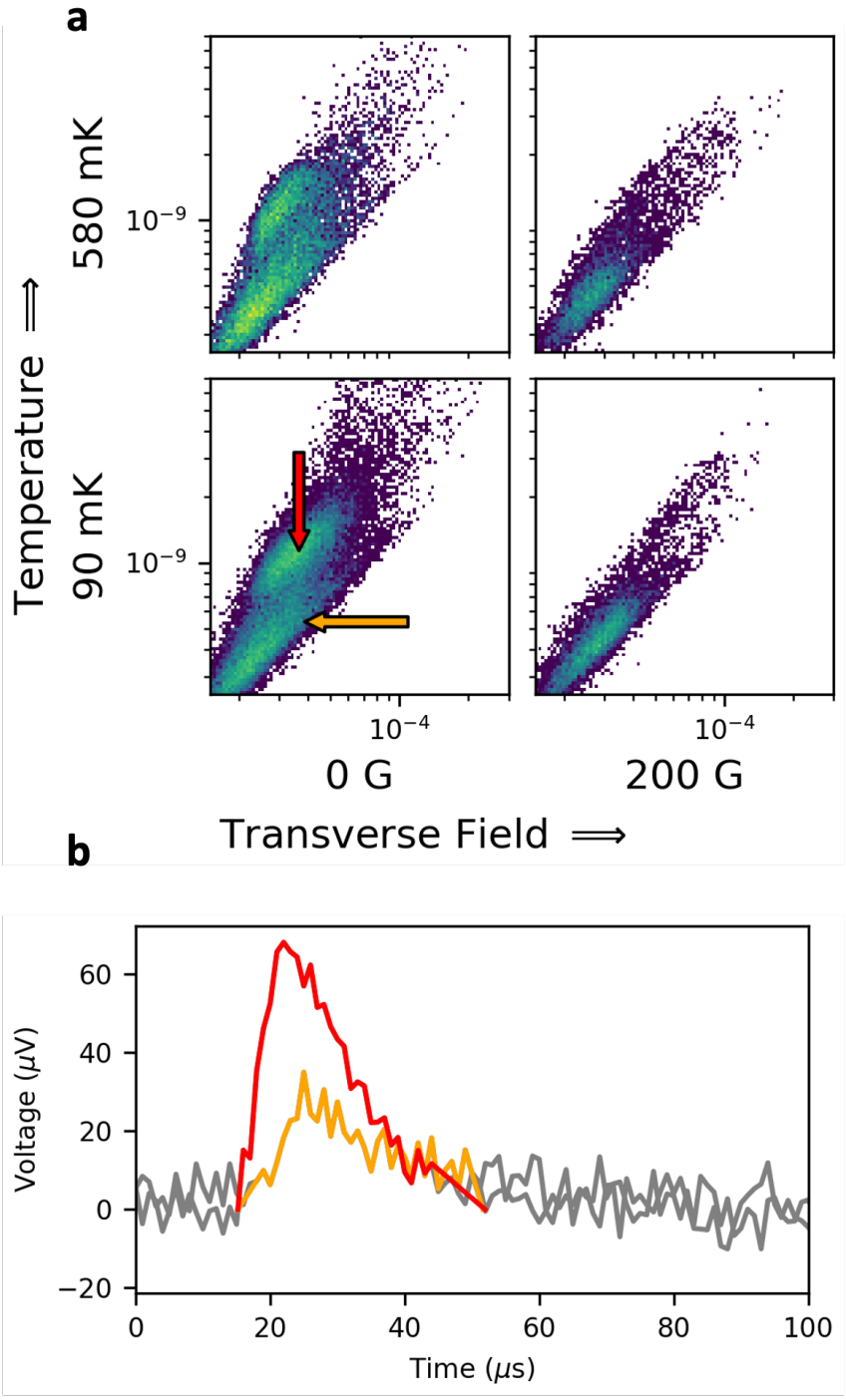

Figure 3.10: Classes of events. **a** 2D histograms of event area (y-axis, $V \cdot s$) vs event duration (x-axis, s) for low/high temperatures and transverse fields. **b** Sample events of each class: "independent" event in orange, and "cooperative" event in red as indicated by the colored arrows in **a**.

independent wall tunneling and consider the interaction between walls. In so doing, one can recover a phenomenological model in which the two different activation mechanisms correspond, on one hand, to walls tunneling independently of each other and, on the other, to cooperative tunneling of pairs of walls. Co-tunneling of domain walls is strongly affected by the application of an external transverse field much smaller than the fields required to induce single-spin tunneling.

I consider a model in which a single plane wall, or an adjacent pair of walls, can displace themselves through the system. For a more detailed treatment, I refer the reader to the supplemental information of [72].

Even without disorder (for $x = 1$), the walls are pinned by a lattice periodic potential. Wall displacement then occurs by the nucleation of plaquettes of a displaced wall (Fig. 3.11a). This occurs by tunneling through a barrier created by the line tension in the plaquette periphery and the tunneling is driven by an applied longitudinal field. Plaquettes can nucleate at different parts of a wall, as well as on top of each other; they are the 2-dimensional lattice version of quantum bubble nucleation [54].

In addition to the independent tunneling processes of a single plaquette, there are co-tunneling processes involving the dipolar interaction between two plaquettes. The interaction term between two plaquettes, ΔU_{12}, as a function of the radius of each plaquette, R_i, is given by:

$$\Delta U_{12} = -\frac{\mu_0}{r_{12}^3}(g\mu_B\pi)^2 \left[3\frac{(\vec{\tilde{J}}_1 \cdot \vec{r}_{12})(\vec{\tilde{J}}_2 \cdot \vec{r}_{12})}{r_{12}^2} - \vec{\tilde{J}}_1 \cdot \vec{\tilde{J}}_2 \right] \frac{R_1^2 R_2^2}{a_0^4} \tag{3.5}$$

where $\vec{\tilde{J}}_i$ is the spin per Ho ion in each plaquette and $\vec{r}_{12}$ is the separation between plaquettes. If this interaction term is attractive ($\Delta U_{12} < 0$), then the configuration energy will be minimized by having the radii of both plaquettes (R_1, R_2) growing together. In this picture, attractive interactions between plaquettes on different domain walls can cause co-tunneling processes in which nucleation of one plaquette lowers the energy barrier for nucleation of the other. By contrast, if the interaction term is repulsive ($\Delta U_{12} > 0$), then these co-tunneling processes are suppressed, and the energetically favored tunneling paths consist of each plaquette growing independently of the other.

The sign of this interaction depends on the relative orientation and polarization of the two plaquettes. If one assumes that the plaquettes are opposite each other, and that their polarizations lie along the x-axis, the interaction simplifies to being

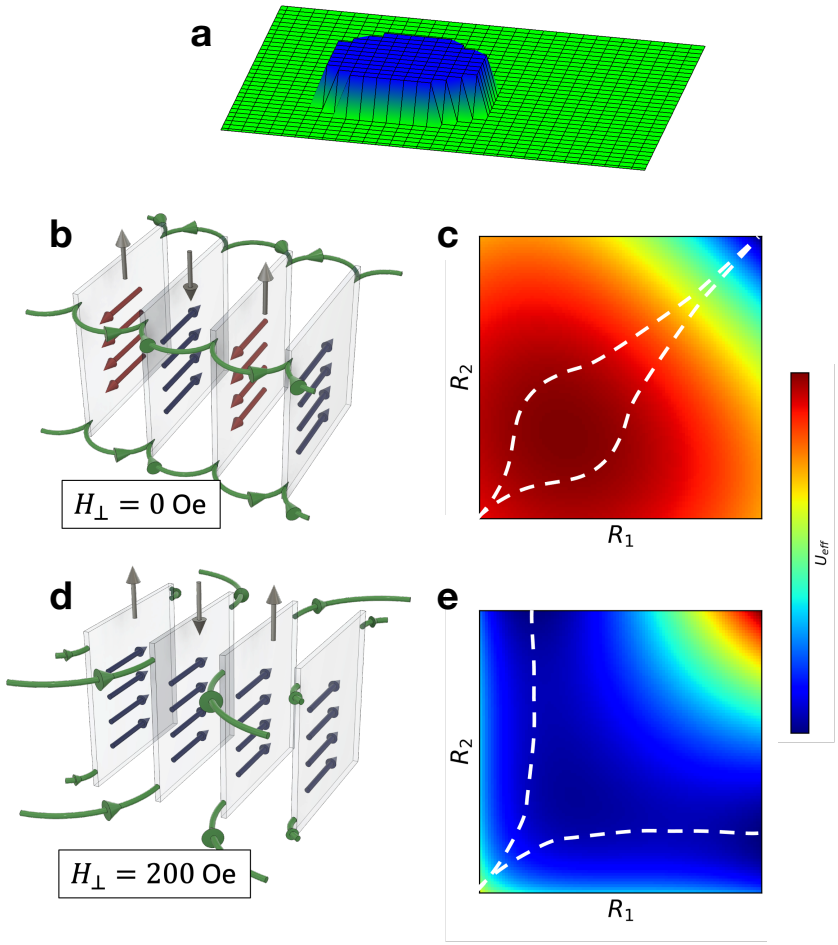

Figure 3.11: Domain wall configurations and interaction potentials. **a** Schematic of a Bloch domain wall with a single "plaquette" structure. Grid denotes locations of individual spins. **b,d** Vertical grey arrows designate the bulk magnetization direction within a domain along the Ising axis, while the red/blue arrows designate the transverse polarizations within a Bloch wall. The green curved arrows illustrate the demagnetization fields. The tunneling potentials **c,e** are a function of the radii of the two interacting plaquettes, R_1 and R_2, coupled via the dipolar interaction. **b** Staggered polarizations of the domain walls at zero transverse field with corresponding attractive interaction in **c** causing R_1 and R_2 to grow together (as indicated by the tunneling paths shown in white). **d** All walls polarized in the same direction due to the transverse field, with the corresponding repulsive interaction in **e**, cause plaquettes to grow independently from one another, as indicated by the tunneling paths shown in white.

attractive when the polarizations are aligned and being repulsive when they are anti-aligned. Hence, the polarizations of domain walls affect the tunneling dynamics by giving rise to cooperative tunneling of pairs of plaquettes on adjacent domain walls when their polarizations are anti-aligned, in addition to the standard independent tunneling processes of single plaquettes.

While the application of an external longitudinal field simply reduces the height of the tunneling barrier, accelerating plaquette nucleation and domain wall tunneling, application of a sufficiently strong transverse field will act to orient polarizations of all the walls to be parallel to the applied field. While the spatial extent of the measured avalanches is not known, the large number of spins involved in an avalanche ($\sim 10^{15}$–10^{16}) guarantees that the wall area will be large. Furthermore, since the Zeeman energy of the wall scales as the number of spins within the wall, the polarizations of these large sections of domain wall will be highly susceptible to even a modest transverse field. Thus, while a 200 Oe transverse field is much less than the single-ion tunneling field scale ($\sim$ 20 kOe)[63], or the quantum phase transition (QPT) field scale ($\sim$ 12 kOe)[69], it is large enough to appreciably polarize most domain walls in the same direction, thereby changing the statistics of the co-tunneling processes. I illustrate these two wall configurations in Fig. 3.11, with the wall polarizations staggered in zero transverse field in panel b, and the configuration with all walls polarized in the same direction in a finite transverse field in panel d.

When the external field is zero, the wall polarizations are random, giving rise to both aligned and anti-aligned domain wall configurations. Consequently, at zero field, co-tunneling processes will be possible due to the attractive interaction between the anti-aligned domain walls. When a finite transverse field is applied, however, all the walls polarize in the same direction, making all of the interactions between walls repulsive, and consequently suppressing the co-tunneling processes. I plot the corresponding tunneling potentials in Fig. 3.11c,e for the domain wall configurations in panels (b,d). (c) illustrates the attractive interaction due to the staggered polarizations of Bloch walls in zero field; (e) illustrates the repulsive interaction due to all wall polarizations being aligned along the external transverse field direction.

I emphasize that, while all domain wall motion is governed primarily through quantum tunneling of small plaquettes, large events consisting of 10^{15} spins are *avalanches* of many plaquette tunneling events triggering one another–not single coherent macroscopic tunneling events. Co-tunneling processes do not cause entire

walls to tunnel together, but they can cause simultaneous quantum nucleation of two plaquettes on adjacent walls at once, affecting the avalanche statistics through an introduction of a second avalanche activation mechanism.

One can consider what the predicted theoretical difference in the data would be if the sample were in the high-temperature classical regime, as opposed to the low-temperature quantum regime. It is useful to differentiate between the low-dimensional representations of macroscopic avalanche events (usually scalar metrics such as duration, integrated area, etc.), which measure an average over many spins, and the finer dynamics of how microscopic sections of domain wall are activated, and subsequently propagate. Since the avalanches measured in this work are so large ($\sim 10^{15}$ spins), the fast microscopic dynamics of individual spin flips will not be visible on the measurement timescale. In contrast, the basic size distribution of avalanches gives information about the spatial pinning potential, as each avalanche can be understood as a quasi-instantaneous (relative to the adiabatic drive) event which begins with a domain wall pinned in one site and ends with it pinned in another site.

There is a natural competition between the linear applied external potential (via the longitudinal field) and a restoring force due to demagnetization effects, as demagnetization fields are proportional to the bulk magnetization (in a simple spatially-uniform approximation). This means that stronger pinning will require a larger applied field to overcome, which in turn must be counter-balanced by a larger demagnetization force, resulting from a larger volume of flipped spins, and thus a larger avalanche. Because of this, the avalanche size distribution (which correlates with other event metrics) is primarily affected by the spatial distribution of the random pinning potential caused by the interplay of the long-range anisotropic dipolar interaction and spatial quenched disorder from chemical dilution.

Thermal fluctuations serve to excite domain walls over the pinning potential barrier at a weaker applied field than would otherwise be necessary—resulting in a smaller avalanche than would occur without fluctuations. However, increasing quantum fluctuations would also accomplish the same effect of activating domain wall motion “early”, and could look the same as in the classical case. For this reason I emphasize that the argument that $LiHo_{0.40}Y_{0.60}F_4$ is in the quantum regime stems from the fact that both measurements (DC hall magnetometry, and 1 MHz digitized temporal events) are completely temperature-independent across all measurement temperatures, within the quasi-linear portion of the hysteresis loop corresponding

to domain wall motion (and not domain creation/annihilation).

Whether the observed data is described as "quantum" or "classical" is frequently a matter of perspective (such as whether magnetism in solids can be ever be considered "classical" due to the quantum spin-1/2 nature of electrons), I would still argue that the Barkhausen events corresponding to pairs of domain walls nucleated by cooperative quantum tunneling is inexplicable by any traditional explanation, and therefore unambiguously a quantum phenomenon.

3.7 Conclusion

In this chapter I discussed bulk magnetic measurements that I made on $LiHo_xY_{1-x}F_4$ within the ferromagnetic ground state. When subjected to an external magnetic field along the Ising spin axis, a ferromagnet will respond by relaxing to a new equilibrium magnetization with an increased number of spins aligned with the field until the sample reaches saturation at a strong enough external field. In the low external field regime, these dynamics are dominated by the motion of domain walls separating the boundaries between domains of opposite magnetization. If the wall motion is uncorrelated between walls, the scalar coordinate of sample bulk magnetization $|M^z|$ can be interpreted as a particle in a random walk, where the underlying random pinning potential is due to the quenched sample disorder.

I first showed the avalanche statistics on one sample that exhibited approximate power laws over about one decade of logarithmic bin size. I compared the measured exponents to those predicted by both the short- and long-range domain wall depinning models and show that while they do not exactly match either model (consistent with measurements in the literature), the data still satisfy a self-consistency relation characteristic of avalanches. I then looked at the averaged event lineshape over different duration bins at multiple temperatures. The first observation is that the events still display the asymmetry characteristic of drag/dissipative effects even in the presence of an optical bandgap, which drives $LiHo_xY_{1-x}F_4$ into an insulating phase that does not support eddy currents. Since the literature generally [22, 85] attributes dissipation to eddy currents, this represents an important counter example of a sample that displays drag even without eddy currents. This is not, however, in contradiction with previous work, as signatures of drag should not depend on the exact microscopic source of the dissipation–whether the source is from coupling to conduction electrons or coupling to lattice vibrations. It was also observed that shortest events ($< 150\mu$s) retained their asymmetry even at elevated temperatures

while the longest events ($< 500\mu$s) became more symmetric at higher temperatures with increased thermal fluctuations.

I then turned to measurements made on a different dipole concentration crystal that did not display typical critical behavior. In these measurements I showed the existence of two distinguishable classes of avalanche events, which I denote "independent" and "cooperative". I argue that, from the temperature and field dependence of these two event classes, both event classes correspond to quantum tunneling activation, but the "cooperative" events are caused by co-tunneling events on multiple walls, while the "independent" events are caused by tunneling events of independent domain walls. I showed that the application of an external transverse field much smaller than any tunneling energy scale in the microscopic Hamiltonian can almost completely suppress the occurrence of the "cooperative" events, while only modestly decreasing the frequency of the "independent" events. The transverse field biases the transverse polarizations of each Bloch wall, determining whether the wall-wall interaction is attractive and supports co-tunneling, or repulsive and suppresses co-tunneling events.

Chapter 4

CONCLUSION

I conclude by summarizing my thesis, as well as expanding upon avenues of future work.

This thesis was dedicated to studying the dynamics of $LiHo_xY_{1-x}F_4$ as a model quantum Ising system. I started by discussing the quantum two-level system, and how the Ising model is useful for describing a many-body system of coupled qubits. I first derived the two-dimensional low-energy effective Hamiltonian for the composite electronic moment of a single Ho^{3+} ion, which displays remarkable easy-axis anisotropy with a ratio of $g_\parallel/g_\perp = 13.8/0.74 = 18.6$, making $LiHoF_4$ a model Ising magnet. I discussed the dipolar interaction between spins, pointing out the importance of the long-range, anisotropic nature of the coupling, as well as the importance of quantum corrections to the spin-spin interaction arising from off-diagonal terms $\sim V^{zx}$. Quenched disorder can be introduced into the system through chemical substitution of non-magnetic Y^{3+} ions in place of the magnetic Ho^{3+} ions, which affects the phase diagram of $LiHo_xY_{1-x}F_4$. Depending on the Ho^{3+} concentration x, the ground state behavior of $LiHo_xY_{1-x}F_4$ can be tuned from its single particle tunneling behavior [4], to renormalized spin clusters [35, 70], to glassy relaxation [59, 60, 64], to propagation of elastic two-dimensional domain walls moving within a random potential [71, 72], to extended coherent electronuclear modes [47]. In this thesis I focused on two classes of experiments–one done in the de-coupled cluster regime, and another in the ferromagnetic regime.

Starting with the weakly-coupled spin clusters in $LiHo_{0.045}Y_{0.955}F_4$, I reported pump-probe susceptibility measurements with a sufficiently strong pump/sufficiently weak dissipation to drive the system into a non-linear regime, driven by magnetic-dipole transitions arising from off-diagonal dipolar terms $\sim \sigma_i^z \sigma_j^x$. I demonstrated the non-linear behavior through frequency-mixing inelastic Raman-scattering measurements in the 100 Hz frequency regime. Furthermore, I show how "linear response" measurements made at the probe frequency show non-linear interference behavior, in which quantum interference between multiple excitation pathways occurs, and can be tuned into a regime with complete destructive interference, rendering the sample transparent to the incident radiation.

These cluster experiments are inherently difficult, because each instantiation depends on the cooldown and thermal boundary conditions, and so different cooldowns with identical experimental parameters $h_p, f_p, H_\perp$ exhibit different fit parameters for the Fano resonances, or sometimes no Fano resonances at all. This complicates the application of $LiHo_{0.045}Y_{0.955}F_4$ for practical quantum computation purposes, but there still remains promise in manipulating the long lifetimes of these high-Q excitations and probing the fundamental physics of decoherence. In particular, tuning these spin clusters to the $q = 0$ regime gives promise for long-lived excitations that can be coherently manipulated, and even possibly used for spin-echo type experiments.

I then transitioned to a set of Barkhausen noise measurements on the disordered ferromagnets, $LiHo_{0.65}Y_{0.35}F_4$ and $LiHo_{0.40}Y_{0.60}F_4$, in which the domain wall dynamics were probed in response to an adiabatic longitudinal driving field. The statistics of the collected Barkhausen events can reveal the underlying free-energy landscape and universality class through scaling analyses. Furthermore, I showed how $LiHo_{0.40}Y_{0.60}F_4$ exhibits temperature-independent, non-critical behavior, which can only be explained through quantum co-tunneling mechanisms.

Whether $LiHo_xY_{1-x}F_4$ exhibits critical behavior remains an open question. While approximate power-law behavior was shown across approximately one decade for $LiHo_{0.65}Y_{0.35}F_4$, further measurements on different concentrations would shed light on whether the source of criticality comes from proximity to a critical point, and whether a precise choice of chemical dilution x would extend the critical behavior. Similarly, measurements on samples with low dilution show promise for "infinite avalanche" behavior, in which the system exhibits a percolation transition. Finally, while domain images exist for the pure compound $LiHoF_4$, imaging of the disordered compound $LiHo_xY_{1-x}F_4$ are sorely needed. The tunneling dynamics are very sensitive to the exact structure of the domain walls, and this would shed light on the underlying random field distributions which are needed to quantitatively calculate tunneling rates.

Bibliography

[1] R. L. Aggarwal, D. J. Ripin, J. R. Ochoa, and T. Y. Fan. Measurement of thermo-optic properties of Y3Al5O12, Lu3Al5O12, YAIO3, LiYF4, LiLuF4, BaY2F8, KGd(WO4)2, and KY(WO4)2 laser crystals in the 80–300K temperature range. *Journal of Applied Physics*, 98(10):103514, November 2005. ISSN 0021-8979. doi: 10.1063/1.2128696.

[2] Bruno Alessandro, Cinzia Beatrice, Giorgio Bertotti, and Arianna Montorsi. Domain-wall dynamics and Barkhausen effect in metallic ferromagnetic materials. I. Theory. *Journal of Applied Physics*, 68(6):2901–2907, September 1990. ISSN 0021-8979. doi: 10.1063/1.346423.

[3] Juan Carlos Andresen, Helmut G. Katzgraber, Vadim Oganesyan, and Moshe Schechter. Existence of a Thermodynamic Spin-Glass Phase in the Zero-Concentration Limit of Anisotropic Dipolar Systems. *Physical Review X*, 4 (4):041016, October 2014. doi: 10.1103/PhysRevX.4.041016.

[4] B. Barbara, R. Giraud, W. Wernsdorfer, D. Mailly, P. Lejay, A. Tkachuk, and H. Suzuki. Evidence for resonant magnetic tunneling of rare-earth ions: From insulating to metallic matrix. *Journal of Magnetism and Magnetic Materials*, 272–276:1024–1029, May 2004. ISSN 0304-8853. doi: 10.1016/j.jmmm.2003.12.654.

[5] Jonathan Barés, Dengming Wang, Dong Wang, Thibault Bertrand, Corey S. O'Hern, and Robert P. Behringer. Local and global avalanches in a two-dimensional sheared granular medium. *Physical Review E*, 96(5):052902, November 2017. doi: 10.1103/PhysRevE.96.052902.

[6] Heinrich Barkhausen. *Physik Z.*, 20(401), 1919.

[7] J. E. Battison, A. Kasten, M. J. M. Leask, J. B. Lowry, and B. M. Wanklyn. Ferromagnetism in lithium holmium fluoride-LiHoF4. II. Optical and spectroscopic measurements. *Journal of Physics C: Solid State Physics*, 8(23):4089, December 1975. ISSN 0022-3719. doi: 10.1088/0022-3719/8/23/022.

[8] P. Beauvillain, J. P. Renard, and J. Magariño. Determination of crystal field parameters of LiRF4(R=Tb,Ho,Er) by high temperature susceptibility measurements. *Journal of Magnetism and Magnetic Materials*, 15–18:31–32, January 1980. ISSN 0304-8853. doi: 10.1016/0304-8853(80)90934-8.

[9] S. Bertaina, B. Barbara, R. Giraud, B. Z. Malkin, M. V. Vanuynin, A. I. Pominov, A. L. Stolov, and A. M. Tkachuk. Cross-relaxation and phonon bottleneck effects on magnetization dynamics in $\mathrm{Li}\mathrm{Y}{\mathrm{F}}_{4}:{\mathrm{Ho}}\hat{}3+$. *Physical Review B*, 74(18):184421, November 2006. doi: 10.1103/PhysRevB.74.184421.

[10] A. Biltmo and P. Henelius. Phase diagram of the dilute magnet $\mathrm{Li}{\mathrm{Ho}}_{x}{\mathrm{Y}}_{1\ensuremath{-}x}{\mathrm{F}}_{4}$. *Physical Review B*, 76(5):054423, August 2007. doi: 10.1103/PhysRevB.76.054423.

[11] A. Biltmo and P. Henelius. Unreachable glass transition in dilute dipolar magnet. *Nature Communications*, 3(1):857, May 2012. ISSN 2041-1723. doi: 10.1038/ncomms1857.

[12] D. Bitko, T. F. Rosenbaum, and G. Aeppli. Quantum Critical Behavior for a Model Magnet. *Physical Review Letters*, 77(5):940–943, July 1996. doi: 10.1103/PhysRevLett.77.940.

[13] Heinz-Peter Breuer and Francesco Petruccione. *The Theory of Open Quantum Systems*. Oxford University Press, 2002. ISBN 978-0-19-852063-4.

[14] J. Brooke, T. F. Rosenbaum, and G. Aeppli. Tunable quantum tunnelling of magnetic domain walls. *Nature*, 413(6856):610–613, October 2001. ISSN 1476-4687. doi: 10.1038/35098037.

[15] M. Buchhold, C. S. Tang, D. M. Silevitch, T. F. Rosenbaum, and G. Refael. Quantum dynamics in strongly driven random dipolar magnets. *Physical Review B*, 101(21):214201, June 2020. doi: 10.1103/PhysRevB.101.214201.

[16] John H. Carpenter, Karin A. Dahmen, Andrea C. Mills, Michael B. Weissman, Andreas Berger, and Olav Hellwig. History-induced critical behavior in disordered systems. *Physical Review B*, 72(5):052410, August 2005. doi: 10.1103/PhysRevB.72.052410.

[17] P. B. Chakraborty, P. Henelius, H. Kjønsberg, A. W. Sandvik, and S. M. Girvin. Theory of the magnetic phase diagram of Li Ho F 4. *Physical Review B*, 70(14):144411, October 2004. ISSN 1098-0121, 1550-235X. doi: 10.1103/PhysRevB.70.144411.

[18] H. P. Christensen. Spectroscopic analysis of LiHo${\mathrm{F}}_{4}$ and LiEr${\mathrm{F}}_{4}$. *Physical Review B*, 19(12):6564–6572, June 1979. doi: 10.1103/PhysRevB.19.6564.

[19] E. M. Chudnovsky, O. Iglesias, and P. C. E. Stamp. Quantum tunneling of domain walls in ferromagnets. *Physical Review B*, 46(9):5392–5404, September 1992. doi: 10.1103/PhysRevB.46.5392.

[20] Marek Cieplak and Mark O. Robbins. Dynamical Transition in Quasistatic Fluid Invasion in Porous Media. *Physical Review Letters*, 60(20):2042–2045, May 1988. doi: 10.1103/PhysRevLett.60.2042.

[21] Xavier Clotet, Stéphane Santucci, and Jordi Ortín. Experimental study of stable imbibition displacements in a model open fracture. II. Scale-dependent

avalanche dynamics. *Physical Review E*, 93(1):012150, January 2016. doi: 10.1103/PhysRevE.93.012150.

[22] Francesca Colaiori, Gianfranco Durin, and Stefano Zapperi. Eddy current damping of a moving domain wall: Beyond the quasistatic approximation. *Physical Review B*, 76(22):224416, December 2007. doi: 10.1103/PhysRevB.76.224416.

[23] A. H. Cooke, D. A. Jones, J. F. A. Silva, and M. R. Wells. Ferromagnetism in lithium holmium fluoride-LiHoF4. I. Magnetic measurements. *Journal of Physics C: Solid State Physics*, 8(23):4083, December 1975. ISSN 0022-3719. doi: 10.1088/0022-3719/8/23/021.

[24] Karin Dahmen and James P. Sethna. Hysteresis, avalanches, and disorder-induced critical scaling: A renormalization-group approach. *Physical Review B*, 53(22):14872–14905, June 1996. doi: 10.1103/PhysRevB.53.14872.

[25] Zsuzsa Danku and Ferenc Kun. Temporal and Spacial Evolution of Bursts in Creep Rupture. *Physical Review Letters*, 111(8):084302, August 2013. doi: 10.1103/PhysRevLett.111.084302.

[26] S. A. Díaz, C. Reichhardt, D. P. Arovas, A. Saxena, and C. J. O. Reichhardt. Avalanches and Criticality in Driven Magnetic Skyrmions. *Physical Review Letters*, 120(11):117203, March 2018. doi: 10.1103/PhysRevLett.120.117203.

[27] Alexander Dobrinevski, Pierre Le Doussal, and Kay Jörg Wiese. Avalanche shape and exponents beyond mean-field theory. *Europhysics Letters*, 108(6):66002, January 2015. ISSN 0295-5075. doi: 10.1209/0295-5075/108/66002.

[28] Tomer Dollberg, Juan Carlos Andresen, and Moshe Schechter. Effect of intrinsic quantum fluctuations on the phase diagram of anisotropic dipolar magnets. *Physical Review B*, 105(18):L180413, May 2022. doi: 10.1103/PhysRevB.105.L180413.

[29] M. Dubé and P. C. E. Stamp. Effects of Phonons and Nuclear Spins on the Tunneling of a Domain Wall. *Journal of Low Temperature Physics*, 110(3):779–840, February 1998. ISSN 1573-7357. doi: 10.1023/A:1022676810365.

[30] G. Durin, F. Bohn, M. A. Corrêa, R. L. Sommer, P. Le Doussal, and K. J. Wiese. Quantitative Scaling of Magnetic Avalanches. *Physical Review Letters*, 117(8):087201, August 2016. doi: 10.1103/PhysRevLett.117.087201.

[31] Gianfranco Durin and Stefano Zapperi. Scaling Exponents for Barkhausen Avalanches in Polycrystalline and Amorphous Ferromagnets. *Physical Review Letters*, 84(20):4705–4708, May 2000. doi: 10.1103/PhysRevLett.84.4705.

[32] Gianfranco Durin and Stefano Zapperi. The Barkhausen effect, April 2004.

[33] Stuart Field, Jeff Witt, Franco Nori, and Xinsheng Ling. Superconducting Vortex Avalanches. *Physical Review Letters*, 74(7):1206–1209, February 1995. doi: 10.1103/PhysRevLett.74.1206.

[34] Michael Fleischhauer, Atac Imamoglu, and Jonathan P. Marangos. Electromagnetically induced transparency: Optics in coherent media. *Reviews of Modern Physics*, 77(2):633–673, July 2005. doi: 10.1103/RevModPhys.77.633.

[35] S. Ghosh, R. Parthasarathy, T. F. Rosenbaum, and G. Aeppli. Coherent Spin Oscillations in a Disordered Magnet. *Science*, 296(5576):2195–2198, June 2002. doi: 10.1126/science.1070731.

[36] Sh. N. Gifeisman, A. M. Tkachuk, and V. V. Prizmak. Optical spectra of Ho3 + ion in LiYF4 crystals. *Optics and Spectroscopy*, 44:68–71, January 1978. ISSN 0030-400X.

[37] Michel J. P. Gingras and Patrik Henelius. Collective Phenomena in the LiHoxY1-xF4 Quantum Ising Magnet: Recent Progress and Open Questions. *Journal of Physics: Conference Series*, 320(1):012001, September 2011. ISSN 1742-6596. doi: 10.1088/1742-6596/320/1/012001.

[38] James P. Gleeson and Rick Durrett. Temporal profiles of avalanches on networks. *Nature Communications*, 8(1):1227, October 2017. ISSN 2041-1723. doi: 10.1038/s41467-017-01212-0.

[39] James P. Gleeson, Jonathan A. Ward, Kevin P. O'Sullivan, and William T. Lee. Competition-Induced Criticality in a Model of Meme Popularity. *Physical Review Letters*, 112(4):048701, January 2014. doi: 10.1103/PhysRevLett.112.048701.

[40] P. E. Hansen, T. Johansson, and R. Nevald. Magnetic properties of lithium rare-earth fluorides: Ferromagnetism in LiEr${\mathrm{F}}_{4}$ and LiHo${\mathrm{F}}_{4}$ and crystal-field parameters at the rare-earth and Li sites. *Physical Review B*, 12(11):5315–5324, December 1975. doi: 10.1103/PhysRevB.12.5315.

[41] André Herpin. Théorie du magnétisme. *(No Title)*.

[42] Touko Herranen and Lasse Laurson. Barkhausen Noise from Precessional Domain Wall Motion. *Physical Review Letters*, 122(11):117205, March 2019. doi: 10.1103/PhysRevLett.122.117205.

[43] Pau Jorba, editor. *SHPM Imaging of LiHoF4 at Ultra Low Temperatures*. 2014.

[44] Ryogo Kubo. Statistical-Mechanical Theory of Irreversible Processes. I. General Theory and Simple Applications to Magnetic and Conduction Problems. *Journal of the Physical Society of Japan*, 12(6):570–586, June 1957. ISSN 0031-9015. doi: 10.1143/JPSJ.12.570.

[45] Lasse Laurson, Xavier Illa, Stéphane Santucci, Ken Tore Tallakstad, Knut Jørgen Måløy, and Mikko J. Alava. Evolution of the average avalanche shape with the universality class. *Nature Communications*, 4(1):2927, December 2013. ISSN 2041-1723. doi: 10.1038/ncomms3927.

[46] Pierre Le Doussal, Kay Jörg Wiese, and Pascal Chauve. Two-loop functional renormalization group theory of the depinning transition. *Physical Review B*, 66(17):174201, November 2002. doi: 10.1103/PhysRevB.66.174201.

[47] M. Libersky, R. D. McKenzie, D. M. Silevitch, P. C. E. Stamp, and T. F. Rosenbaum. Direct Observation of Collective Electronuclear Modes about a Quantum Critical Point. *Physical Review Letters*, 127(20):207202, November 2021. doi: 10.1103/PhysRevLett.127.207202.

[48] Mikhail F. Limonov, Mikhail V. Rybin, Alexander N. Poddubny, and Yuri S. Kivshar. Fano resonances in photonics. *Nature Photonics*, 11(9):543–554, September 2017. ISSN 1749-4893. doi: 10.1038/nphoton.2017.142.

[49] Chen Liu, Ezequiel E. Ferrero, Francesco Puosi, Jean-Louis Barrat, and Kirsten Martens. Driving Rate Dependence of Avalanche Statistics and Shapes at the Yielding Transition. *Physical Review Letters*, 116(6):065501, February 2016. doi: 10.1103/PhysRevLett.116.065501.

[50] Amit P. Mehta, Karin A. Dahmen, and Yehuda Ben-Zion. Universal mean moment rate profiles of earthquake ruptures. *Physical Review E*, 73(5):056104, May 2006. doi: 10.1103/PhysRevE.73.056104.

[51] G. Mennenga, L. J. de Jongh, W. J. Huiskamp, and I. Laursen. A comparative study of the magnetic ordering specific heats of four S = 12 dipolar magnets: LiRF4 (R = Er, Dy, Ho, Tb). *Journal of Magnetism and Magnetic Materials*, 44(1):48–58, September 1984. ISSN 0304-8853. doi: 10.1016/0304-8853(84)90046-5.

[52] Peter Meyer, Jacques Pommier, and Jacques Ferre. Magnetooptic Observation Of Domains At Low Temperature In The Transparent Ferromagnet LiHoF[sub]4[/sub]. In *Electro-Optic and Magneto-Optic Materials and Applications*, volume 1126, pages 93–98. SPIE, December 1989. doi: 10.1117/12.961386.

[53] E. A. Muljarov, W. Langbein, and R. Zimmermann. Brillouin-Wigner perturbation theory in open electromagnetic systems. *Europhysics Letters*, 92(5):50010, January 2011. ISSN 0295-5075. doi: 10.1209/0295-5075/92/50010.

[54] Takashi Nakamura, Yusuke Kanno, and Shin Takagi. Single-collective-degree-of-freedom models of macroscopic quantum nucleation. *Physical Review B*, 51(13):8446–8456, April 1995. doi: 10.1103/PhysRevB.51.8446.

[55] Stefanos Papanikolaou, Felipe Bohn, Rubem Luis Sommer, Gianfranco Durin, Stefano Zapperi, and James P. Sethna. Universality beyond power laws and the average avalanche shape. *Nature Physics*, 7(4):316–320, April 2011. ISSN 1745-2481. doi: 10.1038/nphys1884.

[56] Stefanos Papanikolaou, Yinan Cui, and Nasr Ghoniem. Avalanches and plastic flow in crystal plasticity: An overview. *Modelling and Simulation in Materials Science and Engineering*, 26(1):013001, December 2017. ISSN 0965-0393. doi: 10.1088/1361-651X/aa97ad.

[57] Olga Perković, Karin Dahmen, and James P. Sethna. Avalanches, Barkhausen Noise, and Plain Old Criticality. *Physical Review Letters*, 75(24):4528–4531, December 1995. doi: 10.1103/PhysRevLett.75.4528.

[58] Olga Perković, Karin A. Dahmen, and James P. Sethna. Disorder-induced critical phenomena in hysteresis: Numerical scaling in three and higher dimensions. *Physical Review B*, 59(9):6106–6119, March 1999. doi: 10.1103/PhysRevB.59.6106.

[59] J. A. Quilliam, S. Meng, C. G. A. Mugford, and J. B. Kycia. Evidence of Spin Glass Dynamics in Dilute ${\mathrm{LiHo}}_{x}{\mathbf{Y}}_{1\ensuremath{-}x}{\mathbf{F}}_{4}$. *Physical Review Letters*, 101(18):187204, October 2008. doi: 10.1103/PhysRevLett.101.187204.

[60] D. H. Reich, B. Ellman, J. Yang, T. F. Rosenbaum, G. Aeppli, and D. P. Belanger. Dipolar magnets and glasses: Neutron-scattering, dynamical, and calorimetric studies of randomly distributed Ising spins. *Physical Review B*, 42(7):4631–4644, September 1990. doi: 10.1103/PhysRevB.42.4631.

[61] H. M. Rønnow, J. Jensen, R. Parthasarathy, G. Aeppli, T. F. Rosenbaum, D. F. McMorrow, and C. Kraemer. Magnetic excitations near the quantum phase transition in the Ising ferromagnet $\mathrm{Li}\mathrm{Ho}{\mathrm{F}}_{4}$. *Physical Review B*, 75(5): 054426, February 2007. doi: 10.1103/PhysRevB.75.054426.

[62] M. L. Sachtjen, B. A. Carreras, and V. E. Lynch. Disturbances in a power transmission system. *Physical Review E*, 61(5):4877–4882, May 2000. doi: 10.1103/PhysRevE.61.4877.

[63] M. Schechter and P. C. E. Stamp. Significance of the Hyperfine Interactions in the Phase Diagram of ${\mathrm{LiHo}}_{x}{\mathrm{Y}}_{1\ensuremath{-}x}{\mathrm{F}}_{4}$. *Physical Review Letters*, 95(26):267208, December 2005. doi: 10.1103/PhysRevLett.95.267208.

[64] M. A. Schmidt, D. M. Silevitch, G. Aeppli, and T. F. Rosenbaum. Using thermal boundary conditions to engineer the quantum state of a bulk magnet.

Proceedings of the National Academy of Sciences, 111(10):3689–3694, March 2014. doi: 10.1073/pnas.1316070111.

[65] James P. Sethna, Karin Dahmen, Sivan Kartha, James A. Krumhansl, Bruce W. Roberts, and Joel D. Shore. Hysteresis and hierarchies: Dynamics of disorder-driven first-order phase transformations. *Physical Review Letters*, 70(21): 3347–3350, May 1993. doi: 10.1103/PhysRevLett.70.3347.

[66] James P. Sethna, Karin A. Dahmen, and Christopher R. Myers. Crackling noise. *Nature*, 410(6825):242–250, March 2001. ISSN 1476-4687. doi: 10.1038/35065675.

[67] G. S. Shakurov, M. V. Vanyunin, B. Z. Malkin, B. Barbara, R. Yu. Abdulsabirov, and S. L. Korableva. Direct measurements of anticrossings of the electron-nuclear energy levels in LiYF4:Ho3+ with submillimeter EPR spectroscopy. *Applied Magnetic Resonance*, 28(3):251–265, September 2005. ISSN 1613-7507. doi: 10.1007/BF03166760.

[68] D. M. Silevitch, C. M. S. Gannarelli, A. J. Fisher, G. Aeppli, and T. F. Rosenbaum. Quantum Projection in an Ising Spin Liquid. *Physical Review Letters*, 99(5):057203, July 2007. doi: 10.1103/PhysRevLett.99.057203.

[69] D. M. Silevitch, G. Aeppli, and T. F. Rosenbaum. Switchable hardening of a ferromagnet at fixed temperature. *Proceedings of the National Academy of Sciences*, 107(7):2797–2800, February 2010. doi: 10.1073/pnas.0910575107.

[70] D. M. Silevitch, C. Tang, G. Aeppli, and T. F. Rosenbaum. Tuning high-Q nonlinear dynamics in a disordered quantum magnet. *Nature Communications*, 10(1):4001, September 2019. ISSN 2041-1723. doi: 10.1038/s41467-019-11985-1.

[71] D. M. Silevitch, J. Xu, C. Tang, K. A. Dahmen, and T. F. Rosenbaum. Magnetic domain dynamics in an insulating quantum ferromagnet. *Physical Review B*, 100(13):134405, October 2019. doi: 10.1103/PhysRevB.100.134405.

[72] C. Simon, D. M. Silevitch, P. C. E. Stamp, and T. F. Rosenbaum. Quantum Barkhausen Noise Induced by Domain Wall Co-Tunneling (Under Review).

[73] G. Sparks and R. Maaß. Shapes and velocity relaxation of dislocation avalanches in Au and Nb microcrystals. *Acta Materialia*, 152:86–95, June 2018. ISSN 1359-6454. doi: 10.1016/j.actamat.2018.04.007.

[74] P. C. E. Stamp. Quantum dynamics and tunneling of domain walls in ferromagnetic insulators. *Physical Review Letters*, 66(21):2802–2805, May 1991. doi: 10.1103/PhysRevLett.66.2802.

[75] P.c.e. Stamp, E.m. Chudnovsky, and B. Barbara. Quantum tunneling of magnetization in solids. *International Journal of Modern Physics B*, 06(09): 1355–1473, May 1992. ISSN 0217-9792. doi: 10.1142/S0217979292000670.

[76] S. M. A. Tabei, M. J. P. Gingras, Y.-J. Kao, and T. Yavors'kii. Perturbative quantum Monte Carlo study of ${\text{LiHoF}}_{4}$ in a transverse magnetic field. *Physical Review B*, 78(18):184408, November 2008. doi: 10.1103/PhysRevB.78.184408.

[77] Mehdi Talamali, Viljo Petäjä, Damien Vandembroucq, and Stéphane Roux. Avalanches, precursors, and finite-size fluctuations in a mesoscopic model of amorphous plasticity. *Physical Review E*, 84(1):016115, July 2011. doi: 10.1103/PhysRevE.84.016115.

[78] Cathelijne Ter Burg, Felipe Bohn, Gianfranco Durin, Rubem Luis Sommer, and Kay Jörg Wiese. Force Correlations in Disordered Magnets. *Physical Review Letters*, 129(10):107205, September 2022. ISSN 0031-9007, 1079-7114. doi: 10.1103/PhysRevLett.129.107205.

[79] Shubha Tewari, Dylan Schiemann, Douglas J. Durian, Charles M. Knobler, Stephen A. Langer, and Andrea J. Liu. Statistics of shear-induced rearrangements in a two-dimensional model foam. *Physical Review E*, 60(4):4385–4396, October 1999. doi: 10.1103/PhysRevE.60.4385.

[80] Eduard Vives and Antoni Planes. Hysteresis and avalanches in disordered systems. *Journal of Magnetism and Magnetic Materials*, 221(1):164–171, November 2000. ISSN 0304-8853. doi: 10.1016/S0304-8853(00)00380-2.

[81] Robert A. White and Karin A. Dahmen. Driving Rate Effects on Crackling Noise. *Physical Review Letters*, 91(8):085702, August 2003. doi: 10.1103/PhysRevLett.91.085702.

[82] Kenneth G. Wilson. The renormalization group and critical phenomena. *Reviews of Modern Physics*, 55(3):583–600, July 1983. doi: 10.1103/RevModPhys.55.583.

[83] Wenhao Wu, B. Ellman, T. F. Rosenbaum, G. Aeppli, and D. H. Reich. From classical to quantum glass. *Physical Review Letters*, 67(15):2076–2079, October 1991. doi: 10.1103/PhysRevLett.67.2076.

[84] Stefano Zapperi, Pierre Cizeau, Gianfranco Durin, and H. Eugene Stanley. Dynamics of a ferromagnetic domain wall: Avalanches, depinning transition, and the Barkhausen effect. *Physical Review B*, 58(10):6353–6366, September 1998. doi: 10.1103/PhysRevB.58.6353.

[85] Stefano Zapperi, Claudio Castellano, Francesca Colaiori, and Gianfranco Durin. Signature of effective mass in crackling-noise asymmetry. *Nature Physics*, 1(1):46–49, October 2005. ISSN 1745-2481. doi: 10.1038/nphys101.